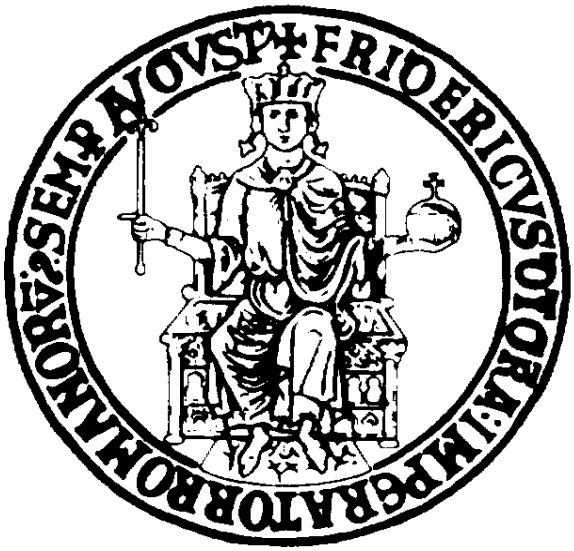

A.D. MCCXXIV

Complex Behavior in Impacting Systems

by
Gustavo Adolfo Osorio Londoo

Thesis Supervisor:

Mario diBernardo
Associate Professor of Nonlinear Systems

Thesis for the Degree of Doctor of Philosophy
Department of Computer and Systems Engineering
University of Naples Federico II
Napoli, Italy

Submitted to the Faculty of Engineering, University of Naples Federico II, in partial fulfillment of the requirements for the degree of Doctor of Philosophy.

Printed in Italy.
Napoli, November 2007.

To Juan Esteban.

Contents

Chapter 1

Introduction

Contents

1.1 Motivation

In the last decades interest on the study of *piecewise smooth* (PWS) dynamical systems has increased given the amount of real applications that naturally fits in this framework [19]. *Nonsmooth mechanical systems*, *electronic circuits with switches* and *hybrid controllers* are typical examples of PWS systems in applications. In the scientific literature much research effort has been spent to gain a better understanding of the *complex dynamics* that this class of systems can exhibit. An interesting example is presented in [70], where a simplified model for a high-speed milling cutter has been studied, showing a rich dynamical behavior described qualitatively through the analysis of smooth and nonsmooth bifurcations involving sudden transitions to chaos

This thesis was born in the context of the European projet SICONOS [63][62], (**Si**mulation and **Co**ntrol of **No**nsmooth Dynamical **S**ystems), whose purpose is to develop algorithms and software for the simulation and feedback–control of nonsmooth dynamical systems. *Nonsmoothness* is usually introduced into the system either by some nonsmooth control action or by the presence of nonsmooth events at a macroscopic level (such as impacts or switchings). This project saw contributions of scientists from various communities like Mechanics, Applied Mathematics, Systems and Control, and Numerical Analysis. It started in 2002 and finished in 2006.

Part of the work presented here was developed within the MIUR–PRIN project MACSI on Advanced Methodologies for Control of Hybrid Systems, where we were also interested in the analysis of nonsmooth bifurcating phenomena in a generic class of piecewise smooth dynamical systems employing the topological approach widely use in the theory of *Dynamical systems*.

For the study of nonsmooth systems there are different analytical, numerical and experimental tools developed from different perspectives. Fig. 1.1 is a synoptic representation of different issues that we have aimed at studying this thesis[1]. We divide our

[1] We use an underline mark for main contributions of this thesis.

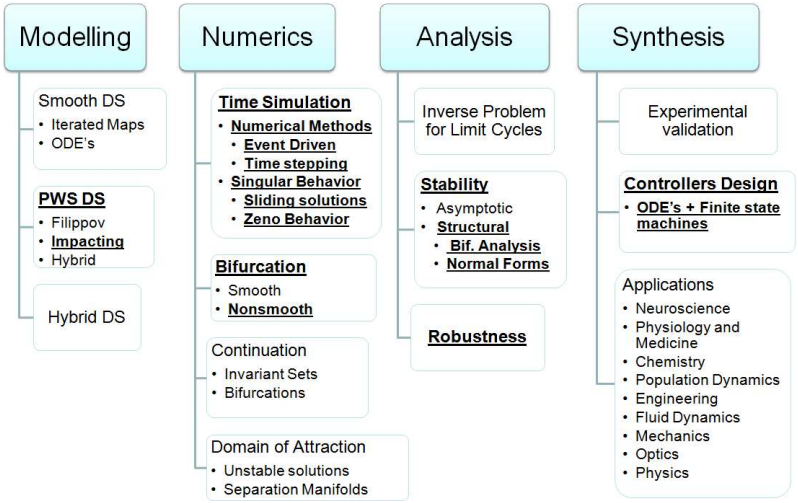

Figure 1.1: Synopsis of the contents of this thesis in the context of the qualitative theory of *Dynamical Systems*.

analysis in four main fields, specifically: *Modelling*, *Numerics*, *Analysis* and *Synthesis*.

Regarding *modelling*, we analyzed three different approaches to model nonsmooth systems: *Piecewise Smooth Dynamical Systems* (PWSDS), *Complementarity Systems* (CS) and *Hybrid Systems* (HS); while regarding *numerics* we focused on both *event driven* and *time stepping* simulation schemes. The most important contribution of this thesis is the complete *analysis* of a novel class of discontinuity–induced bifurcation of periodic orbits in a class of impacting systems. Finally, in relation to the *synthesis* we have proposed the study of models inspired from mechanics. Namely, we use the *cam–follower* system (so called in the context of mechanics), and an hybrid controller for an *Anti–lock Braking System* (ABS) as two relevant representative examples.

The *cam–follower* system is in many aspects similar to the *driven impact oscillator* since it represents also an example of a mechanical system with impacts, where the cam can be modelled as an external forcing while the follower can be modelled as an harmonic oscillator. Smooth and nonsmooth phenomena have been widely studied in *driven impact oscillator* focusing mainly on the *grazing bifurcation* [67][51], while other nonsmooth phenomena like *chattering*, *corner impacts* and *complex invariant sets* have not been studied deeply, and very few references can be found on these aspects [9][11][61][56]. We use the *cam–follower* as a more generic example than the *driven impact oscillator*, where complexity and nonsmooth phenomena are associated to the geometry of the *cam*. In addition the *cam–follower* system is a widely used mechanical device in applications and therefore it is possible to perform experiments that allows the comparison with the theory and numerics.

On the other hand, the hybrid controller for an ABS is studied to tackle one of the open problems in the field of nonsmooth systems related to the stability analysis of hybrid controllers using the topological approach proper of the theory of *Piecewise Smooth Dynamical Systems*.

1.2 Outline of the thesis

In Chapter 2 we present an overview of the qualitative theory of smooth and piecewise smooth dynamical systems. Rather than covering all the issues, the purpose is to present the fundamental concepts and definitions, that according to us, are needed in the study of impacting systems. After a brief presentation on smooth dynamical systems, we introduce nonsmooth dynamical systems, namely we present some definitions, invariant sets, stability analysis and numerical analysis emphasizing particularly the major differences with the classical theory of smooth systems.

In Chapter 3, we present an overview of the main strategies used in this thesis for the analysis of impacting systems. Rather than presenting a generalized theory for impacting systems, we have chosen a simplified representative example (that is the *cam–follower* system), where we study relevant issues on the modelling, simulation and stability analysis. The idea is to characterize systematically the properties inherent to impacting systems as well as the complexity associated to nonsmooth phenomena.

Chapter 4 is then devoted to the study of a representative cam-follower system, introduced in Chapter 3. Our main interest is to present the complex behavior unique to the nonsmooth nature of the cam profile; namely the qualitative effects under perturbations, for solutions with impacts near to discontinuity points.

In Chapter 5 we have performed a complete analysis of the corner impact bifurcation for a periodic orbit in the cam–follower system. This particular bifurcation scenario, exemplifies the use of *Discontinuity Maps* and the theory of *border collision* bifurcations in PWS Maps, to qualitatively characterize the interaction of impacting orbits with a discontinuity boundary.

In Chapter 6, we present the local and global analysis of impacting orbits near discontinuity points of the impacting manifold, using a *corner map* to model the interaction. This *discontinuity map* has been already used for the global analysis of impacting systems with smooth differentiable boundaries at hard and soft (grazing) impacts. Here, the analysis based on an appropriate *corner map* is intended to fill a gap in the existing literature, by performing the analysis of impacting orbits where the boundaries in the admissible space are not continuously differentiable (*i.e.* configuration space with corners).

In Chapter 7, we study an hybrid controller for an *Anti–lock Braking System* (ABS) as a *Piecewise Smooth Dynamical System*. To the best of our knowledge, this type of ABS has never been fully analyzed. Our interest is to characterize the performance (stability and robustness), rather than focusing on the design of new ABS control algorithms. We believe that our approach can give useful synthesis tools as it shows how a simple hybrid controller with a low number of both discrete states and parameters can be designed to guarantee stability and robustness. Finally, in Chapter 8 we summarize the main contributions of the thesis.

Chapter 2

Piecewise Smooth Dynamical Systems

Contents

The aim of this chapter is to present an overview of the qualitative theory of smooth and piecewise smooth dynamical systems. Rather than covering all the issues, the purpose is to present some of the fundamental concepts and definitions that, according to us, are needed to study impacting systems. After a brief presentation of smooth dynamical systems, we introduce nonsmooth dynamical systems, namely we give definitions of invariant sets, stability analysis and numerical analysis emphasizing particularly the differences with the classical theory of smooth systems. Most of the material presented in this chapter is inspired from [19] [43] and references therein.

2.1 Qualitative theory of dynamical systems

Qualitative theory of dynamical systems (also known as *dynamical systems theory*, *nonlinear dynamics*, *chaos theory*) [30] [76] [43] [69] [19], comprises methods for analyzing differential equations and iterated mappings. Specifically, nonlinear dynamics is concerned with the study of the stability of fixed points and periodic orbits, stable and unstable manifolds (first introduced by Poincaré in 1890) and the study of structural stability (first introduced by Andronov and Pontryagin in 1937) (see [34] for references). Next, we present the basic theoretical concepts that will be used in the rest of this thesis.

2.2 Smooth dynamical systems

A *smooth dynamical systems* or simply a *dynamical system* is a rule for the time evolution of a set of possible states. The *time* t takes values in an index set $\mathcal{T}$ which we usually consider to be either discrete (the set of integers $\mathbb{Z}$), or continuous (the set of real numbers $\mathbb{R}$). The possible states belonging to *state space* $\mathcal{X}$, is a discrete or continuous collection of coordinates that gives a complete description of the system. Given the current state of the system $x_0 \in \mathcal{X}$, the evolution rule or flow φ, predicts the state or vector $x(t)$ as:

$$\varphi : \mathcal{X} \times \mathcal{T} \to \mathcal{X} \tag{2.1}$$

where $x(t) := \varphi(x_0, t)$, with $x(0) = x_0$.

We say that (2.1) together with $\mathcal{X}$ and $\mathcal{T}$ (*i.e.* $\{\mathcal{X}, \mathcal{T}, \varphi(x,t)\}$), defines a dynamical system if following conditions are satisfied

$$\varphi(x, 0) = x, \qquad \text{for all } x \in \mathcal{X}, \qquad \text{(Identity)} \tag{2.2a}$$

$$\varphi(x, t+s) = \varphi(\varphi(x,t), s), \quad \text{for all } x \in \mathcal{X}, \text{ and } t, s \in \mathcal{T}. \quad \text{(Group)} \tag{2.2b}$$

The identity condition in (2.2a) basically implies that the state does not change spontaneously, and the group property in (2.2b) means that the evolution operator of the system does not change in time (*i.e.* The system is *autonomous*).

Next, we will focus on basic definitions for *discrete maps* and *continuous flows*, which are the most common classes of dynamical systems used all through this thesis.

2.2.1 Discrete maps and iterated maps

A *discrete map* or simply a *map*, is an evolution rule defined in discrete time, and in a continuous state space. A map $\pi : \mathbb{R}^n \times \mathbb{Z} \to \mathbb{R}^n$ defines a dynamical system where $t \in \mathbb{Z}$

The time evolution can be defined in an iterative form as

$$P : \mathbb{R}^n \to \mathbb{R}^n, \text{ where } x \mapsto P(x), \tag{2.3}$$

with $x \in \mathbb{R}^n$. The iterative operator in (2.3) is often written as $x_{n+1} = P(x_n)$ with $n \in \mathbb{Z}$. Notice that given an initial condition $x(0) = x_0$, a generic element at time $t = n$ can be obtained from

$$x(n) = P^{(n)}(x_0). \tag{2.4}$$

where $P^{(n)} := P \circ P \circ \cdots \circ P$, n–times.

Example: The *logistic map* is an instance of how a very simple nonlinear system can present very complicated behavior. It is a discrete model used to describe demographic evolution, and mathematically is written

$$x_{n+1} = \mu x_n(1 - x_n), \quad \mu \in [0, 1]. \tag{2.5}$$

where μ is the growth constant of the population (For further details see [49]).

2.2.2 Continuous flows and ODEs

A dynamical system can also be defined by an *initial value problem*, through a *ordinary differential equation* of the type

$$\dot{x} := \frac{dx}{dt} = F(x). \tag{2.6}$$

In (2.1) $\mathcal{X} \equiv \mathbb{R}^n$, $\mathcal{T} \equiv \mathbb{R}$ and the flow is defined by $\varphi \equiv \phi$. The state of the system will be given by

$$x(t) = \phi(x_0, t), \tag{2.7}$$

where $\phi : \mathbb{R}^n \times \mathbb{R} \to \mathbb{R}^n$ and $x(0) = x_0$. The evolution rule ϕ satisfies (2.6) in the sense that

$$\frac{d}{dt}(\phi(x, t))\bigg|_{t=\tau} = F(\phi(x, \tau)). \tag{2.8}$$

Example: A periodically forced, damped harmonic oscillator satisfies the second order differential equation

$$\ddot{q} + 2\zeta\dot{q} + \kappa q = a\cos\omega t, \tag{2.9}$$

where ζ and κ are damping and spring constants respectively, and ω is the angular velocity of the periodic forcing. We can define the state variables $x_1 := q$, $x_2 := \dot{q}$ and $x_3 := \omega t$ such that (2.9) can be written as a set of ordinary differential equations:

$$\begin{aligned} \dot{x}_1 &= x_2, \\ \dot{x}_2 &= \kappa x_1 - 2\zeta x_2 + a\cos x_3, \\ \dot{x}_3 &= \omega t. \end{aligned}$$

2.3 Qualitative dynamics and phase portraits

Given a generic dynamical system of the form (2.1), the set of all points $\varphi(x, t)$ for $t \in \mathcal{T}$, is called the *trajectory* or *orbit* through the point x. The phase portrait of a dynamical system is a partitioning of the state space into orbits.

An *invariant set* of a dynamical system is a subset $\Lambda \subset \mathcal{X}$ such that $x_0 \in \Lambda$ implies $\varphi(x_0, t) \in \Lambda$ for all $t \in \mathcal{T}$. An invariant set that is closed and bounded is called an *attractor* if:

- for any sufficiently small neighborhood $U \subset \mathcal{X}$ of Λ, there exists a neighborhood V of Λ such that $\phi(x, t) \in U$ for all $x \in V$ and all $t > 0$, and
- for all $x \in U$, $\phi(x, t) \to \Lambda$ as $t \to \infty$.

A dynamical system may have many competing attractors, with their relative importance being indicated by the set of initial conditions that they attract, that is, their *domain of attraction*. The *domain of attraction* (also known as the *basin of attraction*) of an invariant set Λ, is the maximal set of initial conditions x for which $\varphi(x,t) \to \Lambda$ as $t \to \infty$.

The qualitative description of a dynamical system is given by the description of the invariant sets that compose its phase portrait. Next, we briefly describe the main types of invariant sets.

Equilibria. The simplest form of invariant set is an equilibrium solution (or fixed points) x^* which satisfies $\varphi(x^*,t) = x^*$ for all t. These are also sometimes called stationary points.

Periodic orbits. The next most complex kind of invariant set is a periodic orbit; which comprises an initial condition x_p and a period T which is the smallest time $T > 0$ for which $\varphi(x_p,T) = x_p$. Periodic orbits form closed curves in phase space (topologically they are circular). A periodic orbit that is isolated (*i.e.* such that it does not have any other periodic orbits in its neighborhood) is termed a limit cycle.

Homoclinic and heteroclinic orbits. Another important class of invariant sets are connecting orbits which tend to other invariant sets as time goes asymptotically to $+\infty$ and to $-\infty$. Consider for example orbits which connect equilibria. A homoclinic orbit is a trajectory $x(t)$ that connects an equilibrium x^* to itself; $x(t) \to x^*$ as $t \to \pm\infty$. A heteroclinic orbit connects two different equilibria x_1^* and x_2^* ; $x(t) \to x_1^*$ as $t \to -\infty$ and $x(t) \to x_2^*$ as $t \to +\infty$. Homoclinic and heteroclinic orbits play an important role in separating the basins of attraction of other invariant sets.

Other invariant sets. It is quite possible for dynamical systems to contain certain simple geometric subsets of phase space where trajectories must remain for all time once they enter. The dynamics on this invariant sets could contain equilibria, periodic orbits and other attractors. Similarly, flows can contain invariant tori, invariant spheres, cylinders etc. Invariant sets that are everywhere locally smoothly described by an m-dimensional set of coordinates are called *invariant manifolds*.

Chaos. It might be defined in a number of different ways. Here we say that invariant sets are chaotic if initial conditions diverge from each other locally, and if there is at least one trajectory in the invariant set such that not only eventually comes back arbitrarily close to itself, but to every point of the invariant set. This property ensures that we are talking of an attractor composed of a single piece, not two separate ones. This property is also known as *topological transitivity*.

2.4 Asymptotic and structural stability on smooth systems

The stability of an orbit of a dynamical system characterizes whether nearby (i.e., perturbed) orbits will remain in a neighborhood of that orbit or be repelled away from it. *Asymptotic stability* additionally characterizes attraction of nearby orbits to this orbit

in the long-time limit. The distinct concept of *structural stability* concerns qualitative changes in the family of all solutions due to perturbations to the functions defining the dynamical system.

2.4.1 Stability

An important notion of stability in autonomous dynamical systems in that of either *Lyapunov* or *asymptotic stability* of an invariant set. In general, the former means stability in the weak sense that trajectories starting nearby to the invariant set remain close to it for all time, whereas the latter is more restrictive. Both refer to stability of invariant sets with respect to perturbations of initial conditions, at fixed parameter values.

Stability of invariant sets. An invariant set Λ is called stable if

1. for any sufficiently small neighborhood $U \supset \Lambda$ there exists a neighborhood $V \supset \Lambda$ such that $\varphi(x,t) \in U$ for all $x \in V$ and all $t > 0$;

2. there exists a neighborhood $U' \supset \Lambda$ such that $\varphi(x,t) \to \Lambda$ for all $x \in U'$ as $t \to +\infty$

If Λ is an equilibrium or a cycle, this definition turns into the standard definition of stable equilibria or cycles. Property (1) is called Lyapunov stability. If a set Λ is Lyapunov stable, nearby orbits do not leave its neighborhood. Property (2) is sometimes called asymptotic stability. There are invariant sets that are Lyapunov stable but not asymptotically stable.

Limit cycles and Poincaré maps One of the main building blocks of the dynamics in a set of ODEs is the topology analysis of its periodic solutions (or limit cycles). Limit cycles provide a natural way to transform between flows and maps. Consider a limit cycle solution $x(t) = p(t)$ of period $T > 0$, that is $p(t+T) = p(t)$. To study the dynamics near such a cycle, we can choose a Poincaré section, which is an $(n-1)$-dimensional surface Π that contains a point $x_p = p(t_p)$ on the limit cycle and which is transverse to the flow at x_p. We can use the flow φ to define a map $\mathcal{P}$ from Π to Π, called the *Poincaré map*, which is defined for x sufficiently close to x_p as

$$\mathcal{P}(x) = \phi(x, \tau(x)), \tag{2.10}$$

where $\tau(x)$ is defined implicitly as the time closest to T for which $\phi(x,\tau(x)) \in \Pi$.

Note that we can then define the Poincaré map as a smooth projection S of the fixed time-T map $\phi(x,T)$ for $x \in \Pi$ such that

$$\mathcal{P}(x) = S(\phi(x,T), x), \tag{2.11}$$

where $S(y,x) := \phi(y, \tau(x))$. We can study the stability of the periodic solution by studying the spectrum of the Jacobian matrix of the Poincaré map at x_p (*i.e.* $eig\{\mathcal{P}_x(x_p)\}$).

In general, a consequence of using Poincaré maps rather than flows in the stability analysis of invariant sets is that they reduce their dimension of the sets we need to consider. Thus, limit cycles of flows correspond to isolated fixed points of Poincaré maps; invariant tori correspond to closed curves of the map; and a chaotic invariant sets decrease their fractal dimension by one.

2.5 Structural stability

Dynamical systems theory aims to classify dynamics qualitatively. Structurally stable systems are ones for which all *nearby* systems have qualitatively *equivalent* dynamics. Thus we need a precise notion of nearby and also of equivalence. *Nearby* refers to any possible perturbation of the system itself (the function $F(x)$ for ODE), including for example variation of the systems parameters. We call two systems *equivalent* if their phase spaces have the same dimension, the same number and type of invariant sets, in the same general position with respect to each other. To achieve such a definition, we use mathematical topology.

Topological equivalence. We say that two phase portraits are *topologically equivalent* if there is a smooth transformation that stretches, twists, rotates, but not folds one phase portrait into the other. Such transformations are called homeomorphisms, which are continuous functions defined over the entire phase space whose inverses are also continuous.

Two dynamical systems defined by operators $\varphi, \psi : \mathcal{X} \times \mathcal{T} \to \mathcal{X}$ are *topologically equivalent* if there is a homeomorphism h that maps the orbits of the first system onto orbits of the second one, preserving the direction of time.

One of the key applications of topological equivalence is to show that under *hyperbolicity* condition, linearization of the dynamical systems about the neighborhood of an invariant set are locally topologically equivalent.

It can be proved that the flow local to any two hyperbolic equilibria of n-dimensional systems which have the same number of eigenvalues with negative real part are topologically equivalent to each other. Now, we define hyperbolicity for flows and maps as:

Hyperbolicity in Flows. Consider an equilibrium x^* of a flow φ defined by a system of ODEs $\dot{x} = F(x)$. We refer to the eigenvalues of an equilibrium x^*, to mean the eigenvalues of the associated Jacobian matrix $F_x(x^*)$. An equilibrium is said to be hyperbolic if none of its eigenvalues lie on the imaginary axis.

Hyperbolicity in Maps. Similarly, consider a fixed point x^* of a map π defined by the iterated equation $x_{n+1} = P(x_n)$. We refer to the multipliers μ_i of a fixed point x^*, to mean the eigenvalues of the associated Jacobian matrix $P_x(x^*)$. A fixed point is said to be hyperbolic if none of the multipliers lie on the unit circle.

2.5.1 Bifurcations

We are now interested in the parameter dependance of a dynamical system. So for ODEs or maps we write

$$\dot{x} = F(x, \mu), \quad \text{or} \quad x_{n+1} = P(x_n, \mu),$$

where $\mu \in \mathbb{R}^m$ is a vector of parameters.

Take some value $\mu = \mu_0$ and consider a maximal connected parameter set containing μ_0 and composed by those points for which the system has a phase portrait that is topologically equivalent to that at μ_0. Taking all such sets in the parameter space $\mathbb{R}^m$, we obtain the parametric portrait of the system. The parametric portrait together with its characteristic phase portraits constitute a *bifurcation diagram*.

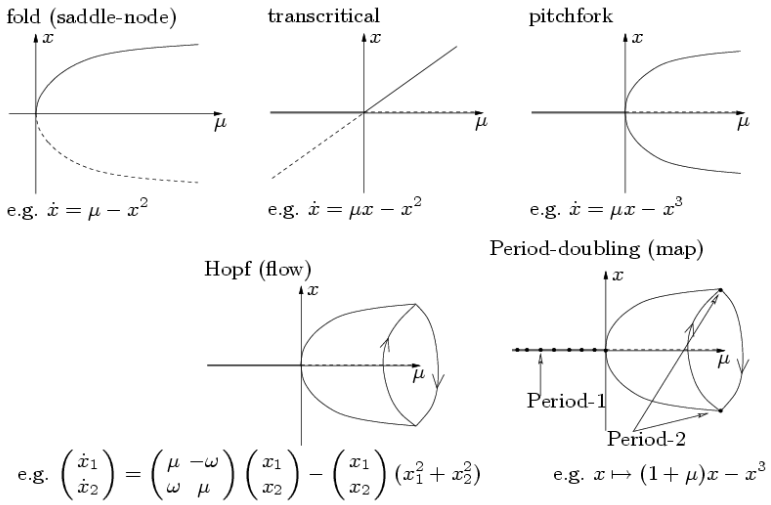

Figure 2.1: Main codimention-1 local bifurcations on smooth dynamical systems.

Local Bifurcations. A local bifurcation arises due to the loss of hyperbolicity of an invariant set upon varying a parameter. All other bifurcations are called global bifurcations. The *codimension* is the number of independent conditions determining the bifurcation; this is the codimension of a certain bifurcation is the same in all generic systems depending on a sufficient number of parameters.

Main codimension-one local bifurcations. Many kinds of local bifurcations of smooth systems have been studied and classified, see for example [43].

Figure 2.1 summarizes the main types of codimension-one local bifurcations of smooth vector fields and an associated representative bifurcation diagram. In each case, under appropriate defining and non-degeneracy conditions, one can calculate an appropriate *normal form* that can be obtained by smooth coordinate transformations from any system that undergoes the bifurcation in question.

Note that bifurcations of equilibria in flows have a direct analogy to limit cycle bifurcations; this is, limit cycles can present fold (or saddle-node), pitchfork or transcritical bifurcations. The study of codimension–one bifurcations of limit cycle can be studied through the bifurcations of fixed points in the associated Poincaré map introduced in (2.10) or equivalently (2.11) as

$$x_{n+1} = \mathcal{P}(x_n, \mu). \tag{2.12}$$

The defining condition is that for a fixed point in a flow there is an eigenvalue at zero and for the map that there is a multiplier at 1. The case of the Hopf bifurcation is more subtle, this is for maps occurs a complex pair of eigenvalues cross the unit circle. For torus or Neimark-Sacker bifurcation there is a birth of invariant circles of the map.

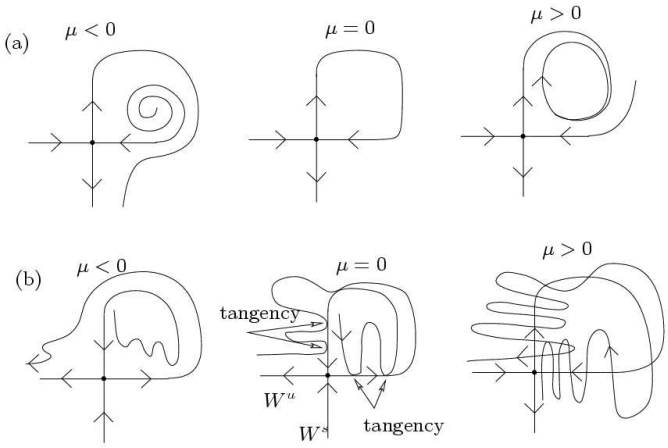

Figure 2.2: Main codimention-1 global bifurcations on smooth dynamical systems.

Global bifurcations. In contrast, global bifurcations typically occur because of a change in the topology of stable and unstable manifolds of invariant sets. A typical example is a homoclinic bifurcation when the stable and unstable manifold of the same invariant set form an intersection or tangency at a fixed parameter value.

2.6 Piecewise smooth dynamical systems

A *piecewise smooth (PWS) dynamical system* is a set of smooth dynamical systems (*i.e.* with elements of the form $\mathcal{D}_i = \{\mathcal{X}_i, \mathcal{T}_i, \varphi_i(x,t)\}$[1]); plus a set of rules for concatenation in time for some dynamical system $\mathcal{D}_i$ to another $\mathcal{D}_j$, such that identity and group conditions are satisfied. In general the set of rules for concatenation can be expressed through zero level sets of scalar functions, say $\sigma_{ij} : \mathbb{R}^n \to \mathbb{R}^2$, to commute at time τ from $\mathcal{D}_i$ to $\mathcal{D}_j$; such that the final state $x_\sigma := x(\tau) = \varphi_i(x_0, \tau)$ becomes an initial state as $x(\tau) \equiv \varphi_j(x_\sigma, 0)$. This is equivalent to say that the state x at commutation time τ can be expressed as function of both evolution operators.

In [19] an extensive study of PWS dynamical system can be found. Here, we present some representative examples that illustrates fundamental properties.

2.6.1 Piecewise smooth maps

A piecewise-smooth map is described by a finite set of smooth maps

$$x \mapsto P_i(x, \mu), \text{ for } x \in S_i,$$

[1] see definition of Smooth Dynamical System in Sec.2.2

[2] In addition to the transversality condition.

where $\cup_i S_i = D \subset \mathbb{R}^n$ and each S_i has a non-empty interior. The intersection Σ_{ij} between the closure (set plus its boundary) of the sets S_i and S_j (that is, $\Sigma_{ij} := \bar{S}_i \cap \bar{S}_j$) is either an $\mathbb{R}^{(n-1)}$-dimensional manifold included in the boundaries ∂S_j and ∂S_i, or is the empty set. Each function P_i is smooth in both the state x and parameter μ for any open subset U of S_i.

2.6.2 Piecewise smooth flows (ODEs)

A piecewise-smooth flow is given by a finite set of ODEs

$$\dot{x} = F_i(x, \mu), \text{ for } x \in S_i,$$

where $\cup_i S_i = D \subset \mathbb{R}^n$ and each S_i has a non-empty interior. The intersection $\Sigma_{ij} := \bar{S}_i \cap \bar{S}_j$ is either an $\mathbb{R}^{(n-1)}$ dimensional manifold included in the boundaries ∂S_j and ∂S_i, or is the empty set. Each vector field F_i is smooth in both the state x and parameter μ and defines a smooth flow $\phi_i(x,t)$ within any open set $U \in S_i$. In particular, each flow ϕ_i is well-defined on both sides of the boundary S_j.

Example: The bilinear oscillator, can be written as the first-order system by setting $x_1 = q$, $x_2 = \dot{q}$ and $x_3 = t$ so that

$$\dot{x}_1 = x_2, \tag{2.13a}$$
$$\dot{x}_2 = -2\zeta x_2 - \kappa_i x_1 + a\cos(x_3), \tag{2.13b}$$
$$\dot{x}_3 = 1, \tag{2.13c}$$

where the value of κ_i depends on region S_i, with $S_1 = \{x_1 < 0\}, S_2 = \{x_1 > 0\}$.

2.6.3 Filippov systems

Consider a general piecewise-smooth continuous system with a single boundary Σ , such that

$$\dot{x} = \begin{cases} F_1(x), & \text{if } H(x) > 0, \\ F_2(x), & \text{if } H(x) < 0, \end{cases} \tag{2.14}$$

where Σ is defined by the zero set of a smooth function H and $F_1(x) \neq F_2(x)$ if $H(x) = 0$. This class of systems must be treated with great care since we have to allow the possibility of *sliding motion*. In order to define sliding, it is useful to think of system (2.14) local to the discontinuity boundary between two regions defined by the zero set of the smooth function $H(x) = 0$.

The *sliding region* of the discontinuity set of a system of the form (2.14) is given by that portion of the boundary of $H(x)$ for which $(H_x F_1) \cdot (H_x F_2) < 0$. That is, $H_x F_1$ (the component of F_1 normal to H) has the opposite sign to $H_x F_2$. Thus the boundary is simultaneously attracting (or repelling) from both sides.

Two approaches exist in the literature for formulating the equations for flows that slide when written in the general form. These are Utkin equivalent control method [75] and Filippov convex method [25]. In Utkin method one supposes that the system flows according to the sliding vector field F_{12} which is the average of the two vector fields F_1 (in region S_1) and F_2 (in region S_2) plus a control $\beta(x) \in [-1, 1]$ in the direction of the difference between the vector fields:

$$F_{12} = \frac{F_1 + F_2}{2} + \frac{F_2 - F1}{2}\beta(x).$$

Specifically the equivalent control is

$$\beta(x) = -\frac{H_x F_1 + H_x F_2}{H_x F_2 - H_x F_1}.$$

Filippov's method, by contrast, takes a simple convex combination of the two vector fields

$$F_{12} = (1-\alpha)F_1 + \alpha F_2.$$

with $0 \leq \alpha \leq 1$, where

$$\alpha(x) = \frac{H_x F_1}{H_x(F_1 - F_2)}.$$

Sometimes, where there is no ambiguity we write $F_{ij} := F_s$ to represent the sliding flow.

2.6.4 Impacting systems

An impacting system comprises a smooth dynamical system whose flow may be defined by

$$\dot{x} = F(x), \text{ if } x \in int\{\Omega\} \text{ or } x \in \partial\Omega^+, \tag{2.15}$$

plus an impact map

$$x \mapsto \rho(x), \text{ if } x \in \partial\Omega^-. \tag{2.16}$$

Here Ω is called the *admissible space* and $\partial\Omega^-$ is part of the boundary set $\partial\Omega$ (*impacting surface*), that in general has lower dimension.

Notice that the impacting system in (2.15) (2.16) may implicitly define several dynamical modes associated to the constrained dynamics.

Impacting system with a single impact surface

Let us define a unique impacting surface by the zero level set of a smooth function $H(x)$ with negative relative velocity and the admissible space Ω is defined by $H(x) \geq 0$.

We can define an impacting system with a single impact surface as

$$\begin{cases} \dot{x} = F(x), & \text{if } H(x) > 0, \text{ or } H(x) = 0,\ v(x) \geq 0, \\ x^+ = R(x^-), & \text{if } H(x^-) = 0,\ v(x^-) > 0. \end{cases} \tag{2.17}$$

$$x^+ = R(x^-) = x^- - W(x^-)v(x^-),$$

To describe the possible constrained motion, we use the equivalent sliding vector field

$$F_s(x) = F(x) + \lambda(x)W(x),$$

when $H(x) = 0$, $v(x) = 0$ and $a(x) < 0$, where

$$\lambda(x) = -\frac{a(x)}{(v_x W)(x)}.$$

Example. A classical example is the driven impact oscillator with a Newton–like restitution law for elastic impacts. We can write the impacting system in the form

$$\begin{bmatrix} \dot{x}_1 \\ \dot{x}_2 \end{bmatrix} = \begin{bmatrix} 0 & 1 \\ -1 & -2\zeta \end{bmatrix} \begin{bmatrix} x_1 \\ x_2 \end{bmatrix} + \begin{bmatrix} 0 \\ \cos(\omega t) \end{bmatrix}, \tag{2.18a}$$

$$\begin{bmatrix} x_1(\tau^+) \\ x_2(\tau^+) \end{bmatrix} = \begin{bmatrix} 1 & 0 \\ 0 & -r \end{bmatrix} \begin{bmatrix} x_1(\tau^-) \\ x_2(\tau^-) \end{bmatrix}. \tag{2.18b}$$

Here we have the free body dynamics together with the impact rule which applies at impact time τ, and the state vector $x = (x_1, x_2, x_3)^T$, is defined as

$$\begin{array}{lll} x_1 = & H(x), & \textit{(Relative position)} \\ x_2 = & H_x F(x), & \textit{(Relative velocity)} \\ x_3 = & t. & \end{array} \tag{2.19}$$

Zeno phenomenon Typically, unlike sliding motion in Filippov systems, impacting systems do not enter a sticking region directly, but via a chattering sequence (also known in control theory as a Zeno phenomenon). Such a sequence begins if an impact occurs within Σ^-, close to the set Σ^0 with $v(x^+) \ll 1$ and $a(x^+) < 0$. There follows an infinite sequence of impacts, of successively reduced velocity, which converges in finite time, onto a point in the sticking set. After the accumulation of such a sequence, the motion will evolve in the sticking set in the manner described above. We shall return to an analysis of chattering in Chapter 4. Chattering sequences are a commonly observed feature of hybrid systems, and require special care when computing the flow numerically.

2.7 Asymptotic and structural stability of PWS

It is a particularly cumbersome task to provide necessary and sufficient conditions that guarantee the asymptotic stability of a desired invariant set of a piecewise-smooth system (see [47]). Even the problem of assessing the asymptotic stability of an equilibrium that rests on a discontinuity boundary is an open problem in general.

Thus, all the bifurcations discussed in Sec.2.5.1 can also occur in piecewise smooth systems. However, there are also other bifurcations that are unique to piecewise-smooth systems. These typically involve non-generic interactions of an invariant set with a discontinuity boundary.

Here we shall introduce the broader concept of a discontinuity-induced bifurcation [18] [14]. By this term we will identify qualitative changes to the topology of invariant sets with respect to the discontinuity boundaries. Specifically, we wish to single out parameter values at which the invariant set changes its event sequence, that is the order and sense of interaction with the discontinuity boundaries. Such changes are typically brought about (or induced) through non-transversal interaction with a discontinuity boundary.

2.7.1 Discontinuity induced bifurcations (DIB)

The analysis of discontinuity-induced bifurcation in maps is relatively straightforward; one merely has to consider the fate of iterates that land either side of the discontinuity. DIBs in piecewise-smooth flows are far harder to analyze, because one must establish the fate of topologically distinct trajectories close to the structurally unstable event that determines the bifurcation. A key analytical tool for the study of DIBs involving limit

cycles and more complex invariant sets, is the *discontinuity map* (DM), a term first introduced by Nordmark [51]. This is a local map that is defined locally near the point at which a trajectory interacts with a discontinuity boundary. When composed with a global Poincaré map (for example around the limit cycle), the DM takes into account the correction to be made because of the interaction with the discontinuity boundary.

It is natural to ask what form $\mathcal{P}$ takes when $\| x - x_p \|$ is small. The answer to this question takes three forms, and depends crucially upon the nature of the orbit $p(t)$. If $p(t)$ lies wholly inside S_i then nearby orbits will also lie inside S_i. In this case the fixed time-T map starting from x will be the smooth flow map $\mathcal{P}(x) = \phi_i(x,t)$, which has a well-defined Taylor series,

$$P(x) = N(x - x_p) + O(\| x - x_p \|^2),$$

where $N = \phi_i, x(x_p, T)$ is the Jacobian derivative with respect to x of the flow ϕ_i around the periodic orbit, evaluated at $x = x_p$. More interesting things happen if the periodic orbit $p(t)$ intersects discontinuity surfaces Σ_{ij}. Consider next the case where $p(t)$ has two transverse intersections with a discontinuity set Σ. In this case it is tempting to assume that the linearization of the Poincaré map takes the form $P(x) = N_1 N_2 N_3 (x - xp)$, where N_1, N_2 and N_3 are linearizations of the flows $\phi_1(x_p, T_1)$, $\phi_2(x'_p, T_2)$ and $\phi_1(x''_p, T_3)$ respectively for the appropriate time T_1 on the trajectory starting at $x_p \in \Pi$ to respectively reach Σ for the first time, T_2 to pass between the first and second intersections of Σ, and T_3 to pass from Σ back to Π. However, this is not the case because, each time Σ is crossed transversally one must apply a correction to the Poincaré map. This correction is necessary because the time taken for trajectories at points x close to x_p to reach the discontinuity boundary Σ will in general vary, and so a small error will be made in assuming that the linearization required is T_1 for a constant time. The correction to this error is the *discontinuity map* in this case. The effect of the *DM* on the matrix N_1 is to multiply it by a so-called *saltation matrix* [2] [51] [50] [46]. A similar correction must be applied to the matrix N_2. Not introducing these corrections will in general result in wrong conclusions being made about the Floquet multipliers of the periodic orbit $p(t)$. Note in this case that, provided the form of the jump in the vector fields upon crossing Σ is described by a smooth function, then the discontinuity mapping, and the associated global Poincaré map around $p(t)$ will be smooth. Similar considerations apply to impacting hybrid systems where a periodic orbit $p(t)$ has a single impact with a discontinuity surface.

Now consider for a moment the special case where the velocity normal to Σ is zero, so that the periodic orbit *grazes* the discontinuity surface. Note that the trajectories from some initial conditions $x \in \Pi$ near x_p do not intersect Σ at all, whereas others intersect Σ with a low normal velocity. The discontinuity mapping in this case is the identity for orbits that do not cross Σ, but is defined as the local correction which must be applied to initial conditions that *do cross* Σ so that a Poincaré map can be applied as if Σ were not there. The effect of applying the DM to the map in this case is to introduce additional terms proportional to fractional powers of $\| x - x_p \|$, such as $\| x - x_p \|^{1/2}$ or $\| x - x_p \|^{3/2}$.

2.7.2 Types of discontinuity-induced bifurcations

Let us list some of the most commonly occurring types of codimension one DIBs (see Fig. 2.3):

Border collisions of maps. These are conceptually the simplest kind of non-smooth transition and occur when, at a critical parameter value, a fixed point of a non-smooth map lies precisely on a discontinuity boundary Σ. For maps locally piecewise-linear continuous there is now a mature theory for describing the bifurcation, that may result upon varying a parameter through such an event. Remarkably, the unfolding may be quite complex. Even in one dimension, it can be verified that a period-1 attractor jump to a period-n attractor for any arbitrary n, or to robust chaos without any periodic windows. In general n-dimensional maps only information on the simplest fixed points is known. There are some result in the study border collision bifurcations in maps with other degrees of singularity, including the discontinuous and square-root cases but there are more open questions than in the PWLC case.

Boundary equilibrium bifurcations. The simplest kind of DIB for flows occurs when an equilibrium point lies precisely on a discontinuity boundary Σ (see [24]). In Filippov systems and hybrid systems with sticking regions there is also the possibility of pseudo-equilibria which are equilibria of the sliding or sticking flow but are not equilibria of any of the vector fields of the original system. There are thus possibilities where the equilibrium lies precisely on the boundary between a sliding or sticking region and a pseudo-equilibrium turns into a regular equilibrium (either under direct parameter variation or in a fold-like transition where both exist for the same sign of the perturbing parameter). There is also the possibility that a limit-cycle may be spawned under parameter perturbation of the boundary equilibrium, in a Hopf-like transition.

Grazing bifurcations of limit cycles. One of the most studied DIBs in applications is caused by a limit cycle of a flow becoming tangent to (i.e. grazing) with a discontinuity boundary. One might naively think that this can be completely understood (upon taking an appropriate Poincaré section that contains the grazing point) as a border collision. However, for piecewise-smooth ODE this is not necessarily the case. Instead one has to analyze carefully what happens to the flow in the neighborhood of the grazing point. In fact, one can derive an associated discontinuity map. But, the link between the singularity of the map and the degree of discontinuity of the flow is a subtle one which also depends on whether the flow is uniformly discontinuous or not at the grazing point. This analysis explains what is observed at the grazing bifurcations in the impact and bi-linear oscillators.

Sliding and sticking bifurcations. There are several ways that an invariant set such as a limit cycle can do something structurally unstable with respect to the boundary of a sliding region in a Filippov system. The Poincaré maps so derived have the property of typically being non-invertible in at least one region of phase space that is due to the loss of information backward in time inherent in sliding motion. This analysis helps to explain the dynamics observed in the relay control and dry friction examples. In addition, in impacting systems sliding regions can be approached by infinite chattering sequences of impacts.

Boundary intersection crossing/corner collision. Another possibility for a codimension-one event in a flow is where an invariant set (e.g. a limit cycle) passes through the $(n-2)$-dimensional set formed by the intersection of two different discontinuity manifolds Σ_1 and Σ_2. There is also an special case where the jumps in vector field across Σ_1 and Σ_2 are such that their intersection can

be considered as a corner in a single discontinuity surface. This can explain the dynamics observed in the DC-DC converter.

Some possible global bifurcations. One example, that we shall mention in Chapter 5, involves a connection between the stable and unstable manifolds of pseudo-equilibria which are equilibria of a sliding flow but not of the individual flows either side of a discontinuity boundary. Topics include parameter and noise sensitivity; bifurcations that involve invariant tori grazing with a discontinuity surface; the similarity between grazing in piecewise-smooth flows and hybrid systems in the limit of large discontinuities; and codimension-two bifurcations.

2.8 Numerical methods

In general we referred to numerical analysis tools for differential equations. For smooth flows, there are broadly speaking two classes of numerical methods for investigating the possible dynamics for a range of parameter values namely; *direct numerical simulation*, and *numerical continuation* (also known as path-following). This classification also applies to piecewise-smooth systems, The rigorous numerical analysis of nonsmooth dynamical systems remains a theory that is far from complete.

2.8.1 Direct numerical simulation

When computing solutions to piecewise-smooth systems it is usually not possible to use general purpose software directly, as they typically use numerical integration routines that assume a high degree of smoothness of the solution. All numerical computations must make special allowance for the nonsmooth events which occur when a discontinuity boundary is reached. Simulation methods for nonsmooth systems fall broadly into two categories; *time-stepping* and *event-driven*. The former is most often used in many-particle rigid body dynamics written in complementarity form for which there can be a big number of constraints. For such problems, to accurately solve for events when one of the every one of the constraint functions becomes zero within each time-step and to subsequently re-initiate the dynamics would be prohibitively computationally expensive. In contrast, the basic idea of *time-stepping* is to only check constraints at fixed times. There are adaptations to standard methods for integrating ODE for complementarity systems, some of which are based on linear complementarity problem solvers that have been developed in optimization theory and that can be directly used on simulation of piecewise smooth dynamical systems. Clearly there are errors introduced by not accurately detecting the transition times, and therefore time-stepping schemes are often of low-order accuracy and can completely miss grazing events associated with low-velocity collisions. Several commercially available implementations of time-stepping algorithms, especially applied to rigid body mechanics, are available. In this thesis we are concerned with low-dimensional systems with a small number of discontinuity boundaries (no more than a couple). In this context, explicit event driven schemes are feasible, fast and accurate. In these methods, trajectories far from boundaries are solved using standard numerical integration algorithms for smooth dynamical systems (e.g. Runge- Kutta, BDF, etc.), then times at which a discontinuity boundary is hit are accurately solved. Here it is necessary to consider the capability of simulating sliding flow by defining a sliding vector fields. A key requirement of using an event-driven method is the ability to define each discontinuity boundary Σ_i as the zero set of a smooth function $H_i = 0$. Also we have to carefully define a set of transition rules at

each boundary if necessary, a reset rule R_i. Thus the time-integration of a trajectory of the dynamical system is reduced to the finding of a set of *event times* τ_k and boundary events $H_i^{(k)}$ such that $H_i^{(k)}(x(\tau_k)) = 0$. To achieve this we set up a series of monitor functions the values of which are computed during each step of the time-integration. If one of these functions changes sign during a time step, then one needs to use a root finding method to accurately find where $H_i = 0$. In this thesis, we have implemented an algorithm for time simulation of impacting systems with a single constraint, while more general algorithms for piecewise smooth dynamical systems has been implemented by Piiroinen and Kuznetsov [61].

Brute force bifurcation analysis

A powerful tool for the analysis of dynamical system is the capability of compute the bifurcation diagram for the set of attracting solutions using directly simulation. In this process, for a fixed parameter value, a set of initial points is chosen and the flow from each point is simulated a sufficiently long time for transients to decay, and for the ensuing dynamics to be deemed to have converged onto an attractor. This dynamics is then recorded, perhaps in a suitable Poincaré section. The parameter is then changed slightly and the same process repeated. Of course, one has to build up experience about the system in order to determine how long is a ẗsufficiently long time*:* However, an even more crucial question is to determine what set of initial conditions to take in order to converge to the various possible attractors. One approach here, which may minimize transient times, is to choose an initial condition for the new parameter value to be a point on the attractor at the previous parameter value. However, such an approach will necessarily miss the possibility of competing attractors present in the system. Thus, in general one should start from a range of different points within a suitably defined subset of the phase space from which one has a priori knowledge that the attractors of the system must lie. But how to choose such points within this set? The number of points should of course be chosen to be as large as possible for the computational time available. One could start with a regular grid of points, but there are advantages in choosing the initial points at random. That is, at each fixed parameter value, use a random number generator to choose initial conditions in uniformly. This way, the situation where attractors with small basins of attraction are missed consistently at each parameter value are likely to be avoided. We will refer to this method for computing bifurcation diagrams as a *Monte Carlo method*. The direct simulation method has many advantages in giving a quick and realistic picture of the bifurcation diagram of a system without assuming any a-priori structure about the number or form of the attractors.

2.8.2 Numerical continuation

Whilst having the merits described above, direct simulation suffers from the two disadvantages that it does not accurately pinpoint bifurcation points, and it only computes stable invariant sets (attractors). In order to accurately locate bifurcations it is sometimes necessary to compute unstable invariant sets. For example the collision of a limit cycle with an unstable equilibrium can cause the sudden disappearance of that limit cycle or one might want to detect the presence of an unstable limit cycle which at some subsequent parameter value may re-stabilize at a fold. Hence there is a complimentary need for direct methods for computing specific invariant sets of dynamical systems. These typically comprise methods for *numerical path-following* of these solutions as a parameter varies. These bifurcations might be regular bifurcations that can also occur

in smooth systems, or they might be DIBs associated with the changing of the event sequence of the orbit. For smooth systems, there is a large literature on such methods, see e.g. [43] for general explanations.

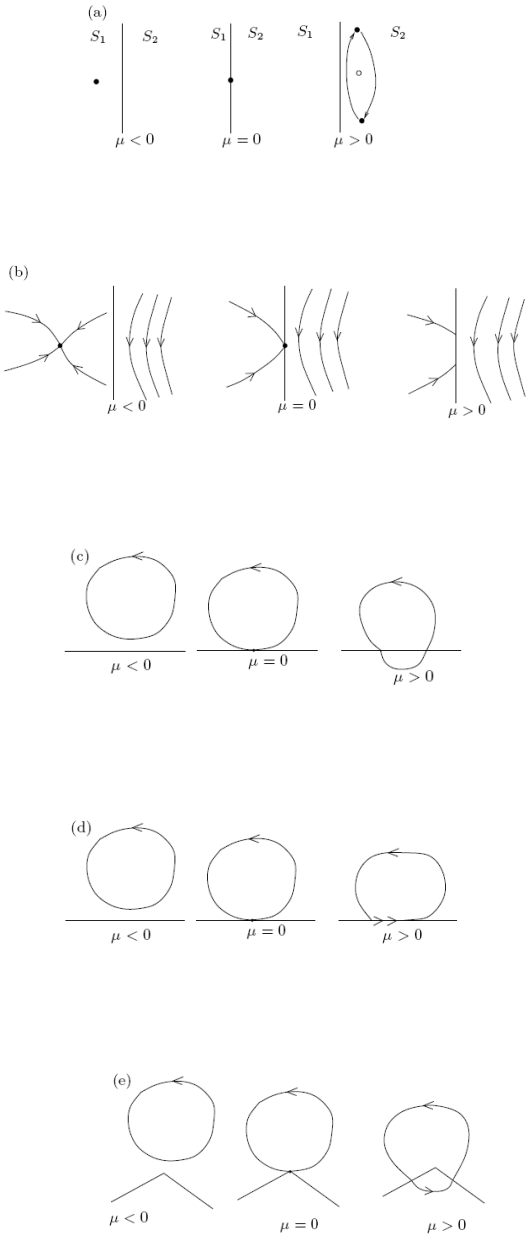

Figure 2.3: Main codimention-1 local bifurcations on nonsmooth dynamical systems.

Chapter 3

Impacting Systems

Contents

In this chapter we present an overview of the main strategies used in this thesis for the analysis of impacting systems in the context of the qualitative *Theory of Dynamical Systems* introduced in Chapter 2.

Rather than presenting a generalized theory for impacting systems (for which you can see [7]), we have chosen a simplified representative system, where we study many relevant issues on the modelling, simulation and stability analysis. The idea is to characterize systematically the properties inherent to impacting systems as well as the complexity associated to nonsmooth phenomena.

3.1 Impacting systems as a class of PWS dynamical system

Impacting systems are a class of piecewise smooth dynamical system often used to model mechanical systems with unilateral constraints on the position. In Sec. 2.6.4 we have given a general definition of such system as the composition of a smooth dynamical system plus an impact map of the form:

$$\begin{cases} x(t) = \varphi(x_0, t), & \text{if } x \in int\{\Omega\} \text{ or } x \in \partial\Omega^+, \quad (3.1a) \\ x \mapsto \rho(x), & \text{if } x \in \partial\Omega^- \text{ (Impact condition).} \quad (3.1b) \end{cases}$$

The evolution operator φ in (3.1a) determines the *free body dynamics*, and is associated to the vector field $\dot{x} = F(x)$. Here Ω is the *admissible space* with a boundary noted by $\partial\Omega$.

The unilateral constraint $\partial\Omega$ can be defined as the zero level set of a scalar function $H(x) : \mathbb{R}^n \to \mathbb{R}$ such that

$$\partial\Omega = \{x : x \in \mathbb{R}^n, H(x) = 0\},$$

with $H_x = \frac{\partial H}{\partial x}$ pointing towards the admissible space Ω. Notice that Ω is implicitly defined as the *epigraph* of H [7]. This is

$$\text{epi}(H) := \{(x, \alpha) : x \in \mathbb{R}^n, \alpha \in \mathbb{R}, H(x) \leq \alpha\} \subseteq \mathbb{R}^{n+1},$$

and then

$$\Omega := \{x : \exists (x, \alpha) \in epi(H)\}.$$

We define as *singularities* all nondifferentiable points on the boundary set, this is $\partial\Omega_c \subset \partial\Omega$. For example, all $x_c \in \partial\Omega$ are singularities, if the normal direction to $\partial\Omega$ is not uniquely defined. In this latter case, it is necessary to take into account additional local properties for the definition of a suitable impact map for corner points (see [28] [29] [7]). In chapter 6, we introduce the concept of *corner* in a boundary allowing different degrees of discontinuity on terms of the scalar function H and its derivatives.

The impact dynamics in (3.1b) is defined by $\rho : \partial\Omega \to \partial\Omega$ which is a *reset map* (or *impact map*) where the subset of the state variables that determines the position remain unchanged at impact, while the velocity variables jump as the relative components of velocity with the impacting surface change direction.

Contact dynamics.

As in Filippov systems, impacting systems may define implicitly some constrained dynamics. Impacting systems in particular may evolve in 2^m different modes that correspond to free and constrained motion for every one of the m variables that corresponds to the position (*i.e.* we assume that $m = n/2$). In general, the system evolving in a constrained mode can be modelled through an equivalent vector field F_s obtained from the interaction between the free flow and the constraint. We will refer to the constrained dynamical mode as *sticking* or *sliding* mode.

3.1.1 Impacting systems with a single constraint

If there is a single constraint we have two dynamical modes in continuous time, namely *free-motion* and *sticking-motion* plus the *impact dynamics*. The free–motion is defined

by a smooth evolution operator plus the impact dynamics. In general we are interested in the study of systems where the smooth dynamics can be defined through the solution of an initial value problem of ODEs such that

$$\frac{d}{dt}(\phi(x_0,t))\bigg|_{t=\tau} = F(\phi(x_0,\tau)), \tag{3.2}$$

where $x(0) = x_0$ is the initial state. Here the generic evolution operator in (3.1a) is defined as $\varphi := \phi$.

The impact dynamics is usually noted as $x^+ = R(x^-)$ where the superscripts "$-$" and "$+$" are used to distinguish between the pre- and post-impact state and R is some function of the system states. This definition does not exclude models with *rheonomic* constraints (*i.e.* with explicit dependence on time) since we assume that a time variable can be included in the state vector x. From now on, we will assume that the impact dynamics in (3.1b) can be expressed as a Newton–like percussion law of the form

$$\rho(x) := R(x) = x - Wv(x), \tag{3.3}$$

where for a single constraint, $W := [\ 0\ \cdots\ 1+r\ \cdots\ 0\ ]^T$, is a constant matrix with $0 \le r \le 1$ to model from plastic to elastic impacts, and v is the relative velocity at impact.

We can then write the dynamical system in (3.1a) (3.1b) as

$$\begin{cases} \dot{x} = F(x), & \text{if } H(x) > 0, \text{ or } H(x) = 0, v(x) > 0, \quad \text{(3.4a)} \\ x^+ = R(x^-), & \text{if } H(x) = 0, v(x) < 0. \quad \text{(3.4b)} \end{cases}$$

As mentioned above, it is possible for the system evolution to take place on the constraint or sticking motion. As shown in [54], the *sticking-motion* is given by the vector field

$$F_s(x) = F(x) + W\lambda(x), \tag{3.5}$$

where $H(x) = 0$, $v(x) = 0$ and $a(x) < 0$, with $\lambda(x) = -\frac{a(x)}{v_x W}$, and $a(x)$ is the acceleration.

As mention in Sec. 2.6.4, impacting systems may enter a sticking region directly (*i.e.* smoothly), or via a chattering sequence (also known as a *Zeno phenomenon*). Such a sequence begins if an impact occurs with low velocity and negative acceleration; this is $v(x^+) \ll 1$ and $a(x^+) < 0$. There follows an infinite sequence of impacts, of successively reduced velocity, which converges in finite time, onto a point in the sticking set. After the accumulation of such a sequence, the motion will evolve in the sticking dynamical mode as described above.

The study of nonsmooth dynamical systems is far from being complete and we are interested in some of the open issues. In particular in this thesis we are interested in the stability analysis of equilibria and limit cycles.

3.1.2 Nonsmooth phenomena

For impacting systems we are interested in two novel types of discontinuity induced bifurcations of equilibria and periodic orbits that occur on different processes, namely *Impact adding* and *Corner crossing*. Let us assume there is a periodic orbit O^* which is a solution (that may include impact events) of the system in (3.4). Then under parameter variations we will observe several bifurcation scenarios as follows :

Impact adding. (Grazing-corner) An *impact adding* of the orbit O^* occurs, when parameter variations imply new impacting events as: (see [67] [51])

- *Soft Impact* - Studied in the literature as *grazing impacts* (or *low velocity impacts*).
- *Hard Impact* - This case is characteristic of impacting systems with corners. As far as we are aware it has been not studied and we propose in Chapter 6 an analytical tools for the analysis.

Corner crossing. (Impacting singularities) A *corner crossing* DIB occurs when an impact belonging to the orbit O^* crosses a corner point $y_c \in \Omega^c$ under parameter variation. In chapters 5 and 6 we present a complete analysis of this bifurcating scenario for corners of degree 2.

3.1.3 Different formulations for impacting systems

Here we present two different formalisms that have been widely studied in the literature on nonsmooth systems. Namely, we will briefly present how an impacting system can be represented as:

- Complementarity system.
- Hybrid system.

An impacting system as a *complementarity system*

An impacting systems can be written as a complementarity problem for a Lagrangian nonsmooth dynamical system [44] [8] [1]. It consist of:

- a dynamical system with boundary conditions in terms of state variables,
- a set of input/output variables and their relations with the state variables,
- a set of nonsmooth laws which rely the input/output variable.

The evolution of a Lagrangian system for a general non linear case may be stated as follows :

$$M(q)\ddot{q} + Q(q, q') + F_{int}(q', q, t) = F_{ext}(t) + R, \tag{3.6}$$

where q is the generalized coordinates vector, $M(q)$ is the inertia term, $Q(q, q')$ is the non linear inertia term, $F_{int}(q', q, t)$ is the internal force of the system, $F_{ext}(t)$ is the given external force, $R \in \mathbb{R}^n$ is the force due the nonsmooth law.

In a general way, we denote the state of the system as

$$x = \begin{bmatrix} q \\ q' \end{bmatrix},$$

which is a vector of dimension n. The equation of evolution (3.6) may be reformulated in terms of the state vector as :

$$\dot{x} = F(x) + \begin{bmatrix} 0 \\ I \end{bmatrix} R, \tag{3.7}$$

which is a classical order one formulation for an ordinary differential equation.

Constrained variables. In a general way, the dynamical system is completed by a set of nonsmooth laws which do not concern directly the state vector. The set of such variables is denoted by y. In *Lagrangian* systems, the structure of these relations is very particular and we assume that they can be written as :

$$y := h(q), \tag{3.8}$$
$$\dot{y} := H(q)^T \dot{q}, \tag{3.9}$$
$$R := H(q)\lambda. \tag{3.10}$$

If we assume that these relations are non *holonomic* (*i.e.* independence with respect to the velocity q'), we derive the relative velocity as:

$$\dot{y} = \frac{\partial h(q,t)}{\partial q} q' + \frac{\partial h(q,t)}{\partial t}. \tag{3.11}$$

Furthermore, if the constraints is *scleronomic* (*i.e.* independence with respect to the time t) this relation leads to

$$\dot{y} = \frac{\partial h(q)}{\partial q} h(q) q'. \tag{3.12}$$

Indeed, the gradient $\nabla_q h(q) := \frac{\partial h(q)}{\partial q}$ corresponds to the constraint normal direction. We assume that the nonsmooth law for impacting systems has only a normal component which implies that the relation between λ and R is given by :

$$R = \nabla_q h(q)\lambda. \tag{3.13}$$

Impact Law. Several kind of nonsmooth laws may be formulated for a Lagrangian system. Here, we define just the unilateral contact law and the impact law.

The unilateral contact law may be formulated as follows :

$$0 \leq y \perp R \geq 0, \tag{3.14}$$

and the Newton–like impact law:

$$\text{if } y(t) = 0, \quad \dot{y}(t^+) = -r\dot{y}(t^-), \tag{3.15}$$

where $0 \leq r \leq 1$ to model form plastic to elastic impacts.

An impacting system as an *hybrid system*

The *hybrid* approach can be used to model dynamical systems where continuous and discrete variables are necessary to completely describe the dynamics of the system [38] [78] [37]. We are interested in the model of piecewise-smooth impacting systems where several dynamical modes may be implicitly defined on the boundaries (*i.e.* free and sticking motion). An impacting system as an *hybrid system* is defined by a 6-tuple $\{\mathcal{T}, \mathcal{X}, \mathcal{Q}, \varphi, \rho, \sigma\}$ in which

$\mathcal{T} = \mathbb{R}$, is a time set.

$\mathcal{X} := \Omega \in \mathbb{R}^n$, is the set of permissible states.

$\mathcal{Q}$, is the set of discrete (symbolic) states: *Impact*, *free* and *sticking* motion.

$\varphi : \mathcal{T} \times \mathcal{X} \times \mathcal{Q} \to \mathcal{X}$, is a continuous evolution operator for each dynamical mode.

$\rho : \mathcal{T} \times \mathcal{X} \times \mathcal{Q} \to \mathcal{X} \times \mathcal{Q}$, is a discrete evolution operator or discrete dynamics.

$\sigma : \mathcal{T} \times \mathcal{X} \times \mathcal{Q} \to \mathbb{R}$, is a discrete event generating function (impacting boundaries).

We have several remarks for impacting systems with a single constraint:

- There are three different dynamical modes: *Impact*, *free* and *sticking* motion. This is $\mathcal{Q} = \{S_i, S_f, S_s\}$.
- We assume that the evolution for the free–motion state is given by $x(t) = \phi(t, x_0)$, where ϕ is the solution of the initial value problem $\dot{x} = F(x, t)$ with initial condition $x(0) = x_0$.
- The transition from free-motion to sticking-motion can occur through a grazing orbit (smoothly) or through a chattering sequence product of the interaction between the impact and free dyanmics.
- Function σ can assume any arbitrary shape (as for example corners).

3.2 Simulation of impacting system

There are two main numerical schemes for simulation of impacting systems: *Event driven* and *Time stepping*. The *event driven* scheme is based on an hybrid formulation while the *time stepping* scheme uses fixed step integration computing impact dynamics by using quadratic programming to solve a complementarity problem. Next, we will briefly present the main features of the two approaches.

3.2.1 Event driven scheme

Let us assume we are interested in the simulation of an impacting system with a single constraint in (3.4). In this case it is possible to determine the initial dynamical mode from the definition as:

$$\begin{cases} \dot{x} = F(x) & \text{if } H(x) > 0, \text{ or } H(x) = 0, v(x) > 0, \\ & \text{or } H(x) = 0, v(x) = 0, a(x) > 0. \\ x^+ = R(x) & \text{if } H(x) = 0, v(x) < 0, \\ \dot{x} = F_s(x) & \text{if } H(x) = 0, v(x) = 0, a(x) \leq 0, \\ \text{Not valid.} & \text{if } H(x) < 0. \end{cases} \tag{3.16}$$

For simplicity, we assume that the initial conditions satisfy conditions for free–motion. After determining the initial dynamical mode we now need to define how the system commutes from one mode to the other. Fig. 3.1 shows the control flow of the algorithm developed for simulation of impacting systems. There are three basic operations: *Free Dynamics*, *Impact Dynamics* and *Sticking Dynamics*.

Different from many other approaches for the simulation of impacting system that use the hybrid systems approach we do not avoid the numerical problems that chattering (or Zeno behaviour) possesses, but instead we are using a recently developed method (see [55] for further details and the code attached to the thesis) to deal with this very specific situation. The main idea with this method is to introduce a *chatter map* that maps the state forward in time when the impacts are accumulating. This means that every time there is an impact and the relative acceleration between two bodies are negative the method checks whether the chatter map can be applied. The method also makes sure that the map does not introduce a bigger error than some tolerance given by the user. After the chatter map has been applied the two object that were impacting with each other will now be in contact until the relative acceleration between the two objects becomes positive (*Release detect*). Using this strategy we have computed the different types of bifurcation diagrams presented in Chapter 4. We have chosen MATLAB's ODE solvers (and mainly Rk45, which is a fourth order Runge-Kutta method) with the built-in event location routines to detect the crossings of the discontinuity surfaces. Such event location routines find the zero of the specified functions called *event functions* and the direction of the zero crossing. The values of the relative and absolute tolerance that we have considered to implement the integration method are both 10^{-12}. We have also used a maximum integration step whose value have been 10^{-3}.

3.2.2 Time stepping scheme

Here we present the numerical strategy used in the SICONOS platform for the simulations of nonsmooth systems, this is the time discretization method for nonsmooth Lagrange dynamical systems in (3.6). The equation may be reformulated equivalently in terms of an integral over a time step $[t_i, t_{i+1}]$ of length h such that :

$$\int_{[t_i,t_{i+1}]} Mq'' + Cq' + Kq\,dt = \int_{[t_i,t_{i+1}]} F_{ext}(t)\,dt + \int_{[t_i,t_{i+1}]} R\,d\nu. \tag{3.17}$$

Due to the non smooth character of the motion, the first term is integrated by a first order scheme (backward Euler-like) such that :

$$\int_{[t_i,t_{i+1}]} Mq''\,dt \approx M(q'(t_{i+1}) - q'(t_i)). \tag{3.18}$$

For simplicity sake, we note the approximation of q and q':

$$q'_{i+1} \approx q'(t_{i+1}), q'_i \approx \dot{q}(t_i). \tag{3.19}$$

For the other terms, a θ-method is used :

$$\int_{[t_i,t_{i+1}]} Cq' + Kq\,dt \approx h\left[\theta(Cq'_{i+1} + Kq_{i+1}) + (1-\theta)(Cq'_i + Kq_i)\right], \tag{3.20}$$

$$\int_{[t_i,t_{i+1}]} F_{ext}(t)\,dt \approx h\left[\theta F_{ext}(t_{i+1}) + (1-\theta)F_{ext}(t_i)\right]. \tag{3.21}$$

For the term which contains the reaction force, we state a new variable such as :

$$R_{i+1} = \frac{1}{h}\int_{[t_i,t_{i+1}]} R\,d\nu. \tag{3.22}$$

The displacement is integrated through the velocity with :

$$q_{i+1} = q_i + h\left[\theta q'_{i+1} + (1-\theta)q'_i\right]. \tag{3.23}$$

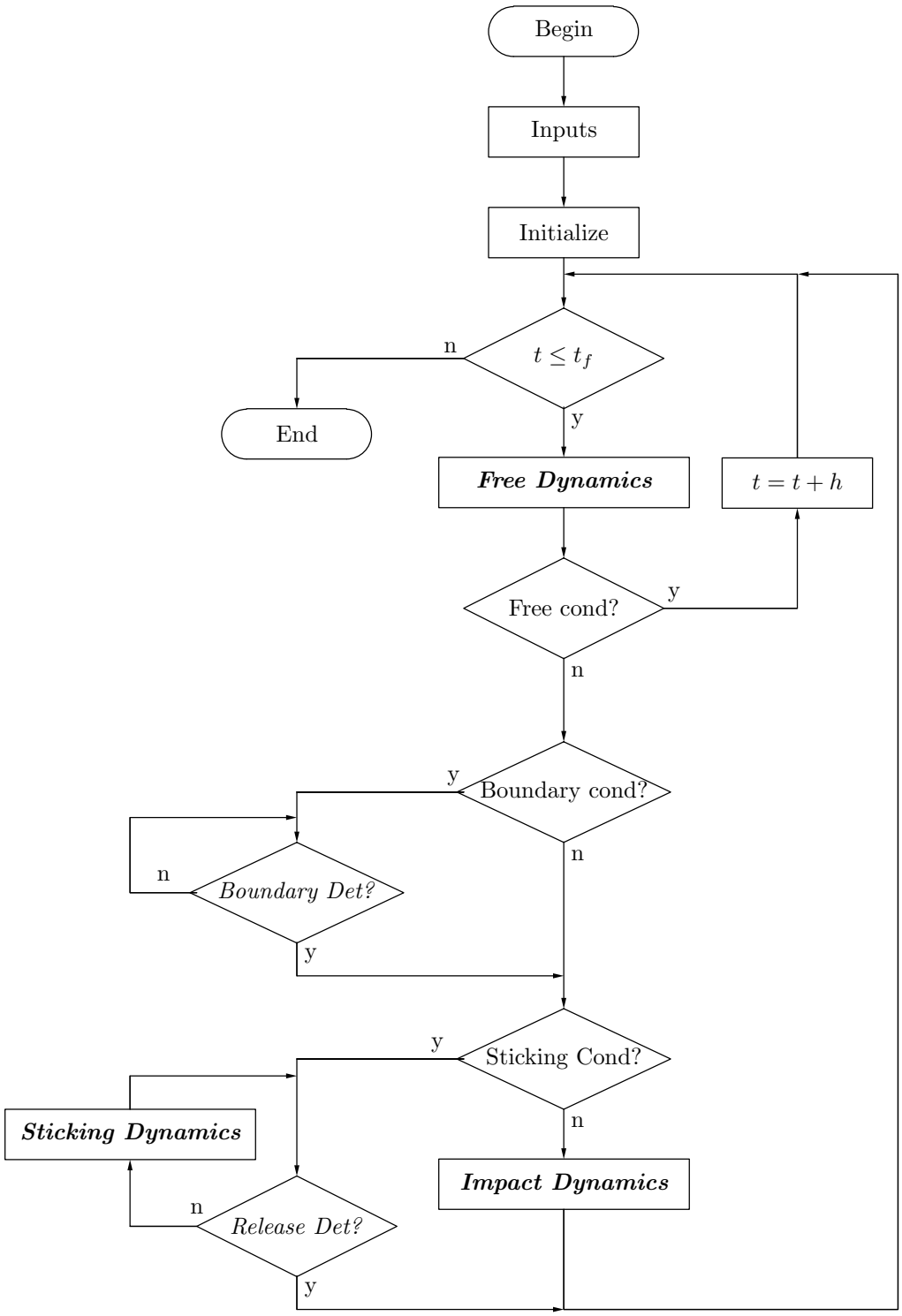

Figure 3.1: Control flow diagram for an event driven numerical scheme.

Finally, we obtain the time discretized equation of motion as follows :

$$\begin{aligned}\left[M + h\theta C + h^2\theta^2 K\right](q'_{i+1} - q'_i) = \\ - hCq'_i - hKq_i - h^2\theta K q'_i + h\left[\theta F_{ext}(t_{i+1}) + (1-\theta)F_{ext}(t_i)\right] + hR_{i+1},\end{aligned} \quad (3.24)$$

which can be written :

$$q'_{i+1} = q'_{free} + hNR_{i+1}, \quad (3.25)$$

where

$$N = \left[M + h\theta C + h^2\theta^2 K\right]^{-1},$$

$$\begin{aligned}q'_{free} = \\ q'_i + N\left[-hCq'_i - hKq_i - h^2\theta K q'_i + h\left[\theta F_{ext}(t_{i+1}) + (1-\theta)F_{ext}(t_i).\right]\right].\end{aligned} \quad (3.26)$$

The free velocity q'_{free} corresponds to the velocity of the system without any constraints.

Time discretization of the relations. The Time discretization of the relations is fully implicit and may be written as :

$$\begin{aligned} y_{i+1} &= H^T q_{i+1} + b, & (3.27)\\ \dot{y}_{i+1} &= H^T q'_{i+1}, & (3.28)\\ R_{i+1} &= H\lambda_{i+1}, & (3.29)\end{aligned}$$

Time discretization of the non smooth laws. A natural way of discretizing the unilateral constraint leads to the following implicit discretization :

$$0 \le y_{i+1} \perp \lambda_{i+1} \ge 0, \quad (3.30)$$

In the Moreau's time–stepping [1], we use a reformulation of the unilateral constraints in terms of velocity (3.30) :

$$\text{If } y(t) = 0, \text{ then } 0 \le \dot{y} \perp \lambda \ge 0. \quad (3.31)$$

which leads to the following discretization:

$$\text{If } y^p \le 0, \text{ then } 0 \le \dot{y}_{i+1} \perp \lambda_{i+1} \ge 0, \quad (3.32)$$

where y^p is a prediction of the position at time t_{i+1}, for instance, $y^p = y_i + \frac{h}{2}\dot{y}_i$.

We introduce now the Newton impact law, we consider an equivalent velocity defined by

$$\dot{y}^e_{i+1} = \dot{y}_{i+1} + r\dot{y}_i \quad (3.33)$$

and we apply the constraints directly on this velocity :

$$\text{If } y^p \le 0, \text{ then } 0 \le \dot{y}^e_{i+1} \perp \lambda_{i+1} \ge 0 \quad (3.34)$$

3.2.3 Numerical analysis

As mentioned in Chapter 2, Poincaré maps are useful for the qualitative analysis (bifurcations) of periodic orbits. Since we have a high quality simulator we also want to be able to perform the bifurcation analysis of stable solutions using brute force simulation. By using the event generating function in the case of the event-driven numerical approach (or the complementarity condition in the time-stepping approach), we record the complete state of the system whenever an impact occurs. This recorded data can be employed to estimate a map from one impact to the next *i.e. a Poincaré impact map* or simply an *impact map*. Another way of characterizing periodic orbits is through the definition of a *Poincaré stroboscopic map* (or *stroboscopic map*) which is a fixed time map obtained numerically by sampling the state of the system at a fixed rate conveniently defined by the user; for example in periodically forced systems we will usually chose a sampling period that is an integer multiple of the forcing period.

We can then use a numerical simulation to study the structural stability of stable periodic orbits, by plotting the projections of the orbits on the *Poincaré* sections (impact and stroboscopic) associated to the corresponding maps. Now, under parameter variations we can graphically capture qualitative changes (bifurcations) on the periodic solutions as follow:

1. *Impact Map*
   For a codimension-one analysis, we have that μ is a one dimension parameter to be varied within the model, θ_i is the phase at impact (in relation with a complete period of the forcing input), v_i is the velocity of the particle at impact, then we need the plot of:

   (a) μ *vs.* θ_i, *Bifurcation Diagram at impact.*

   (b) θ_i *vs.* v_i, for $\mu = \mu_c$ (constant) *Phase map at impact.*

2. *Stroboscopic Map*
   For a codimension-one analysis, we have that θ_s define a *Poincaré section* Π_s, μ is a one dimension parameter to be varied within the model, v_s and p_s are the velocity and position of the particle when crosses Π_s, then we need the plot of:

   (a) μ *vs.* p_s *Bifurcation Diagram at* Π_s

   (b) p_s *vs.* v_s, for $\mu = \mu_c$ (constant) *Phase Map at* Π_s

3.3 Cam-follower system as a representative example

We propose the use of a cam–follower system as a benchmark example for the qualitative study of dynamical behavior in impacting systems, since it collects most relevant properties described in the previous sections. The cam–follower system is inspired from a widely used mechanical device consisting of two moving parts, namely a rotating part called cam and a longitudinal moving part called follower [57]. See Fig. 3.2 for the schematic diagram. It is assumed that the cam excited by an external constant force producing a constant rotational speed, since we assume no effects on the cam dynamics coming from the follower. We also assume the follower dynamics can be modelled as a single degree of freedom damped oscillator. We finally assume that the geometrical construction of the mechanical system is such that the cam imposes a rheonomic (i.e. time dependant) constraint to the follower position, with interaction modelled by a Newton

like impact law or equivalent sliding vector field whenever the cam and the follower are detached or in contact. Note the distinction between the cam–follower system and the driven impact oscillator since most of the research work done so far has been focused mainly on the qualitative behavior under smoothly driven impact oscillators [67] [10] [51] [32]. Instead in the cam–follower system it comes naturally from the cam geometry that the driven force can be non smooth.

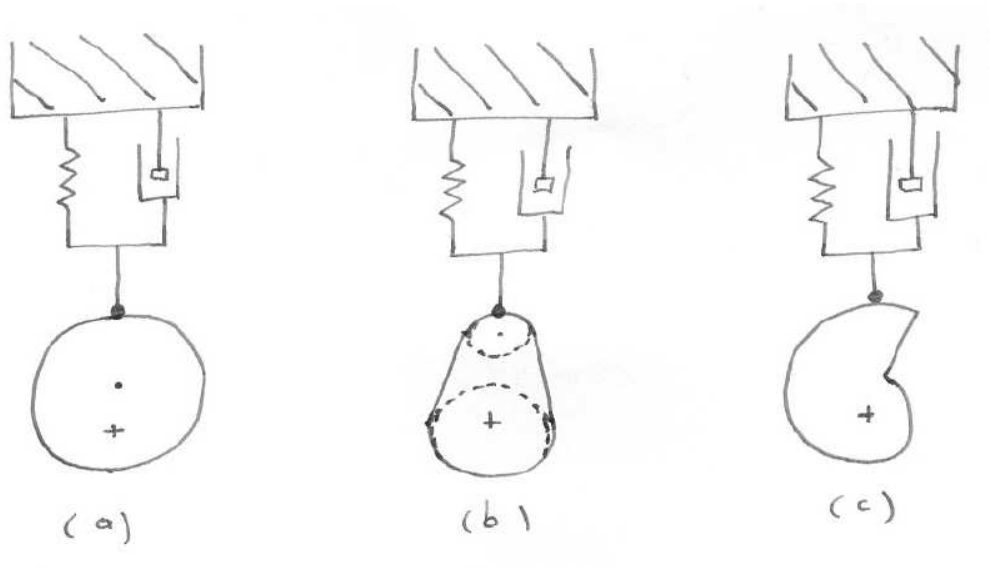

Figure 3.2: Cam-Follower system with different cam profiles

Figures 3.2 and 3.3 presents different shapes and characteristic position (lift), velocity and acceleration for cam profiles from continuous lift profile,to those with up to fourth order discontinuities.

Cam-follower as a piecewise smooth dynamical system

It is possible to completely describe the cam–follower system as a driven impact oscillator plus an impact law. Let us note u the position of the follower and c the position of the cam on the admissible space of the follower (lift profile) in a common inertial frame. We define the variables $q = u - c$ (relative position) and $q' = u' - c'$ (relative velocity), then the free–motion will be completely described by the smooth vector field defined through a second order differential equation of the form

$$\mu\ddot{q} + \zeta q' + \kappa q = -\left(\mu\ddot{c} + \zeta c' + \kappa c\right), \qquad \text{if} \quad q > 0 \text{ or } q = 0,\ q' > 0, \tag{3.35}$$

and the Newton like impact dynamics of the form

$$q'^{+} \quad = \quad -r q'^{-}, \quad \text{if} \quad q = 0,\ q' < 0. \tag{3.36}$$

Further we can write (3.35) and (3.36) as function of the state variables in the form of an order one system of ODEs plus an impact map

$$\begin{cases} \dot{x} = F(x), & \text{if } H(x) > 0, \text{ or } H(x) = 0, v(x) > 0, \quad (3.37a) \\ x^+ = R(x^-), & \text{if } H(x) = 0, v(x) < 0. \quad (3.37b) \end{cases}$$

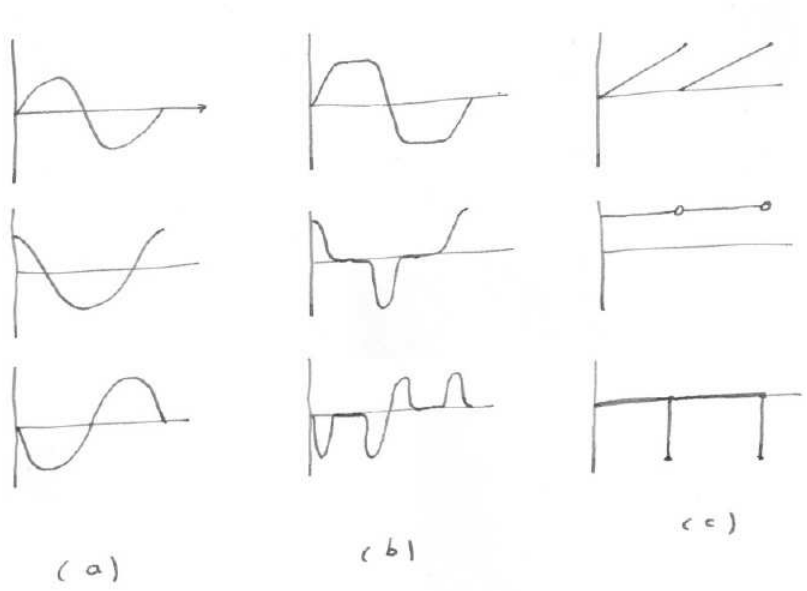

Figure 3.3: (From top to bottom) Cam lift, velocity and acceleration for the three different cases.

with $R(x^-) = x^- - WH_xF(x^-)$, where

$$\begin{aligned} x &= \begin{bmatrix} x_1 \\ x_2 \\ x_3 \end{bmatrix} = \begin{bmatrix} q \\ q' \\ t \end{bmatrix}, \\ F(x,t) &= \begin{bmatrix} x_2 \\ -\frac{\zeta}{\mu}x_2 - \frac{\kappa}{\mu}x_1 + \frac{\hat{f}(x_3)}{\mu} \\ 1 \end{bmatrix}, \\ R(x^-) &= \begin{bmatrix} x_1^- \\ -rx_2^- \\ x_3^- \end{bmatrix}, \\ H(x) &= x_1, \\ W &= \begin{bmatrix} 0 \\ 1+r \\ 0 \end{bmatrix}. \end{aligned}$$

Notice that that a lift profile $c(t) \in \mathcal{C}^k$ implies $F \in \mathcal{C}^{k-2}$.

3.3.1 Simulation of a cam-follower system

We have performed the simulation of the cam–follower system for different values of the cam rotational speed with the SICONOS software package using a time-stepping numerical scheme with step size ($h = 1e^{-4}$) and an event-driven scheme with minimum step size ($h_{min} = 1e^{-12}$). Fig. 3.4 and 3.5 show the time simulations for different values of the cam rotational speed and Fig. 3.6 show the chaotic attractor at $rpm = 660$ for impact and stroboscopic Poincaré sections. A more extensive investigation of the dynamics of cam–follower systems will be presented in Chapter 4.

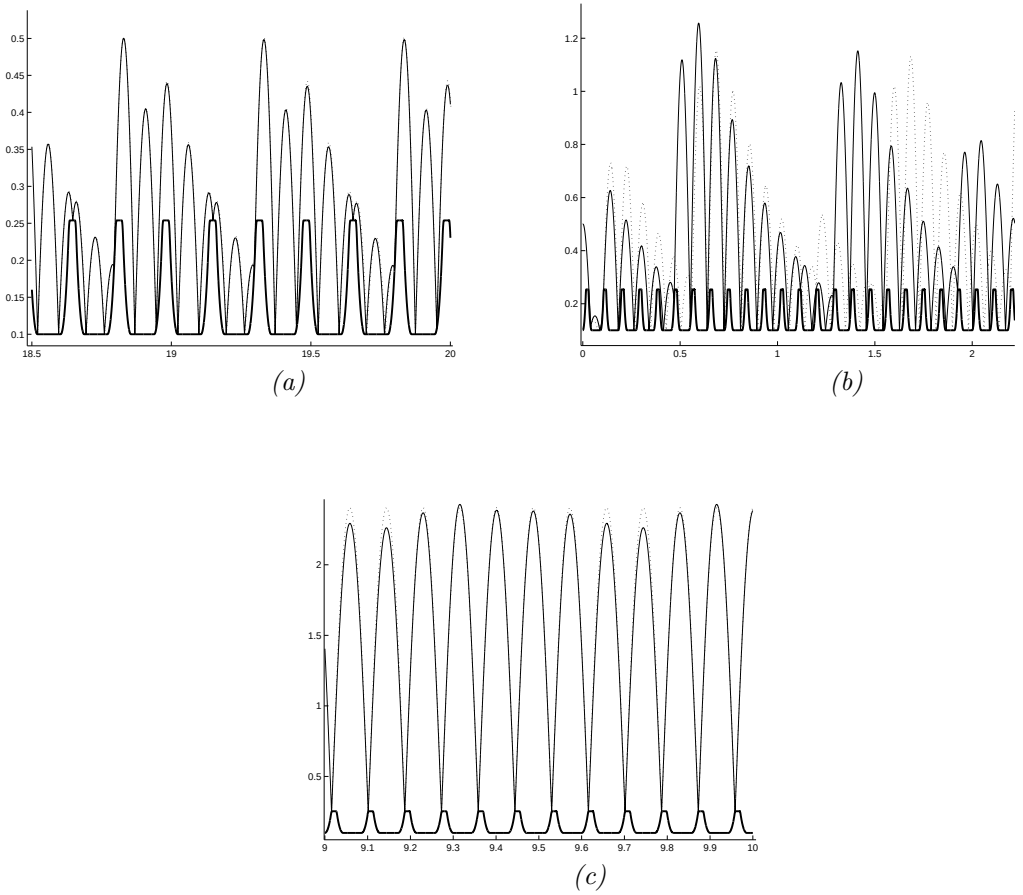

Figure 3.4: Time series using SICONOS platform. Time-stepping scheme (continuous line). Event-driven scheme (dashed line) *(a)* rpm=358. *(b)* rpm=660. *(c)* rpm=700.

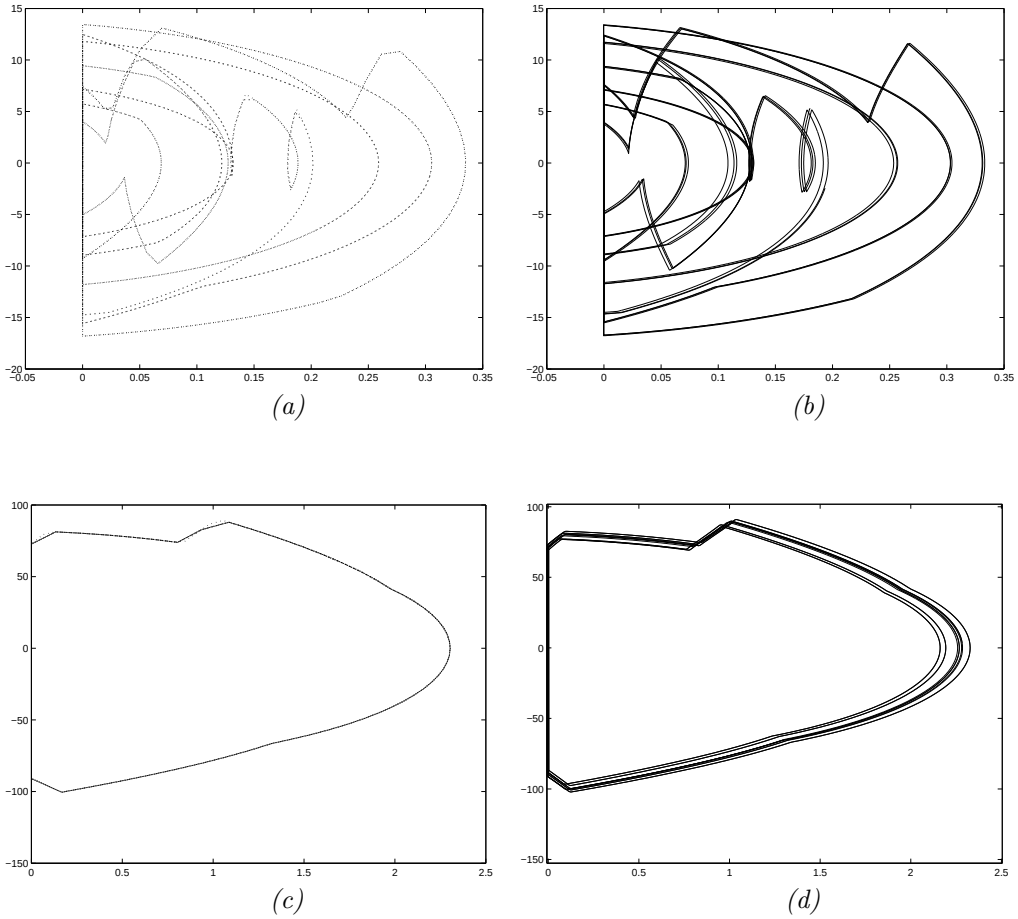

Figure 3.5: State space comparison using SICONOS platform. *(a)* rpm=358. Event Driven *(b)* rpm=358. Time Stepping ($h = 1e^{-4}$)*(c)* rpm=700. Event Driven *(d)* rpm=700. Time Stepping ($h = 1e^{-4}$)

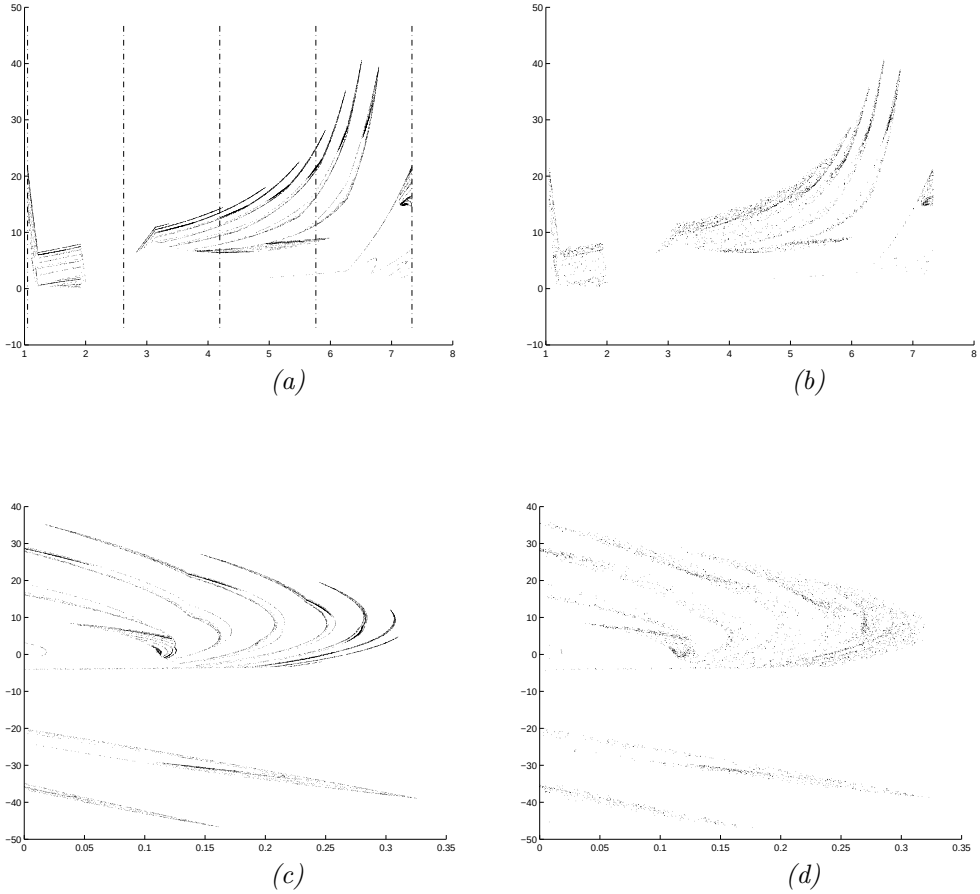

Figure 3.6: Attractors comparison using SICONOS platform at rpm=660. *(a)* Impact map. (Event Driven) *(b)* Impact Map. Time Stepping ($h = 1e^{-4}$)*(a)* Stroboscopic map. (Event Driven) *(b)* Stroboscopic Map. Time Stepping ($h = 1e^{-4}$)

3.4 Limit cycle analysis in impacting systems

As an illustrative example we propose to study the stability of piecewise smooth periodic orbits (*i.e.* periodic orbits with impacts) in the cam–follower system. We denote an orbit as $\mathcal{O}(n, m)$, when is a period nT orbit with m impacts per period; where T is the period of the forcing input.

3.4.1 Existence of $\mathcal{O}(1, 1)$ periodic orbits

We use the concept of map to define a discrete function P associated to the system in continuous time in such a way that

$$x_{t_s+T} = P(x_{t_s}, T), \tag{3.38}$$

where x_{t_s} is the state of the system at an arbitrary time t_s and T defines the period of the mapping. This is nothing else but a stroboscopic sampling where is usually convenient to choose the sampling period equal to the forcing period.

In general, it is possible to define the global map P as a composition of two kinds of maps in which there is one that takes care of discontinuities (P_ρ) and the other one which will account for the continuous flows (P_ϕ). For example a $\mathcal{O}(1, 1)$ orbit can be expressed as

$$x_{t_s+T} = P_\phi(P_\rho(P_\phi(x_{t_s}, \tau), 0), T - \tau), \tag{3.39}$$

where τ is the impact time referred to the previous sampling t_s. Figure 3.7 presents an schematics for the map composition.

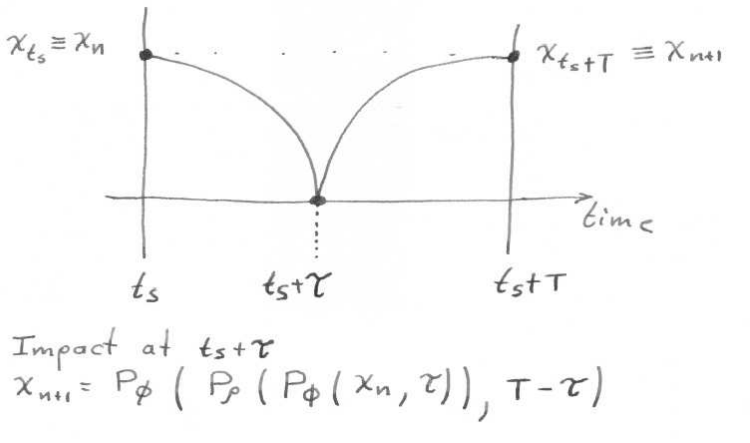

Figure 3.7: The map composition for a $\mathcal{O}(1, 1)$ Orbit

Notice that P_ϕ depends only on the free body dynamics and therefore from (3.2) can be written as

$$P_\phi(x, t) = \phi(x, t).$$

Furthermore, P_ρ provides an instantaneous (zero time) mapping on the relative velocity and can be directly obtained from (3.4b) as

$$P_\rho(x, 0) = R(x).$$

Then, we can write (3.39) as

$$x_{t_s+T} = \phi(R(\phi(x_{t_s}, \tau)), T - \tau). \tag{3.40}$$

Now we have that a fixed point in (3.40) (associated to the periodic orbit of the system in continuous time), will satisfy $x_{t_s} = x_{t_s+T} \equiv x_{t_s}^{ref}$.

If we choose $\tau = T$ then, existence of a $\mathcal{O}(1,1)$ will be obtained by solving for t_s the equation

$$R(\phi(x_{t_s}^{ref}, T)) - x_{t_s}^{ref} = 0.$$

Finally, it is necessary to verify the validity for every solution given that is possible to find some solutions for the equation that allows penetration of the bodies.

3.4.2 Asymptotic stability of periodic orbits with impacts

Let us assume we have a periodic orbit ($\mathcal{O}^{ref}(1,1)$) depicted with a solid line in Fig. 3.8(a). In the previous section we have shown that we can arbitrary choose the stroboscopic sampling $t_s = 0$ exactly at impact with period T and the impacting time τ^{ref}. We also have that $x(0) = x_0^{ref} \in \mathcal{O}^{ref}$ is the state of the system at $t = 0$ after impact. Then we are interested in the asymptotic behavior of the perturbed orbit ($\mathcal{O}$) depicted as dashed line in Fig. 3.8(a), with initial condition $x(0) = x_0 \notin O^{ref}$. In the depicted example the perturbed orbit (dashed) approaches asymptotically the continuous one (solid).

Fig. 3.8(b) represents the construction of a global map $\mathcal{P}$ that will allow us to determine the asymptotic stability near the orbits $\mathcal{O}^{ref}$. $\mathcal{P}$ will map an initial state x_0 to a final state x_1 after time T, in general we have that

$$x_{n+1} = \mathcal{P}(x_n).$$

Now, $\mathcal{P}$ can be defined as a composition of two different maps. The first map Φ will be associated to the stroboscopic sampling and the free flow (*i.e.* without impacts). The other map D is a zero time discontinuous mapping depending on the perturbation and the impact, specifically:

$$\begin{aligned} x_d &= \Phi(x_0), \\ x_1 &= D(x_d). \end{aligned}$$

As sketched Fig. 3.8(b), we can directly define Φ as an stroboscopic mapping to determine x_d as function of the initial state x_0 and the sampling period T:

$$x_d = \Phi(x_0) = \phi(x_0, T). \tag{3.41}$$

We can also construct the discontinuity mapping D as a composition of the flow from point x_d in the perturbed orbit till x_τ^- which is the pre-impact state, *i.e.*

$$x_\tau^- = \phi(x_d, t_i(x_d)),$$

then using the impact law presented at (3.4b) we can determine the post-impact state

$$x_\tau^+ = R(x_\tau^-, \tau),$$

and finally flowing back to the stroboscopic section to determine x_1, with

$$x_1 = \phi(x_\tau^+, -t_i(x_d)).$$

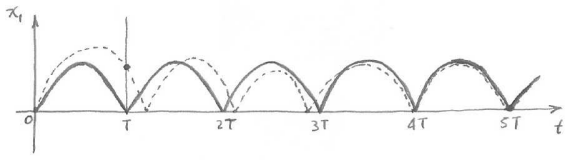

(a)

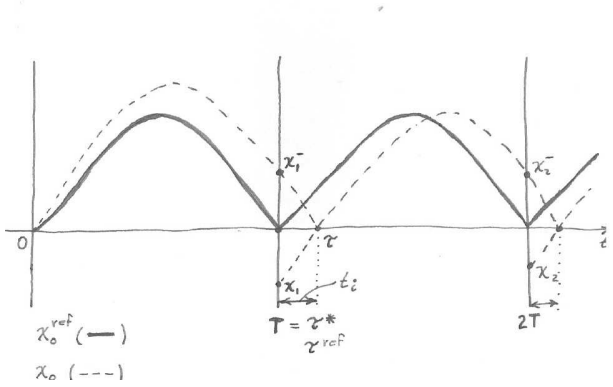

(b)

Figure 3.8: (a) Continuous is the (1,1) Orbit, dashed is a perturbed orbit. (b) Construction of the global map where $t_i = \tau - T$.

After the composition, we can write the zero time discontinuity mapping D as

$$x_1 \quad = D(x_d) \quad = \phi(R(\phi(x_d, t_i(x_d))), -t_i(x_d)). \tag{3.42}$$

At this point we can write a complete expression for the stroboscopic map $\mathcal{P}$ as

$$x_1 \quad = \quad \mathcal{P}(x_0) = D(\Phi(x_0)) \tag{3.43}$$

Given that (3.43) is in general a nonlinear map, the local stability characteristics of the discrete system are governed, to the lowest order, by the linearization about the reference fixed point x_0^{ref}:

$$\mathcal{P}(x_0) = \mathcal{P}(x_0^{ref}) + \mathcal{P}_x(x_0^{ref})(x_0 - x_0^{ref}) + o(\|x_0 - x_0^{ref}\|),$$

where

$$\mathcal{P}_x(x_0^{ref}) = D_x\Phi_x,$$

$$D_x(x_0^{ref}, \tau^{ref}) = R_x + \frac{(F^+ - R_xF^-)H_x}{H_xF^-},$$

and $\Phi_x = \phi_x(x_0, T)$ can be computed numerically from the variational equation for the Jacobian $J(t) = \phi_x(x_0, t)$ as

$$\dot{J} = F_x(x)J.$$

The complete derivation of $\mathcal{P}(x)$ will be presented in Chapter 5.

Chapter 4

Complex Dynamics in the Cam–Follower System

Contents

This chapter is devoted to give a brief overview of the complex dynamics of a representative cam-follower system, already introduced in Sec. 3.3 The aim is to present the complexity exhibited by the cam–follower because of the nonsmooth nature of the cam profile; namely the qualitative changes of the system behavior under parameter variations, for solutions with impacts near to discontinuity points. Cam-follower systems are a particularly important class of mechanical systems with displacement constraints widely used for the operation of various machines and mechanical devices [57]. Usually, their purpose is to actuate valves or other mechanisms through the movement of a follower forced by a rotating cam. For example, all types of automated production machines, including screw machines, spring winders and assembly machines, rely heavily on this kind of systems for their operation. One of the most common application is to the valve train of internal combustion engines (ICE) [31], where the effectiveness of the ICE is based on the proper working of a cam-follower system. A schematic figure of a single valve for a typical pushrod type engine is presented in Fig. 4.1. Here, the cam rotation results in a linear motion imparted to the valve. The valve spring in the system provides the restoring force necessary to maintain contact between the components.

To guarantee that the follower moves as required, it is important in applications to carefully design the cam profile. Different cam geometries are used in practice ranging from circular cams to highly complex cam profiles. In general, there is now a large variety of alternative methods to select the cam profile. For example, by using constrained

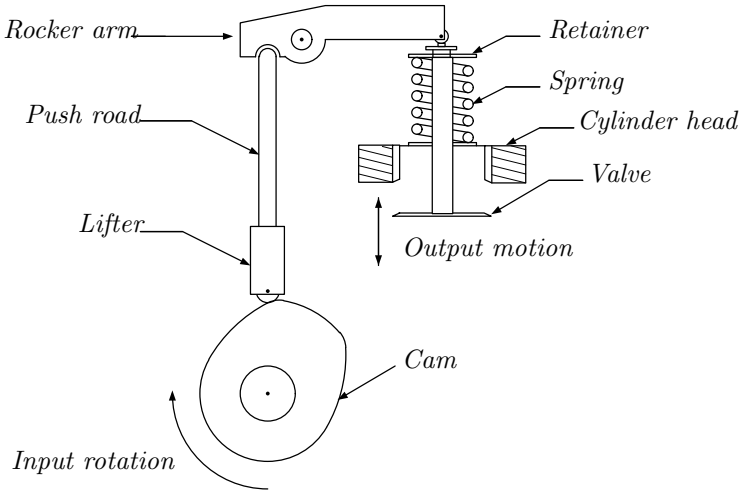

Figure 4.1: Valve train configuration.

optimization algorithm, it is possible to use splines to obtain the cam geometry from the desired motion that the cam is required to impart on the follower (see for examples [12] and [23]). This often means that while the cam has a continuous displacement profile, it might have discontinuities in its acceleration [58].

It has been observed that, as the cam rotational speed increases, the follower can detach from the cam. This causes the onset of undesired behavior associated to impacts taking place between the follower and the cam. For example, in automotive engines this phenomenon can seriously deteriorate the engine performance as the valves can close with abnormally high velocity and even bounce off the seat (valve floating and bouncing) [42, 72, 13]. To avoid this phenomenon, a large spring force and preload are applied to the follower [64]. This often causes an increase in the contact force, which induces higher stresses possibly leading to early surface failure of the parts. The resulting high friction valve train reduces the efficiency of the engine system [74]. In general, cam-follower systems can be thought of as impact oscillators with moving boundaries [41, 57, 22, 77]. While the dynamics of impact oscillators with continuous forcing has been the subject of many papers in the existing literature (see [59], [14], [9][10]), the possible intricate bifurcation behavior of impact oscillators with discontinuous forcing was discussed only recently, as for example in [11]. As shown later in Chapter 5, it was proposed that discontinuously forced oscillators can show a novel bifurcation phenomenon unique to their nature which was termed as *Corner-Impact Bifurcation* (CIB). Namely, in [11] the dynamics are studied of an impact oscillator forced by a discontinuous sinusoidal forcing of the form $f(t) = A|\sin(\omega t)|$. It was shown that, under variation of the system parameters, abrupt changes of the system qualitative behavior are observed when an impact occurs at a point where the forcing velocity is discontinuous (a corner-impact bifurcation point).

The observed behavior was explained in terms of appropriate local maps. In particular, by using the technique of discontinuity-mappings recently proposed in [14] and [20], it was suggested that a corner-impact bifurcation of the oscillator corresponds to a border-collision of a fixed point of the associated Poincaré map. An important difference was highlighted between corner-impact bifurcations and other types of discontinuity-induced bifurcations [19] in impacting systems such as grazing of limit cycles [51],[73],[46],[17], [60],[45]. While the normal form map of a grazing bifurcation is typically characterized by a square root singularity [51], the local normal form map associated to a corner-impact bifurcation was shown to be a piecewise linear map with a gap such as those studied in [33]. Hence, as explained in [11], an appropriate classification method needs to be used to investigate this novel class of bifurcations. Here, we present for the first time an in–depth analysis of the complex behavior of cam–follower systems and explain the role of CIBs in organizing their dynamics.

4.1 Modelling

The formulation of an appropriate model for a cam-follower system can be a challenging task for most applications. Various models with different degrees of complexity have been proposed and extensively studied. They range from simple models with one degree-of-freedom (DOF) such as described in [41] to complex models characterized by many DOFs, as for example the 21 DOFs model studied in [66] where additional effects of camshaft torsion and bending, backlash, squeeze of lubricant in bearings are included. Nevertheless, there is a general agreement in the literature, confirmed by experiments, that a lumped parameter single degree-of-freedom model is adequate to represent the main qualitative features of the dynamic behavior of the system of interest [6],[41],[3],[22].

The schematic diagram of the cam-follower system under investigation is shown in Fig. 4.2. We consider the following second order equation to model the free body dynamics of the follower away from the cam,

$$mq''(t) + bq'(t) + kq(t) = -mg, \qquad \textit{if } q(t) > c(t),$$

where m, b, k and g are constant positive parameters representing the follower mass, viscous damping, spring stiffness and the gravitational constant respectively. At this point and for the rest of this thesis we choose some specific values for the system parameters The state of the follower is given by the position $q(t)$ and the velocity $q'(t)$. The cam position is given by $c(t)$ and we assume that the follower motion is constrained to the phase-space region where $q(t) > c(t)$.

The dynamic behavior, when impacts occurs, is modelled via a Newton restitution law as [7],[44],[26]:

$$q'(t^+) = (1+r)c'(t) - rq'(t^-), \qquad \textit{if } q(t) = c(t), \text{ and } q'(t) - c'(t) < 0\ ,$$

where $q'(t^+)$ and $q'(t^-)$ are the post- and pre-impact velocities respectively, $c'(t)$ is the projection of the cam velocity vector at the contact point along the direction of the free movement of the follower, and $r \in [0, 1]$ is the coefficient of restitution used to model from plastic to elastic impacts.

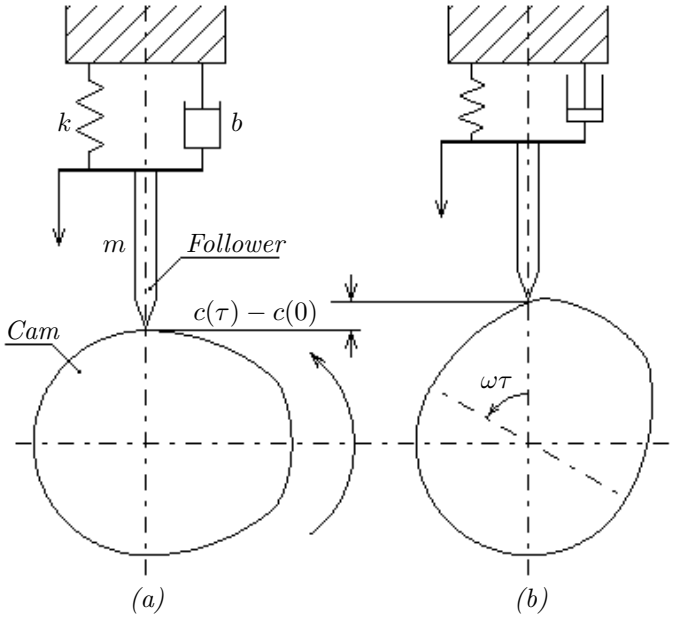

Figure 4.2: Cam-Follower schematics. *(a)* t=0. *(b)* t=τ.

An essential ingredient of the model is the choice of the cam profile, $c(t)$. The cam is assumed to be rotating at a constant angular velocity ω and can be interpreted as the "control action" acting on the follower state as suggested in [57]. Therefore, $c(t)$ is carefully selected in applications as a trade off between several optimality criteria dependent upon the specific device being considered and the unavoidable physical constraints present on the system.

Typically, this is a result of a design process where the cam profile is selected by using some interpolation technique as splines, and can contain several degrees of discontinuity. For example, the cam for a single overhead camshaft valve train is designed by using quadratic splines and, as a consequence, discontinuities are present in its acceleration. In general, it is not uncommon in applications, to find cam geometries characterized by continuous cam positions and velocities but a discontinuous second-derivative [57].

In what follows, we assume the cam profile to be characterized by a discontinuous second derivative as shown in Fig. 4.3. A detailed observation of Fig. 4.3(b), will reveal the nonsmooth nature of the cam profile. Points labelled as *a, b, c, d, e* and *f*, on the lift function $c(t)$, have continuous first derivative (velocity) $c'(t)$ and presents jumps in the second derivative (acceleration) $c''(t)$. This particular shape is a result of a geometrical based cam design, since the profile is constructed as a concatenation of different pieces of circumferences.

The case of a smooth cam profile with continuous first and second-order derivatives is also of interest in applications and was studied experimentally in [4].

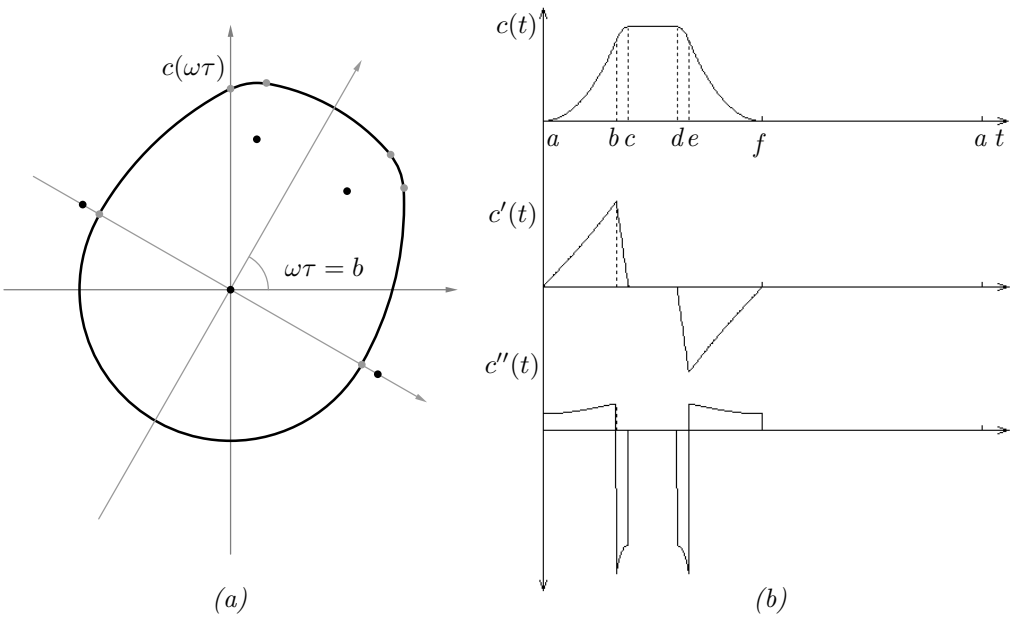

Figure 4.3: (a) Cam profile. (b) Constraint position $c(t)$, velocity $c'(t)$ and acceleration $c''(t)$.

4.2 Simulation and numerical bifurcation analysis

In Sec. 3.2, we have presented technical issues on the simulation of impacting systems. Here, we are interested on the qualitative changes in the dynamics, induce by the nonsmooth nature of the cam profile.

Using specialized routines, we are able to simulate the model represented by (3.37). Given some specific parameter values for the system for $\omega < 114$ rpm, the follower is always attached to the cam due to the force provided by the preloaded spring. For higher values of ω, the asymptotic solution will present impacts. A typical periodic evolution with impacts is shown in Fig. 4.4(a), when $\omega = 183$ rpm. We observe that the follower and the cam are in contact with zero relative velocity (*sticking*) for part of the orbit, and then detach giving rise to impacting behavior. As shown in Fig.4.4(b)-(c) a careful look to the system evolution shows that a *chattering sequence*.

It is then possible to get a global picture of the qualitative behavior of asymptotic solutions with the construction of a bifurcation diagram. We have found that the system exhibit an intricate behavior including the sudden transition to chaos under variation of the cam rotational speed, ω . In Fig. 4.5(a), we present an impact bifurcation diagram for $\omega \in [115, 200]$ *rpm*, where the phase of every impact ϕ_i (rad), is plotted against ω. Instead, in Fig. 4.5*(b)* we present a stroboscopic bifurcation diagram for $\omega \in [115, 200]$ *rpm*. In this case we plot the relative position between the cam and the follower $q(t)$, sampled stroboscopically point Π_s. Finally, in Fig. 4.5(c) we present the time evolution of the follower position $q(t)$ and cam position $c(t)$ for $\omega = 175$ *rpm*. Black dots correlate different representations of the same state in Figs. 4.5(a), 4.5(b) and 4.5(c).

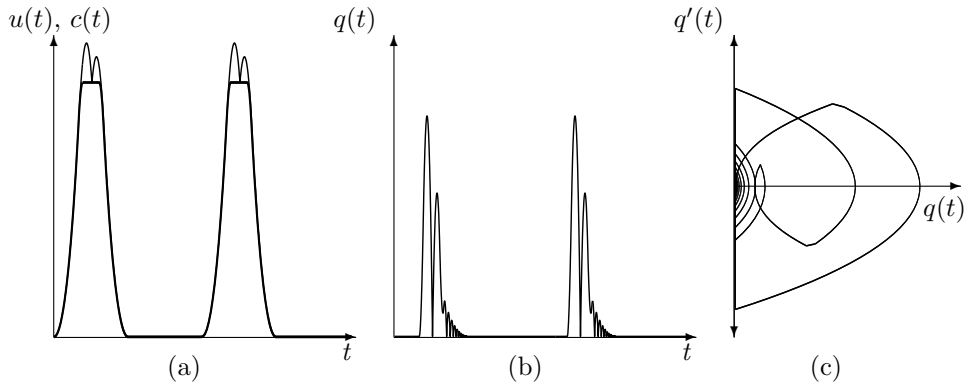

Figure 4.4: Time simulation at $\omega = 183$ *rpm*. (a) Follower position, $u(t)$ (Light); Cam position, $c(t)$ (Dark). (b) Relative position, $q(t)$. (c) Phase space, $q(t)$ *Vs.* $q'(t)$.

4.2.1 Observed dynamics

In order to have a better understanding of the dynamical behavior of the cam–follower device, we present in Fig. 4.6, impact and stroboscopic bifurcation diagrams for a wider range of the cam rotational speed; this is for $\omega \in [114, 850]$.

For each value of the cam rotational speed ω measured in **rpm**, a fixed initial condition (zero relative position and velocity), is simulated for a sufficiently long time to ensure that transients have died out. Then we plot data belonging to the last 60 periods. Now we briefly summarize some of the most striking behavior.

We clearly see the onset of complicated dynamics leading to the sudden formations of seemingly aperiodic solutions and chaos. Before 114 *rpm* the asymptotic dynamic does not include impact because the cam and the follower are always in contact thanks to the restitution force provided by the preloaded spring. After 114 *rpm* a set of period one chattering sequences are generated. For higher values of cam velocity in region $\omega \in [114, 200]$ *rpm* we can observe that the location of the accumulation point varies as function of the cam speed as well as the derivatives of several order. These solutions characterized by the presence of periodic chattering sequences undergo transitions whenever their accumulation point hits the boundary where the cam velocity is non differentiable. This causes transitions to periodic solutions characterized by different impact sequences.

On the other end of the periodic chattering solutions, around 198 *rpm*, we also observe the destruction of the period one orbit. The structural change in the solution involves the crossing of the accumulation point to the next forcing period. For our parameter values, this implies the generation of a set of period two orbits as a route to chaos.

Further on in the parameter space, for $\omega \in [357.5, 361.5]$ rpm, we observe the sudden transition from a chaotic attractor to a 3T-periodic solution with eight impacts. As we will see later on, a stable 1T-periodic orbit with two impacts in each period coexists in the same region. Moreover, there is a particular nonsmooth transition due to a border-collision of one chaotic attractor with the boundary where the cam profile loses its differentiability, implying the jump of the chaotic attractor to a larger one. Next, we will present in detail qualitative changes in the solution induced by the non smooth nature of the cam profile.

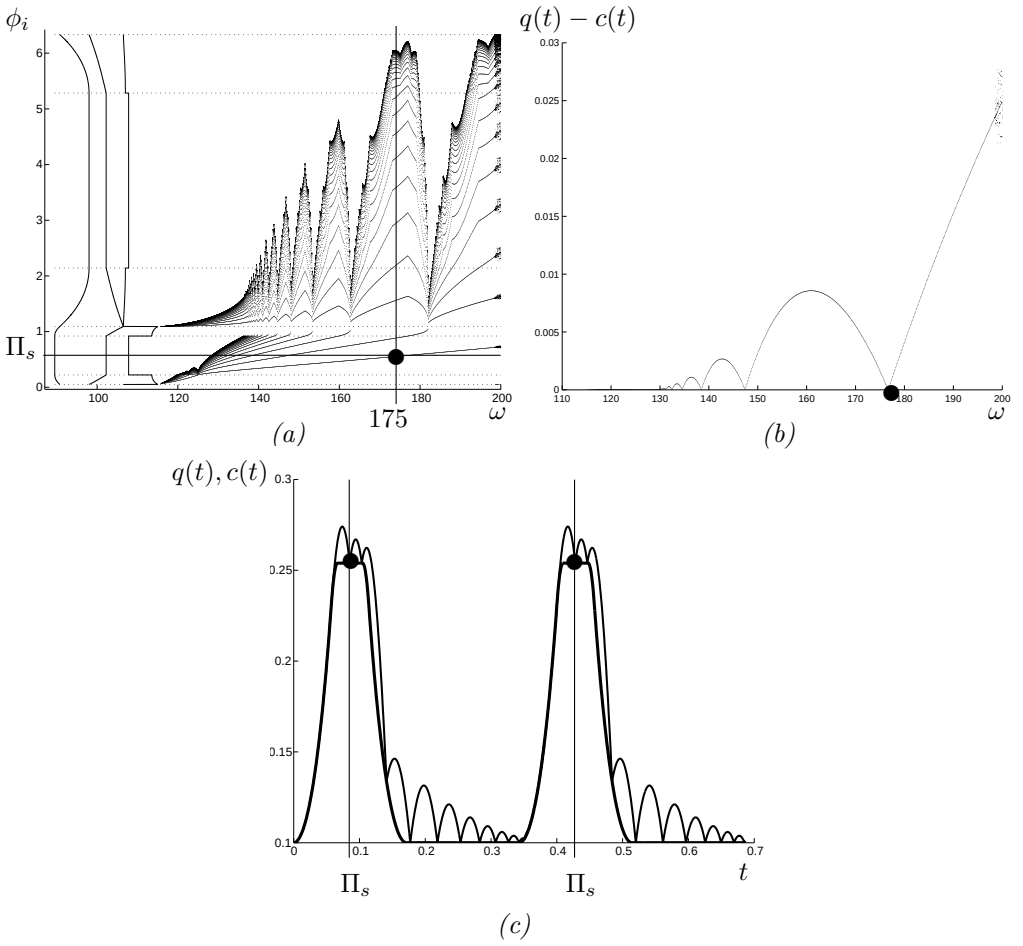

Figure 4.5: *(a)* Impact bifurcation diagram for $[115, 200]$ *rpm*. The phase of an impact ϕ_i (rad), is plotted against ω. *(b)* Stroboscopic bifurcation diagram for $[115, 200]$ *rpm*. Relative position sampled at the stroboscopic point Π_s, between the cam and the follower $q(t) - c(t)$, is plotted against *omega*. *(c)* Time evolution of the follower position $q(t)$ and cam position $c(t)$ for $\omega = 175$ *rpm*. Black dots correlate different representations of the same state in (a), (b) and (c).

4.3 Chattering

In general, starting from low values of ω the system exhibits solutions characterized by permanent contact between the cam and the follower. As ω increases the follower is observed to detach from the cam during its evolution and then to impact with it. Chattering can be associated with an intricate bifurcation structure. In Fig. 4.5(a), the location of the impacts in the cam surface is depicted for each value of ω, characterizing the follower asymptotic solution. We see that following detachment at about 114 rpm, the follower immediately exhibits multi-impacting behavior and chattering (characterized by the accumulation of the impact lines in the diagram onto the darker areas corresponding to the chattering accumulation points). An interesting phenomenon is the

appearance of resonant peaks associated to impact lines crossing the boundaries where the cam acceleration profile is discontinuous (represented by dotted lines in the figure).

This phenomenon can be classified as due to a *corner-impact bifurcation* CIB, a type of discontinuity-induced bifurcation which will be later studied in Chapter 5. Namely, at certain values of ω, one of the impacts characterizing the follower motion occurs at a point on the cam profile where the acceleration is discontinuous. We shall seek to investigate analytically this phenomenon and classify the behavior following the corner-impact event in the cam-follower system of interest.

4.3.1 First detachment

As mentioned before, in the nominal operating regime, there is a permanent contact between the cam and the follower. Therefore a problem of relevance in application is to assess the onset of complex dynamics due to the detachment between the cam and the follower. It is known that this is an undesirable behavior and it is essential to understand the nature of this phenomenon.

Let us define

$$H(x) := q(t) - c(t),$$

$$v(x) := q'(t) - c'(t),$$

$$a(x) := q''(t) - c''(t),$$

where x is the state vector of the follower (position, velocity and time), $H(x)$, $v(x)$ and $a(x)$ are relative position, velocity and acceleration respectively.

Notice that if the follower device is in contact with the cam they will continue in sticking motion if the relative velocity $v(x)$ is zero and relative acceleration $a(x)$ is negative. Therefore the set of detachment points is given by:

$$D = \{x : H(x) = 0, v(x) = 0 \text{ and } a(x) \geq 0\},$$

where conditions on $H(x)$ and $v(x)$ are always satisfied if sticking solution is assumed. Instead, $a(x)$ depends on the system parameters as follows

$$a(x) = -\omega_s^2 \cdot q(t) - c''(t),$$

where ω_s is a positive constant dependant on the system parameters. This implies that the condition for the first detachment after increasing the cam rotational speed is given by

$$c''(t) \leq -w_s^2 \cdot c(t). \tag{4.1}$$

In general, (4.1) can be numerically solved to get the value of ω at which detachment occurs. For our particular example we can go even further since $c(t) > 0$, and $w_s > 0$, then the only way to achieve the detachment condition is $c''(t) < 0$. From Fig. 4.3(b), it can be observed that time instants labelled as 'b' and 'e' will produce the first detachment on monotonous increasing of the cam rotational speed. After solving 4.1, we obtain $\omega = 114.979$ rpm. If we continue increasing the cam rotational speed the detachment point in time instant 'e', starts moving towards the point in time instant 'd', till reaching it at $\omega = 134.873$) rpm.

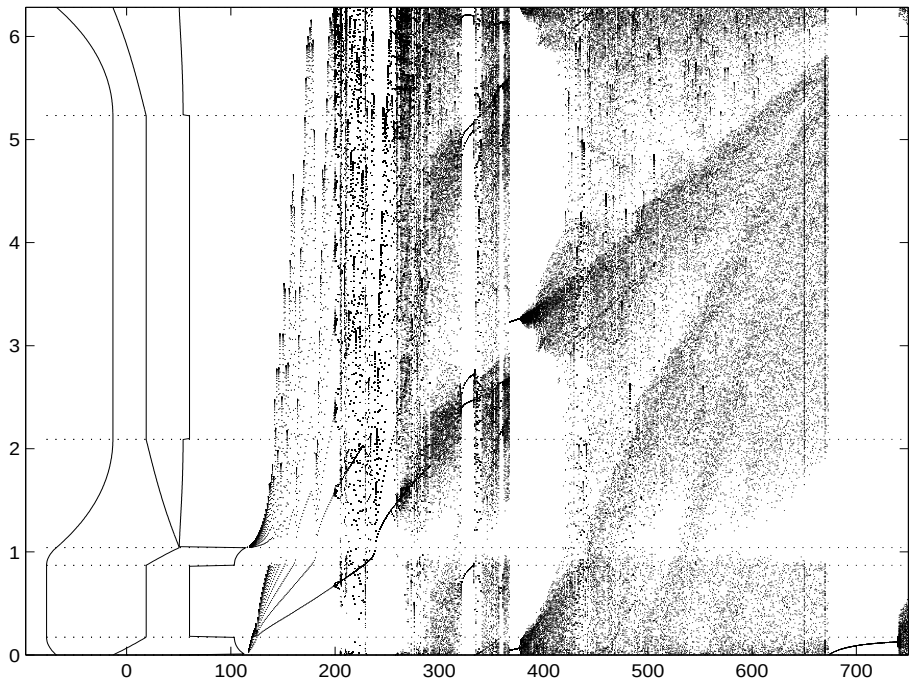

(a)

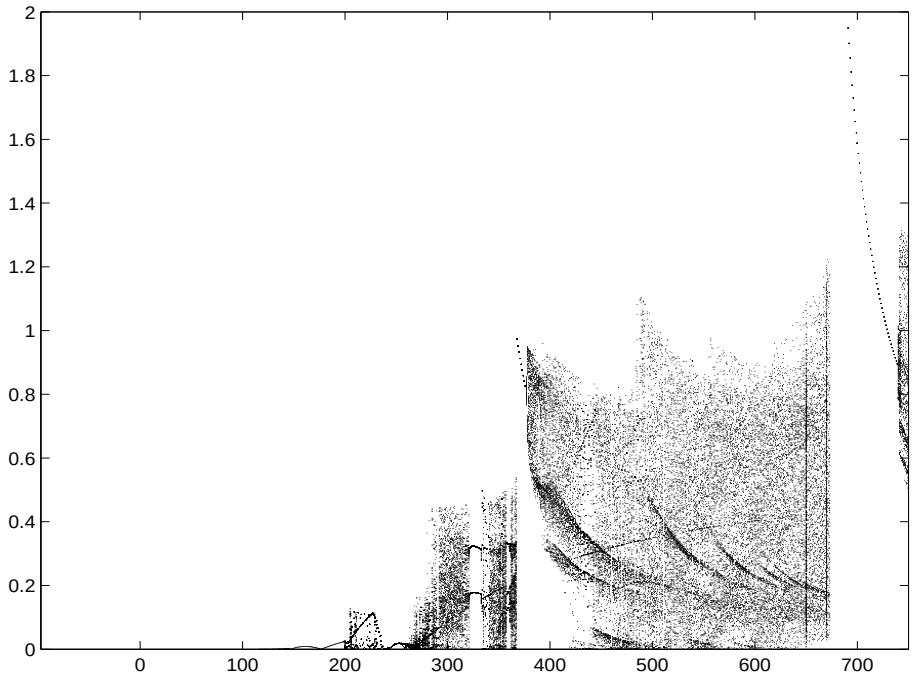

(b)

Figure 4.6: Observed dynamics for $\omega \in [114, 850]$. (a) Impact bifurcation diagram. (b) Stroboscopic bifurcation diagram.

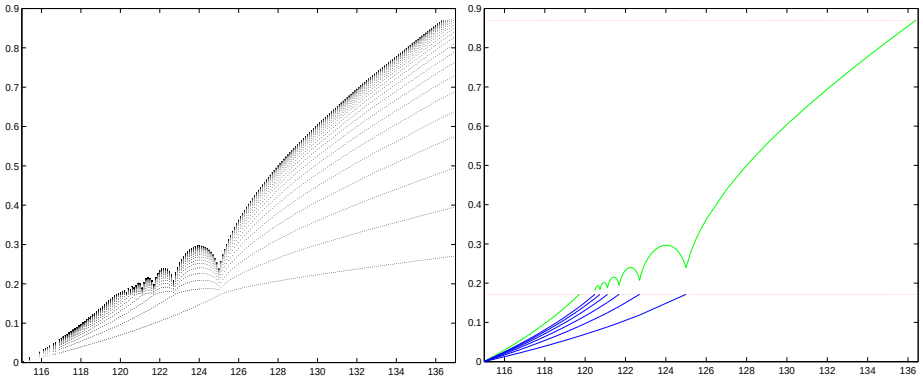

Figure 4.7: Zoom in of the first chattering part. (a) Impact bifurcation diagram. (b) Numerical computation of accumulation points.

4.3.2 Bifurcations involving accumulation points

As can be seen in Fig. 4.7(a), once the detachment between the cam and the follower occurs (*i.e* $\omega = 114.979$ rpm), the asymptotic solution includes two chattering sequences. The first qualitative change will occur when the accumulation point of the chattering sequence (the one associated to the detachment at instant '*b*' in 4.3(b)), reaches the discontinuity point at instant '*c*'. As mentioned in Sec. 3.2.1, we can use the formulation presented in [55], to numerically estimate the accumulation point of a chattering sequence. If $H(x) = 0$, $v(x) < 0$ and small enough, and $a(x) < 0$, the first order approximation is given by

$$t_{acc} = \frac{1}{1-r}\Big(\frac{2}{a(x)}r\Big)v(x). \tag{4.2}$$

Therefore, we can calculate the rotation speed at which the accumulation point exactly reaches the instant time c, at $\omega = 119.72\ rpm$. In Fig. 4.7(b) we present the numerical estimation of the accumulation point chattering sequence. Here we can observe some resonances or "bubbles" in the bifurcation diagram. Such "bubbles" occur when one of the points belonging to the chattering sequence, impacts at instant labelled as '*c*', this is in the point with a discontinuity in the acceleration of the cam. Then the "bubble" amplitude increases at a maximum value, to finish when another impact belonging to the chattering sequence hits the discontinuity point. We have also computed parameter values at the most significant impact crossing, this is $\omega = 120.7356$ rpm, $\omega = 121.107$ rpm, $\omega = 121.686$ rpm, $\omega = 122.699$ rpm and $\omega = 124.998$ rpm. For $\omega > 124.998$ rpm the first impact after detachment occurs later than time instant '*c*', where the cam velocity and acceleration is zero. At $\omega = 136.38$ rpm, the accumulation point of the first chattering sequence reach time instant '*d*', producing a qualitative change in the asymptotic solution, such that there is one chattering sequence instead of two.

Period doubling and sudden transition to chaos As we can see in Fig. 4.8, around $\omega = 198$ rpm, we observe the destruction of the period one chattering sequence. The structural change in the solution is due to the crossing of the accumulation point to the next forcing period.

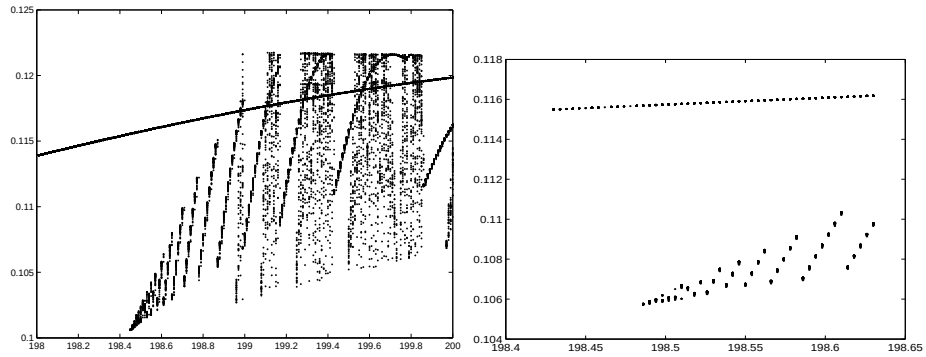

(a) *(b)*

Figure 4.8: Bifurcations involving accumulation points. (a) Stroboscopic bifurcation diagram in range $\omega \in [198, 200]$ rpm. (b) Zoom of the stroboscopic bifurcation diagram.

In Figs. 4.8(a)(b), we show the time evolution of the system before and after the crossing event. A period one orbit is shown in Fig. 4.8(a) at $\omega = 198.4$ rpm. As we can observe in Fig. 4.8(a) the chattering sequence accumulates before crossing the next forcing period. Then, for higher values of ω, the accumulation point is found at the beginning of the next forcing period. For our parameter values, this implies the generation of a set of period two orbits as a route to chaos. In Figs. 4.8(a)(b) a stroboscopic bifurcation diagram is presented.

4.4 Coexistence of periodic orbits

Now we move our attention to other interesting regions in the bifurcation diagram presented in Fig. 4.6. For $\omega \in [358, 360]$ rpm we have found evidence of coexisting solutions. In Fig. 4.9, we present the evolution of two different solutions in the same range of parameter. In particular Figs. 4.9(a)(b) (impact and stroboscopic bifurcation diagram), show a standard period doubling cascade as a route to chaos. We can also observe that at $\omega = 358.5$ rpm, we have a Period-3 solution, with 8 impacts per period (*i.e.* P(3,8)). On the other hand, in Figs. 4.9(c)(d) (impact and stroboscopic bifurcation diagram), we observe that at the same parameter value, $\omega = 358.5$ rpm, there is a Period-1 solution with 2 impacts per period ((*i.e.* $\mathcal{O}(1, 2)$)). Notice that in both cases, decreasing the parameter values causes a sudden transition to chaos in what seems to be a corner impact bifurcation. In the next chapter we will study this particular phenomenon.

A detail of the time and state space evolution for the two coexisting solutions at $\omega = 360$ rpm is presented in Fig. 4.10. In Figs. 4.10(a)(b), we show the evolution of a $\mathcal{O}(6, 16)$ orbit right after the first period doubling. At the same parameter value, we have a coexistent $\mathcal{O}(1, 2)$ solution. (see Figs. 4.10(c)(d)).

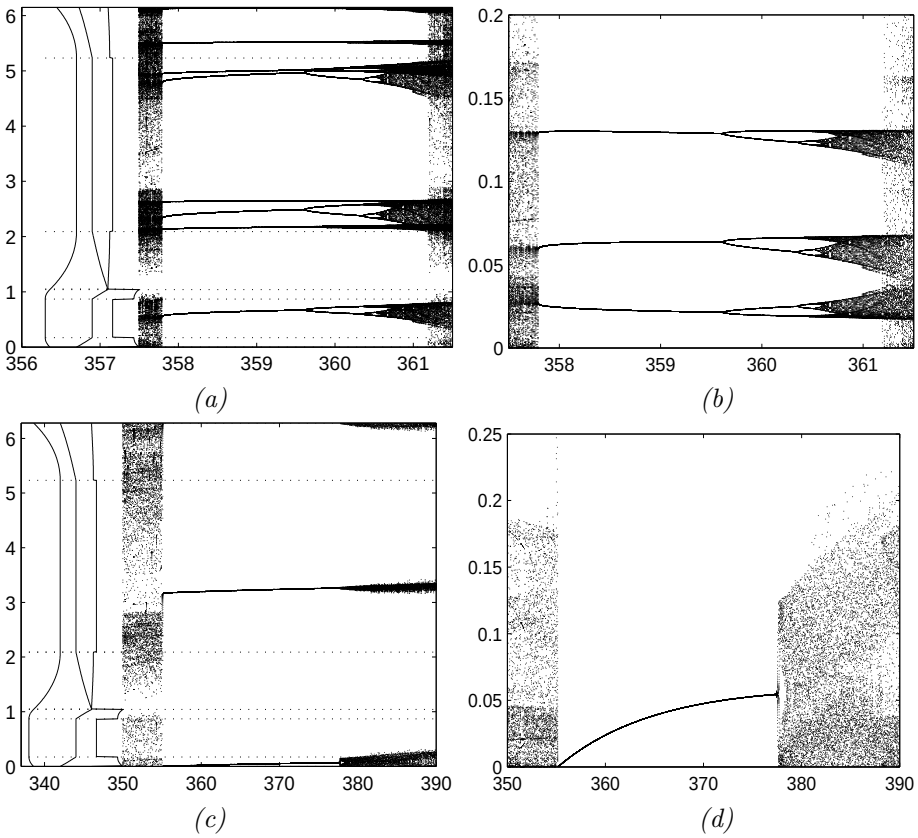

Figure 4.9: Coexistent solutions (a) Impact Bifurcation diagram for cam velocity $\omega \in [357.5, 361.5]$ rpm. (b) Stroboscopic bifurcation diagram for cam velocity $\omega \in [357.5, 361.5]$ rpm, sampling the states at $\Pi_s = 0$. (c) Impact Bifurcation diagram for cam velocity $\omega \in [660, 760]$ rpm. (d) Stroboscopic bifurcation diagram for cam velocity $\omega \in [670, 750]$ rpm, sampling the states at $\Pi_s = 0$.

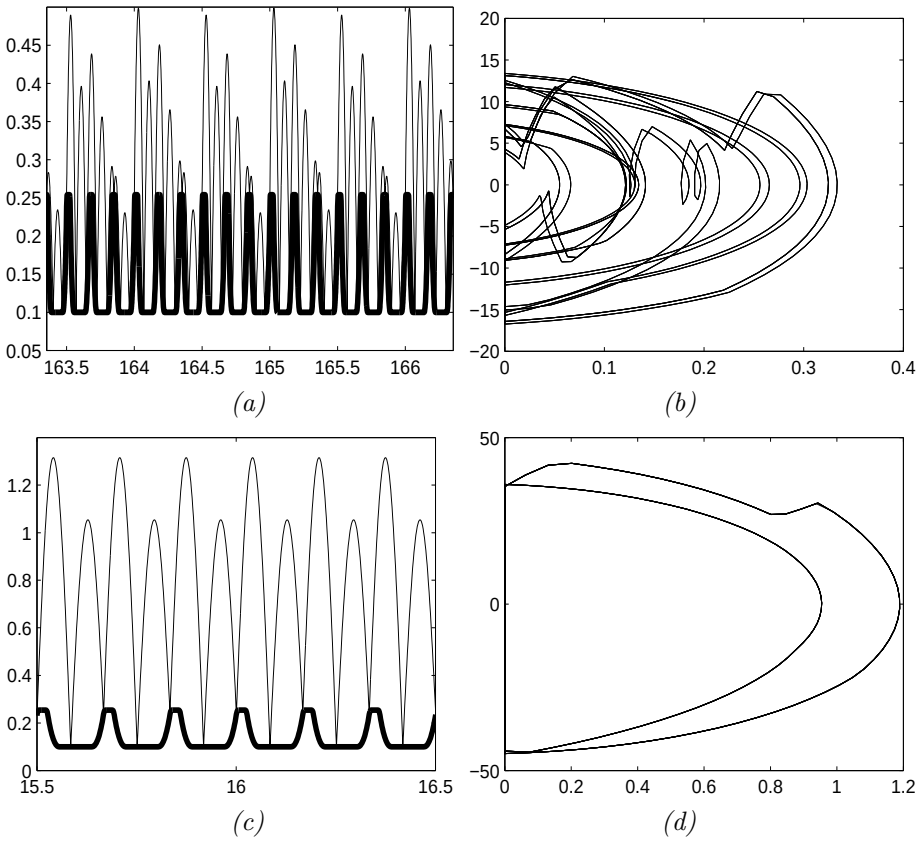

Figure 4.10: Coexistence of periodic solutions for $\omega = 360$ rpm.(a)(c)Time evolution. (b)(d) State space evolution

4.4.1 Domain of attraction

The main idea is to characterize the phase portrait of a Poicaré map associated to the system when there is coexistence of solutions. We have obtained the domain of attraction using a *cell–mapping* method. This technique reduces the amount of computational work needed to get a reasonably accurate picture of basins of attraction (see [77] for further details on the method). Fig. 4.11 shows the different basins of attraction of coexisting solutions for $\omega = 358.5$ rpm. The initial conditions have been taken in the range $x \in [0.1, 1.6]$ and $q' \in [-60, 60]$ considering 10^6 (1000×1000) cells uniformly distributed.

As can be observed there are three coexisting solutions, two stables and one unstable. One of the stable solutions is period 3 while the other one is period 1. The light region corresponds to all initial conditions in the domain of attraction of the period 3 solutions; while the dark region is the basin of the other stable solution. The basins of attraction are separated by the stable manifold of the saddle-node solution.

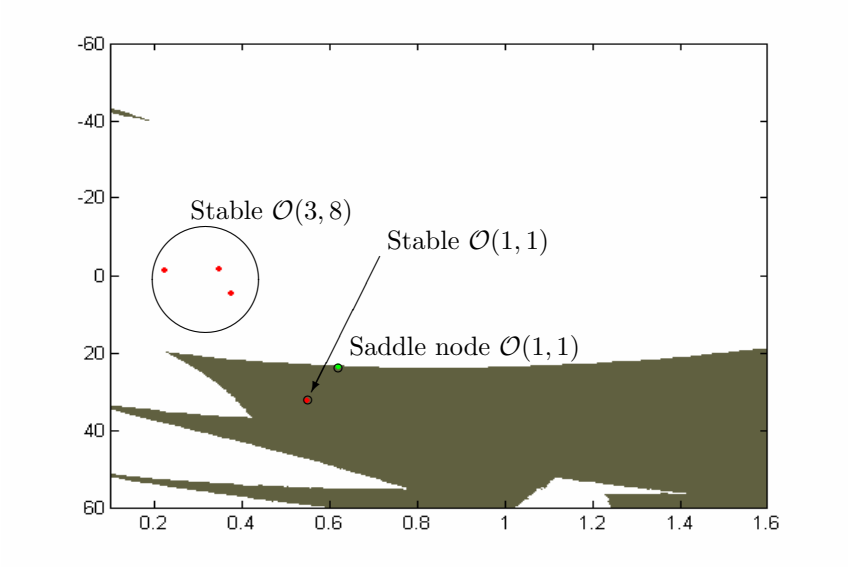

Figure 4.11: Domain of attraction $\omega = 358.5$ rpm.

4.4.2 Smooth and nonsmooth bifurcations of a $\mathcal{O}(1,1)$ Orbit

Now we are interested in the study, of the periodic orbit $\mathcal{O}(1,1)$ in Fig. 4.12(a). This is the bifurcation diagram for $\omega \in [660, 760]$ rpm, where a stable $\mathcal{O}(1;1)$ bifurcates into a $\mathcal{O}(2;2)$ (*i.e.* a period doubling) when the parameter is increased at about $\omega \approx 739$ rpm (see Fig. 4.12(b) for a zoom in). It is also observed that the $\mathcal{O}(1,1)$ orbit vanishes at about $\omega \approx 680$ rpm, due to a corner impact bifurcation as we will show in Chapter 5. The same phenomenon occurs to the $\mathcal{O}(2,2)$ orbit for $\omega \approx 739.378$ rpm, where one of the impacts belonging to the orbit hits a *corner* in the cam lift. Further on in the parameter space at $\omega \approx 740.2$ rpm a chaotic attractor collide again with a discontinuities.

Computing the First Period-doubling of a $\mathcal{O}(1;1)$ Orbit

Flip and saddle-node bifurcations in Fig. 4.12, can be analytically predicted studying the spectrum the Jacobian matrix of the associated Poincaré map (see Sec. 3.4.2 for details). In Fig. 4.13 we show the evolution of the characteristic multipliers of the map $P_x(1;1)$ associated to the orbit $\mathcal{O}(1;1)$, for $\omega \in [672, 756]$ rpm. We observe that the characteristic multipliers of $\mathcal{P}_x$ are complex conjugates that move on a circle of radius $r \approx 0.8$, and so the orbit is asymptotically stable. Near $rpm \approx 736$, both characteristic multipliers become real, and one of the characteristic multipliers has norm greater than 1, which implies that the periodic orbit becomes unstable.

We move now to the detailed analysis of the bifurcation scenario depicted in Fig. Fig. 4.12.

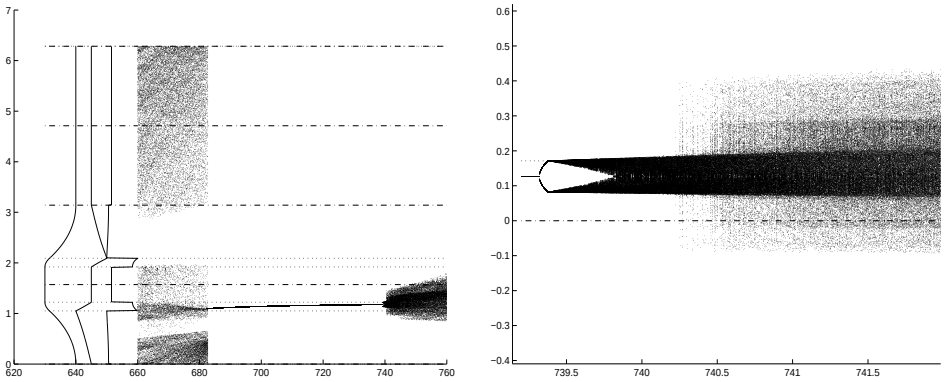

(a) (b)

Figure 4.12: Smooth and nonsmooth bifurcations in periodic orbits.

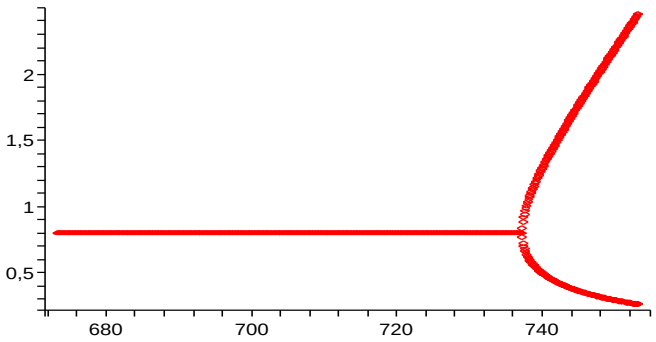

Figure 4.13: Eigenvalues of the stable $\mathcal{O}(1,1)$.

Chapter 5

DIBs in the cam–follower system

Contents

In this chapter we will present a new kind of DIB for impacting systems, that we call *Corner Impact Bifurcation*. We perform a complete analysis for a periodic orbit with impacts in the cam–follower system. This particular bifurcation scenario, exemplifies the use of *Discontinuity Maps* and the theory of *border collision* bifurcations in PWS Maps, to qualitatively characterize the interaction of impacting orbits with a discontinuity boundary. The first reference we are aware of reporting numerical evidence of DIBs in a mechanical system with impacts was published by Shaw and Holmes [67], where authors show a complex sequence of transitions due to discontinuities in an driven impact oscillator. Later on, Nordmark *et al.* [51] [52] [26] [53], have presented an extensive work on the analysis of grazing bifurcation, which explains a wide range of non-smooth bifurcation phenomena that appears in impacting systems. For the sake of simplicity, we focus on region the of the system bifurcation diagram depicted in Fig. 5.1(a). Here, as mentioned in the previous chapter, a one-periodic solution characterized by one impact per period exhibits sudden transitions to chaos as ω is decreased below 673.234445 rpm. A close look at the impact bifurcation diagram in Fig. 5.1(a) and in the stroboscopic bifurcation diagram Fig. 5.1(b) shows that such transitions occur precisely when the impact characterizing the solution crosses the cam discontinuity boundaries (the dotted lines in Fig. 5.1(a)). Specifically, the sudden transition to chaos is due to the corner-impact bifurcation of the periodic solution depicted in Fig. 5.1(c). Past the corner-impact bifurcation point the system exhibits chaotic behavior (see for example the trajectory reported in Fig. 5.1(d) for $\omega \approx 670$ rpm).

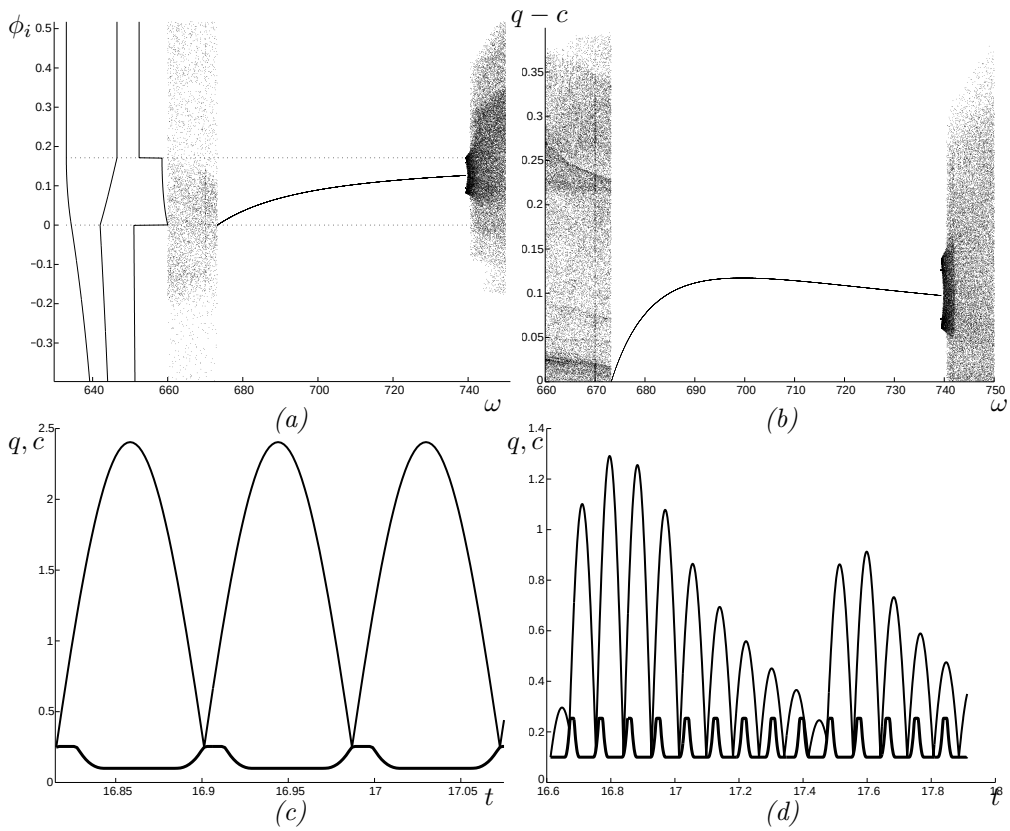

Figure 5.1: *(a)* Impact Bifurcation diagram for $\omega = [660, 750] rpm$.*(b)* Stroboscopic Bifurcation diagram for $\omega = [660, 750] rpm$. *(c)* Bifurcating orbit at the corner impact point at $\omega = 700 rpm$. *(d)* Chaotic evolution for $\omega = 670 rpm$. Dotted lines in *(a)*, represent phases where the cam profile is discontinuous. Vertical curves in panels (a),(c) shows the cam position velocity and acceleration as function of the phase.

5.1 Corner impact bifurcation analysis

The numerical observations reported above indicate that a corner-impact bifurcation is causing the transition to chaos observed in the cam-follower system. Specifically, we are interested in analyzing the occurrence of the corner impact bifurcation depicted in Fig. 5.1(a) when $\omega \approx 673.234445$ rpm. Numerically, we detected that the bifurcating orbit, shown in Fig. 5.1(c) is a one-periodic orbit characterized by one impact per period. As the rotational speed of the cam is decreased, at the bifurcation point, the impact is observed to cross the point on the cam surface where the cam acceleration is discontinuous. To investigate this novel type of discontinuity-induced bifurcation, we will construct analytically the Poincaré map of the system close to the bifurcation point. We will then study the bifurcations of the fixed point corresponding to the periodic solution of interest. A crucial point of the analysis is to assess whether the resulting map is piecewise linear continuous or not. Indeed, only if this is the case, the theory of border-collision bifurcations (see [5, 21]) can be used to classify the possible solutions

branching from the corner-impact bifurcation point [16].

We use the concept of discontinuity mapping (or normal form map) recently introduced in [14], [20], and described in Chapter 3; to construct analytically the Poincaré map associated to the bifurcating orbit of interest. We use the cam-follower system described in Sec 4.1 as a representative example to carry out the analytical derivations.

5.2 Poincaré map derivation

We are interested in the analysis of the period one orbit at the corner-impact bifurcation point. Such orbit is sketched in Fig. 5.2. Then, close to such periodic orbit we define the stroboscopic map P as the mapping from the follower state $x_1 \in \Pi_1$ at a stroboscopic time instant t_1 to the next stroboscopic point $x_2 \in \Pi_2$. Without loss of generality, we assume that $t_n = -\frac{T}{2} + (n-1)T$ for $n = 1, 2, 3, \ldots$, where T is the period of the cam forcing cycle (note that $T = 2\pi/\omega$). Namely, we have:

$$x_2 = P(x_1). \tag{5.1}$$

To construct P we would need to flow forward using the system evolution from x_1 to x_2 for time T taking into account the possible occurrence of impacts and therefore applying Newton's restitution law as required. Alternatively, as shown in [14], it is possible to construct P as the composition of three submappings: (i) an affine transformation $P_{1,T/2}$ from the stroboscopic plane Π_1 at $t_1 = -\frac{T}{2}$ to the plane Π_D going through the corner impact point at $t = 0$; (ii) an appropriate zero-time discontinuity mapping(ZDM) P_D on Π_D accounting for the presence of the discontinuity; and again (iii) an affine transformation $P_{2,T/2}$ from the plane Π_D at $t = 0$ back to the stroboscopic plane Π_2 at $t_2 = \frac{T}{2}$. Specifically, while $P_{1,T/2}$ and $P_{2,T/2}$ are fixed time maps that accounts for the follower evolution away from the cam as if no impact had occurred, the ZDM represents the correction that needs to be made to the system trajectories because of the presence of impacts. Fig. 5.2 represents the global map composition. This means that we can write

$$P = P_{2,T/2} \circ P_D \circ P_{1,T/2}, \tag{5.2}$$

where $P_{1,T/2} : \Pi_1 \mapsto \Pi_D$, will map the state from the initial condition x_1 on the stroboscopic plane Π_1 to a point x_d^- on the discontinuity plane Π_D as if no impacts had occurred. $P_D : \Pi_D \mapsto \Pi_D$ will then map x_d^- to the point x_d^+ appropriately correcting the evolution for the presence of impacts (see Fig. 5.3). Finally $P_{2,T/2} : \Pi_D \mapsto \Pi_2$, will map x_d^+ to a point x_2 back onto the stroboscopic plane Π_2. In so doing, as discussed in [14], [20], the effect of the system discontinuities due to impacts are all taken into account by the ZDM, P_D, which is therefore often termed as the local normal form map in the context of the theory of discontinuity-induced bifurcations [17].

5.2.1 Derivation of $P_{1,T/2}$ and $P_{2,T/2}$

As explained above, the maps $P_{1,T/2}$ and $P_{2,T/2}$ are defined only in terms of the free body dynamics of the follower and the cam rotating period T (depending upon the cam rotational speed ω). Therefore we can solve equations (4.1) to get an analytical expression of the flows generating the mappings of interest.

Specifically, we define

$$x_t = \begin{bmatrix} q(t) + \frac{g}{\omega_0^2} \\ q'(t) \end{bmatrix}, \qquad y_t = \begin{bmatrix} c(t) \\ c'(t) \end{bmatrix}.$$

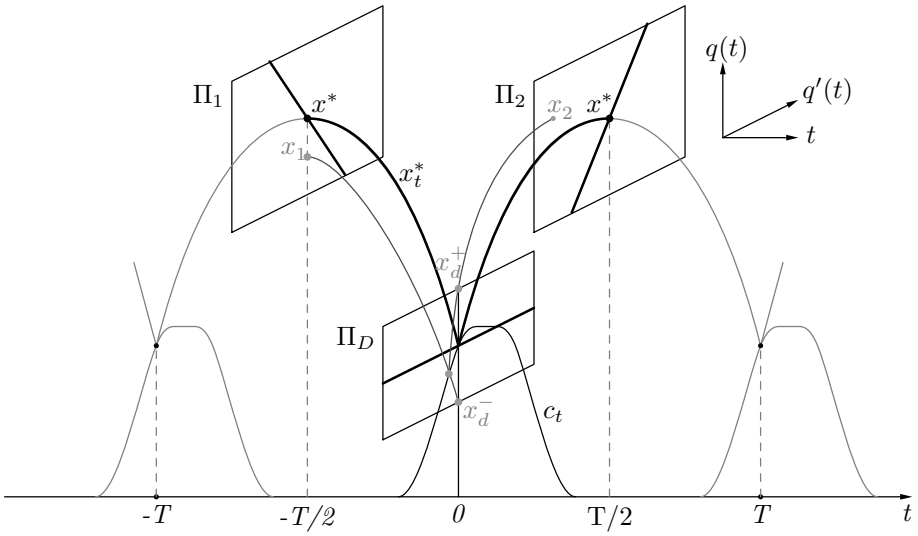

Figure 5.2: Global map composition.

as the state vector for the follower and the cam respectively.

Then, the generalized solution of (4.1) is:

$$\begin{aligned} x_t &= e^{-\zeta t}\left(I\cos(\omega_s t) + A\sin(\omega_s t)\right)x_0 \\ &= \phi_t x_0, \end{aligned} \tag{5.3}$$

where $\zeta = \frac{b}{2m}$, $\omega_0 = \sqrt{\frac{k}{m}}$, $\omega_s = \sqrt{\omega_0^2 - \zeta^2}$, I is the identity matrix, $\phi_t x_0$ represents the system flow for time t starting from the initial condition x_0 and

$$A = \begin{bmatrix} \frac{\zeta}{\omega_s} & \frac{1}{\omega_s} \\ -\frac{\omega_0^2}{\omega_s} & -\frac{\zeta}{\omega_s} \end{bmatrix}.$$

Note that, in general, the system flow operator can be expressed as:

$$\phi_t = \frac{e^{-\zeta t}}{\omega_s}\begin{bmatrix} \omega_s\cos(\omega_s t) + \zeta\sin(\omega_s t) & \sin(\omega_s t) \\ -\omega_0^2\sin(\omega_s t) & \omega_s\cos(\omega_s t) - \zeta\sin(\omega_s t) \end{bmatrix}. \tag{5.4}$$

The submapping $P_{i,T/2}$ can then be easily obtained using (5.3) as:

$$\begin{aligned} P_{i,T/2}(x) &= e^{-\zeta T/2}\left(I\cos(\omega_s T/2) + A\sin(\omega_s T/2)\right)x \\ &:= \phi_{\frac{T}{2}}x. \end{aligned} \tag{5.5}$$

5.2.2 Derivation of P_D

As explained in [20], the ZDM can be obtained by an appropriate composition of backward and forward flows so that the overall time spent following backward and forward is zero. As explained earlier, the ZDM is the correction that maps the point $x_d^- \in \Pi_D$ onto the point $x_d^+ \in \Pi_D$ taking into account the presence of impacts in the trajectory of interest. In what follows we assume that only one impact occurs over one cycle of the periodic orbit of interest as we suppose to be sufficiently close to the bifurcating orbit x_t^*

shown in Fig. 5.2. Fig. 5.3 shows a schematic diagram that describes the construction of the ZDM, close to the corner-impact bifurcations. Without loss of generality we assume that the origin is placed at the Poincaré section Π_D. To derive analytically the mapping $x_d^+ = P_D(x_d^-)$ we need to perform the following steps:

1. Starting from x_d^-, we find the time t_i at which the impact occurs. Namely, t_i is obtained by looking at the difference, $(q(t) - c(t))$, between the follower position and the cam position close to $t = 0$. Given a vector z, we indicate by $[z]_1$ its first component. Then $q(t) = [x_t]_1 - \frac{g}{\omega_0^2}$ and therefore, close to x_d^-, t_i can be obtained as the nearest solution of the equation:

$$H(x_{-t_i}^-, t_i) := \left[x_{-t_i}^- - y_{-t_i}\right]_1 = h \cdot \left[\phi_{-t_i} x_d^- - y_{-t_i}\right] = 0, \tag{5.6}$$

   where $h = [\ 1 \quad 0\ ]$.

   Hence, t_i is implicitly defined by the equation $H(x_{-t_i}^-, t_i) = 0$. Once, t_i is found, the pre-impact state of the system, $x_{-t_i}^-$, can also be obtained as

$$x_{-t_i}^- \quad = \quad \phi_{-t_i} x_d^- . \tag{5.7}$$

   Note that t_i can be either negative or positive according to whether the impact occurs to the left or to the right of $t = 0$.

2. Using the restitution law (4.1), we can then write the post-impact state of the follower $x_{-t_i}^+$ as

$$x_{-t_i}^+ = x_{-t_i}^- + R(x_{-t_i}^- - y_{-t_i}) = \rho(x_{-t_i}^-, y_{-t_i}), \tag{5.8}$$

   where

$$R = \begin{bmatrix} 0 & 0 \\ 0 & -(1+r) \end{bmatrix}.$$

3. Finally, to obtain x_d^+, we flow forward for time t_i starting from the post-impact state $x_{-t_i}^+$ found at the previous step. In so doing, the state of the follower $x_d^+ \in \Pi_D$ can be computed as:

$$x_d^+ = \phi_{t_i} x_{-t_i}^+ . \tag{5.9}$$

Using equations (5.7),(5.8) and (5.9) we can then write explicitly the ZDM as:

$$x_d^+ = \quad P_D(x_d^-) \quad = \left(\mathbf{I} + \phi_{t_i} R \phi_{-t_i}\right) x_d^- - \phi_{t_i} R y_{-t_i}, \tag{5.10}$$

with t_i defined implicitly by the equation (5.6).

5.2.3 Constructing the stroboscopic map

Composing the submappings $P_{1,T/2}$, $P_{2,T/2}$ and P_D given by (5.5) and (5.10), we can then construct the stroboscopic Poincaré map, P, of the system close to the corner-impact bifurcation point from a generic $x_n \in \Pi_n$ to $x_{n+1} \in \Pi_{n+1}$ as:

$$\begin{aligned} x_{n+1} = P(x_n, T) \quad &= \quad P_{2,T/2}(P_D(P_{1,T/2}(x_n))) \\ &= \quad \phi_{\frac{T}{2}} \left(\left(\mathbf{I} + \phi_{t_i} R \phi_{-t_i}\right) \phi_{\frac{T}{2}} x_n - \phi_{t_i} R y_{-t_i} \right), \end{aligned} \tag{5.11}$$

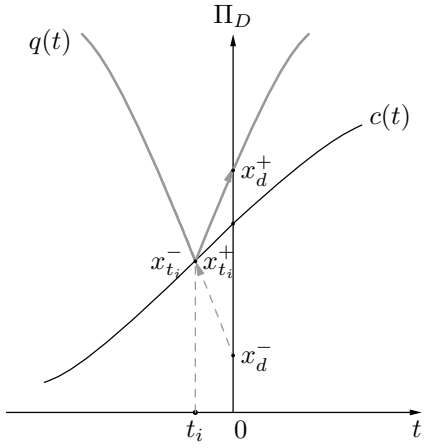

Figure 5.3: ZDM construction.

where t_i is implicitly defined by the equation $H(x_n, t_i) = h \cdot \left(\phi_{\frac{T}{2}-t_i} x_n - y_{-t_i}\right) = 0$.

Note that the fixed point (x^* associated to the periodic solution existing for a fixed value of the cam period $T = T^*$), can be obtained by solving equation (5.11) for $x_{n+1} = x_n = x^*$ i.e.,

$$x^* = -\left[\mathbf{I} - \phi_{T^*} + \phi_{\frac{T^*}{2}} R \phi_{\frac{T^*}{2}}\right]^{-1} \phi_{\frac{T}{2}} R y_0, \tag{5.12}$$

with $t_i^* = 0$.

In what follows we are interested in studying such mapping locally to the corner-impact bifurcation point detected when $\omega = \omega^* = 673.234445$ rpm, corresponding to a period $T^* = 0.08912199969159$ s. The fixed point associated to the bifurcating orbit is $x^* = \left[\begin{array}{cc} 5.09700788184250 & 0 \end{array}\right]'$. These values were detected firstly numerically and then obtained analytically by solving (5.12) through an algebraic manipulation software (For the sake of brevity we leave out the computer algebra here).

5.3 A locally piecewise-linear continuous map

Let δx_n and δT be sufficiently small variations of the state and parameter from the bifurcation point x^*, T^*. We can then linearize the map $x_{n+1} = P(x_n, T)$ in (5.11) about this point as:

$$\delta x_{n+1} = \frac{\partial P(x^*, T^*)}{\partial x_n} \delta x_n + \frac{\partial P(x^*, T^*)}{\partial T} \delta T. \tag{5.13}$$

For the computation of $\frac{\partial P}{\partial x_n}$ it is essential to take into account the implicit dependance of t_i on x_n and T. Hence, using implicit differentiation, we have

$$\frac{\partial P(x_n, T)}{\partial x_n} = \frac{\partial P(x_n)}{\partial x_n} + \frac{\partial P(t_i)}{\partial t_i} \frac{\partial t_i(x_n)}{\partial x_n}. \tag{5.14}$$

Using (5.11), we can then write

$$\frac{\partial P(x_n)}{\partial x_n} = \phi_{\frac{T}{2}}(I + \phi_{-t_i} R \phi_{t_i})\phi_{\frac{T}{2}} \tag{5.15}$$

$$\frac{\partial P(t_i)}{\partial t_i} = \phi_{\frac{T}{2}} \left(\phi'_{t_i} R \phi_{-t_i} - \left(\phi_{t_i} R \phi'_{-t_i}\right) \phi_{\frac{T}{2}} x_n - \phi'_{t_i} R y_{-t_i} + \phi_{t_i} R y'_{-t_i} \right). \tag{5.16}$$

Moreover, using implicit differentiation theorem, from (5.6) we have:

$$\frac{\partial H(x_n, t_i(x_n))}{\partial x_n} = \frac{\partial H(x_n)}{\partial x_n} + \frac{\partial H(t_i)}{\partial t_i} \frac{\partial t_i(x_n)}{\partial x_n} = 0.$$

The above expression can be used to compute the remaining term in (5.14) as:

$$\frac{\partial t_i(x_n)}{\partial x_n} = -\left(\frac{\partial H(t_i)}{\partial t_i}\right)^{-1} \frac{\partial H(x_n)}{\partial x_n}, \tag{5.17}$$

where

$$\frac{\partial H(t_i)}{\partial t_i} = -h \cdot \left(\phi'_{\frac{T}{2}-t_i} x_n - y'_{-t_i}\right),$$

$$\frac{\partial H(x_n)}{\partial x_n} = h \cdot \phi_{\frac{T}{2}-t_i},$$

and $h = \begin{bmatrix} 1 & 0 \end{bmatrix}$.

After substituting (5.15),(5.16) and (5.17) in (5.14) we obtain

$$\left.\frac{\partial P(x_n, T)}{\partial x_n}\right|_{\substack{x_n = x^* \\ T = T^*}} =$$

$$\phi_{\frac{T}{2}^*} \left((I + R) + \left((R\phi'_0 - \phi'_0 R)\, \phi_{\frac{T}{2}^*} x^* + \phi'_0 R y_0 - R y'_0 \right) \frac{h}{h \cdot \left(\phi'_{\frac{T}{2}^*} x^* - y'_0\right)} \right) \phi_{\frac{T}{2}^*}. \tag{5.18}$$

In an analogous way, for the computation of $\frac{\partial P}{\partial T}$, it is essential to take into account the implicit dependance of t_i on x_n and T. Hence, by using implicit differentiation, we have

$$\frac{\partial P(x_n, T)}{\partial T} = \frac{\partial P(T)}{\partial T} + \frac{\partial P(t_i)}{\partial t_i} \frac{\partial t_i(T)}{\partial T}. \tag{5.19}$$

Using (5.11), we can then write

$$\frac{\partial P(T)}{\partial T} =$$

$$\left(\phi'_T + \frac{1}{2} \phi'_{\frac{T}{2}+t_i} R \phi_{\frac{T}{2}-t_i} + \frac{1}{2} \phi_{\frac{T}{2}+t_i} R \phi'_{\frac{T}{2}-t_i} \right) x_n - \frac{1}{2} \phi'_{\frac{T}{2}+t_i} R y_{-t_i} - \phi_{\frac{T}{2}+t_i} R \frac{\partial y_{-t_i, T}}{\partial T}. \tag{5.20}$$

Again, from (5.6) we have:

$$\frac{\partial H(x_n, t_i(x_n))}{\partial T} = \frac{\partial H(T)}{\partial T} + \frac{\partial H(t_i)}{\partial t_i} \frac{\partial t_i(T)}{\partial T} = 0,$$

that can be used to compute the remaining term in (5.19). Namely, we obtain:

$$\frac{\partial t_i(T)}{\partial T} = -\left(\frac{\partial H(t_i)}{\partial t_i}\right)^{-1} \frac{\partial H(T)}{\partial T}, \tag{5.21}$$

where

$$\begin{aligned} \frac{\partial H(t_i)}{\partial t_i} &= -h \cdot \left(\phi'_{\frac{T}{2}-t_i} x_n - y'_{-t_i}\right) \\ \frac{\partial H(T)}{\partial T} &= h \cdot \left(\frac{1}{2}\phi'_{\frac{T}{2}-t_i} x_n - \frac{\partial y_{-t_i,T}}{\partial T}\right) \end{aligned}$$

and

$$\frac{\partial y_{t,T}}{\partial T} = \begin{bmatrix} -\frac{t}{T}c'(t) \\ -\frac{1}{T}c'(t) - \frac{t}{T}c''(t) \end{bmatrix}.$$

Finally, substituting (5.16), (5.20) and (5.21) into (5.19), yields

$$\begin{aligned} \left.\frac{\partial P(x_n,T)}{\partial T}\right|_{\substack{x_n=x^* \\ T=T^*}} = \\ \left(\phi'_{T^*} + \frac{1}{2}\phi'_{\frac{T}{2}^*} R \phi_{\frac{T}{2}^*} + \frac{1}{2}\phi_{\frac{T}{2}^*} R \phi'_{\frac{T}{2}^*}\right) x^* - \frac{1}{2}\phi'_{\frac{T}{2}^*} R y_0 - \phi_{\frac{T^*}{2}} R \frac{\partial y_{0,T^*}}{\partial T} \\ + \phi_{\frac{T}{2}^*} \left(\left(R\phi'_0 - \phi'_0 R\right)\phi_{\frac{T}{2}^*} x^* + \phi'_0 R y_0 - R y'_0\right) \cdot \frac{h \cdot \left(\frac{1}{2}\phi'_{\frac{T}{2}^*} x^* - \frac{\partial y_{0,T^*}}{\partial T}\right)}{h \cdot \left(\phi'_{\frac{T}{2}^*} x^* - y'_0\right)}. \end{aligned} \tag{5.22}$$

We can then compute explicitly these quantities for the cam-follower system of interest. In particular, after some algebraic manipulation, we have:

$$A := \frac{\partial P}{\partial x_n}(x^*, T^*) = \phi_{\frac{T}{2}^*} \begin{bmatrix} -r & 0 \\ -\frac{(1+r)(2\zeta c'_0 + c''_0 + \omega_0^2 q_d^*)}{q_d^{'*} - c'_0} & -r \end{bmatrix} \phi_{\frac{T}{2}^*} \tag{5.23}$$

and

$$\begin{aligned} B := \frac{\partial P}{\partial T}(x^*, T^*) = \frac{1}{2}\phi_{\frac{T}{2}^*} \begin{bmatrix} q_d^* \\ -r q_d^{'*} + (1+r)c'_0 \end{bmatrix} + \frac{1}{2}\phi'_{\frac{T}{2}^*} \begin{bmatrix} q_d^{'*} \\ -r q_d^{''*} - \frac{2(1+r)}{T^*} c'_0 \end{bmatrix} \\ + \frac{1}{2}\phi_{\frac{T}{2}^*} \frac{(1+r) q_d^{'*}}{q_d^{'*} - c'_0} \begin{bmatrix} q_d^{'*} - c'_0 \\ 2\zeta c'_0 + c''_0 + \omega_0^2 q_d^* \end{bmatrix}. \end{aligned} \tag{5.24}$$

Note that both the matrices A and B as defined by (5.23)-(5.24) depend on the value of the second derivative of the cam acceleration c''_0 at the impact point. Therefore the map is actually piecewise-linear locally to the bifurcation point where the cam acceleration is discontinuous, i.e.

$$c''^-_0 := \lim_{t \to 0^-} c''(t) \neq \lim_{t \to 0^-} c''(t) := c''^+_0.$$

Then, the local map can be expressed as:

$$\delta x_{n+1} = \begin{cases} A^- \delta x_n + B^- \delta T, & \text{If } C \cdot \delta x_n + D \cdot \delta T < 0, \\ \\ A^+ \delta x_n + B^+ \delta T, & \text{If } C \cdot \delta x_n + D \cdot \delta T > 0, \end{cases} \tag{5.25}$$

where

$$A^{\pm} = \frac{\partial P^{\pm}}{\partial x}, \quad B^{\pm} = \frac{\partial P^{\pm}}{\partial T},$$

with the index $\pm$ indicating whether the matrices are evaluated with $c_0'' = c_0''^-$ or $c_0'' = c_0''^+$.

We have established that close to the corner-impact bifurcation point, the dynamics of the follower can be studied by means of the local mapping (5.25).

Now, from (5.11), the global Poincaré map is known to be a continuous function of the cam position and velocity through the term y_{-t_i}. Moreover, the map is independent from the cam acceleration. It follows, that the map is continuous at the bifurcation point, *i.e.* we must have that

$$A^- \delta x_n + B^- \delta T = A^+ \delta x_n + B^+ \delta T,$$

when

$$C \delta x_n + D \delta T = 0.$$

Therefore we have

$$C = h \cdot (A^+ - A^-), \quad \text{and} \quad D = h \cdot (B^+ - B^-).$$

Substituting the numerical values of the map parameters for the cam–follower system of interest, we obtain the following analytical estimates of the map matrices:

$$A^- = \begin{bmatrix} 0.82093496821478 & 0.01346530915655 \\ 2.52012201452530 & 0.82093496821478 \end{bmatrix}, \; B^- = \begin{bmatrix} -51.62757990297 \\ -5455.79455977621 \end{bmatrix},$$

$$A^+ = \begin{bmatrix} 0.68571072072040 & -0.07351052377964 \\ 2.30988433707948 & 0.68571072072040 \end{bmatrix}, \; B^+ = \begin{bmatrix} 208.11740649865 \\ -5051.96030903248 \end{bmatrix}$$

and

$$C = [-0.13522424749438 \; -0.08697583293619], \; D = 259.7449864016200.$$

5.3.1 Numerical validation

We will now validate our numerical findings by comparing the map (5.25), which was derived analytically, with the numerical estimates of the mapping obtained by means of simulation and an optimized fitting algorithm close to the bifurcation point.

To derive such an estimate, we use an accurate event-driven numerical algorithm to simulate the cam dynamics over one period starting from a set of M different initial conditions and parameter values. Namely, say $\delta\bar{x}_n$ the vector of M possible perturbations of x^* and $\delta\bar{T}$ the vector of M possible perturbations of T. We then simulate the cam dynamics from each of the perturbed initial conditions and parameter values to obtain the vector $\delta\bar{x}_{n+1} = x^* - x_{n+1}$ after one period. We repeat the set of simulation twice, once with the cam acceleration set to $c_0''^+$ and once with the acceleration set to $c_0''^-$. In so doing, we obtain numerically the vectors

$$\delta\bar{x}^{\pm}_{n+1} = \begin{bmatrix} \delta\bar{x}^1_{n+1} & \dots & \delta\bar{x}^m_{n+1} & \dots & \delta\bar{x}^M_{n+1} \end{bmatrix}.$$

We then use a least-squares fitting algorithm to estimate the matrices $\hat{A}^{\pm}$ and $\hat{B}^{\pm}$ that minimize the error

$$e = \left\| \delta\bar{x}_{n+1}^{\pm} - \left[\begin{array}{c|c} \hat{A}^{\pm} & \hat{B}^{\pm} \end{array} \right] \left[\begin{array}{c} \delta\bar{x}_n \\ \delta\bar{T} \end{array} \right] \right\|^2 .$$

The estimated map matrices found using this numerical strategy are

$$\hat{A}^{-} = \left[\begin{array}{cc} 0.82093497830369 & 0.01346530945739 \\ 2.52012201542191 & 0.82093496286678 \end{array} \right], \hat{B}^{-} = \left[\begin{array}{c} -51.62757113994 \\ -5455.79411324739 \end{array} \right],$$

$$\hat{A}^{+} = \left[\begin{array}{cc} 0.68571065978423 & -0.07351053029558 \\ 2.30988432418263 & 0.68571073479454 \end{array} \right], \hat{B}^{+} = \left[\begin{array}{c} 208.11731732063 \\ -5051.95951604729 \end{array} \right].$$

We notice that these numerical estimates are almost identical (up to at least 5 decimal places) to those obtained analytically earlier in the paper. This validates our analysis and shows the reliability of the analytical derivation used to get a leading order estimate of the Poincaré map close to the bifurcation point under investigation.

5.4 Classification of the discontinuity induced bifurcation scenario

We can now use the locally derived map (analytical or numerical) to classify and explain the bifurcation scenario due to the corner-impact bifurcation detected in the cam-follower system of interest. In particular, the map derived above is a piecewise linear continuous map. As the cam rotational speed is increased, the period T of the forcing provided by the cam varies. Correspondingly, at the corner-impact bifurcation point ($\delta T = 0$), the map fixed point undergoes a border collision. Feigin strategy for border-collision bifurcations can then be used to classify the corner-impact bifurcation scenario [21].

The idea is to start by recasting the map (5.25) into a canonical form following the procedure presented in [19]. Specifically,

1. We eliminate the term depending on δT by considering an appropriate change of coordinates. In particular if we say c_1 and c_2 the coefficients of C, we choose:

$$\begin{aligned} \delta\tilde{x}_n^1 &= \delta x_n^1 + D\frac{\mu}{c_1}, \\ \delta\tilde{x}_n^2 &= \delta x_n^2, \end{aligned}$$

so that the map becomes

$$\delta\tilde{x}_{n+1} = \begin{cases} A^{-}\delta\tilde{x}_n + \tilde{B}\delta T, & \text{If } C \cdot \delta\tilde{x}_n < 0, \\ \\ A^{+}\delta\tilde{x}_n + \tilde{B}\delta T, & \text{If } C \cdot \delta\tilde{x}_n > 0, \end{cases}$$

where

$$\tilde{B} = \left[\begin{array}{c} b_1^{-} - \frac{a_{11}^{-}}{c_1}d \\ b_2^{-} - \frac{a_{21}^{-}}{c_1}d \end{array} \right] = \left[\begin{array}{c} b_1^{+} - \frac{a_{11}^{+}}{c_1}d \\ b_2^{+} - \frac{a_{21}^{+}}{c_1}d \end{array} \right] = \left[\begin{array}{c} 1525.26226128059 \\ -615.02768162765 \end{array} \right],$$

with $a_{ij}^{\pm}$ being the coefficients of $A^{\pm}$.

2. Then, using the strategy presented in [19, 15], we consider the change of coordinates $x = W^{-1}\tilde{x}$ where the matrix W is obtained as $W = T^{-}O^{-}$ with

$$O^{-} = \begin{bmatrix} C \\ CA^{-} \end{bmatrix}, T^{-} = \begin{bmatrix} 1 & 0 \\ d_1^{-} & 1 \end{bmatrix},$$

where d_1^{-} is the linear coefficient of the characteristic polynomial of A^{-} given by $p^{-}(\lambda) = \lambda^2 + d_1^{-}\lambda + d_2^{-}$. Applying such a similarity transformation, the map matrices become:

$$\bar{A}^{-} = \begin{bmatrix} 1.64186993642956 & 1 \\ -0.64 & 0 \end{bmatrix}, \ \bar{A}^{+} = \begin{bmatrix} 1.37142144144080 & 1 \\ -0.64 & 0 \end{bmatrix},$$

and

$$\bar{B} = \begin{bmatrix} 152.75990 \\ 207,79599 \end{bmatrix}, \qquad \bar{C} = \begin{bmatrix} 1 & 0 \end{bmatrix}.$$

As explained in [21, 19], we can now classify the type of bifurcation scenario observed at the bifurcation point under investigation by computing the map eigenvalues on both sides of the boundary. For the case under investigation, we have that: (i) the eigenvalues of A^{-} are $\lambda_1^{-} = 1.0052$ and $\lambda_2^{-} = 0.6367$; (ii) the eigenvalues of A^{+} are $\lambda_{1,2}^{+} = 0.6857 \pm \mathbf{j}0.4120$. Hence, according to Feigin's classification strategy, since the total number of real eigenvalues greater than unity on both sides of the boundary is odd, the bifurcating fixed point will undergo a nonsmooth saddle node bifurcation and ceases to exist [21]. This is in perfect agreement with what observed numerically as shown in Fig. 5.4, where the local bifurcation scenario observed in the map is shown.

Therefore, we can explain the sudden transition to chaos observed in the cam-follower system under investigation as due to the occurrence of a corner-impact bifurcation. Namely, the corner-impact is associated to a nonsmooth-fold scenario causing the disappearance of the stable impacting solution undergoing the bifurcation. This causes trajectories to leave the local neighborhood where they are confined before the bifurcation and converge towards the stable coexisting chaotic attractor when ω is decreased below the corner-impact bifurcation point.

Hence, we can conclude that corner-impact bifurcations in cam–follower systems can indeed lead to dramatic changes of the system qualitative behavior including sudden transitions from periodic solutions to chaos.

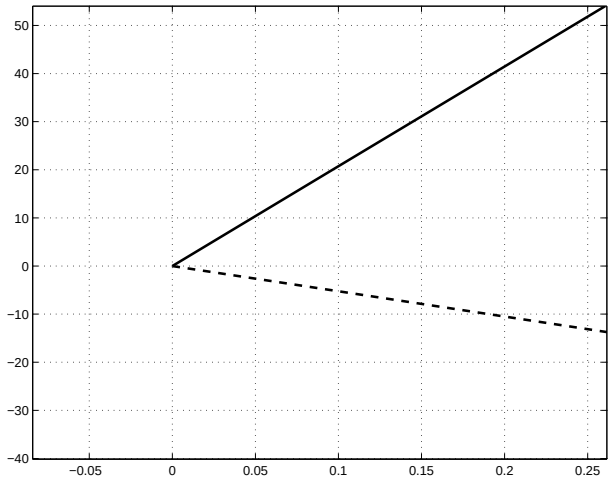

Figure 5.4: Numerical bifurcation diagram of the local map (5.25) with the analytically estimated matrices. The border collision when $\delta T = 0$ corresponds to the corner-impact bifurcation point at $\omega \approx 673.2$ rpm. Note that as predicted a nonsmooth fold scenario is observed with no fixed point existing for $\delta T < 0$ and two coexisting fixed points, one stable, the other unstable for $\delta T > 0$.

Chapter 6

Corner Impact Bifurcation in Generic Impacting Systems

Contents

In this chapter, we present the local and global analysis of impacting orbits near discontinuity points of the impacting manifold, using the concept of discrete maps and the theory of border collision bifurcations presented in Chapter 2. The global map, or *Global Poincaré Map*, can be also derived for impacting systems through the composition of fixed time maps and discontinuity maps. Fixed time maps will describe the system evolution between impacts, while the discontinuity mappings will take care of the impact dynamics. This analytical tool has been already used for the global analysis of impacting systems with smooth differentiable boundaries at hard and soft (grazing) impacts. Here, the analysis is intended to fill a gap, by performing the analysis of impacting orbits where the boundaries in the admissible space are not continuously differentiable (*i.e.* configuration space with corners. See section 6.1 for definition). Finally, we analyze the case of a representative cam–follower system.

6.1 Impacting systems with a corner

We define an *impacting system* over some admissible region $\Omega \in \mathbb{R}^n$ (see Fig. 6.1) as

$$\begin{cases} \dot{x}(t) = F(x(t), \mu) \\ x^+ = R_i(x^-, y_i^-) \quad \text{If impact} \end{cases} \tag{6.1}$$

where $x(t) \in \mathbb{R}^n$ is the state vector, $\mu \in \mathbb{R}^p$ is a parameter vector, $F : \mathbb{R}^n \to \mathbb{R}^n$ is a smooth vector field.

The zero level sets of the smooth functions $H_1(x(t), y_1(t))$ and $H_2(x(t), y_2(t))$ define the boundary set $\partial\Omega$. In particular we choose:

$$H_i(x(t), y_i(t)) := C^T(x(t) - y_i(t)), \quad \text{and} \quad \Sigma_i := \{x : H_i(x(t), y_i(t)) = 0\}, \tag{6.2}$$

with $C^T := \begin{bmatrix} 1 & 0 & \cdots & 0 \end{bmatrix}$ defined such that H_i gives the relative position of the system with the moving constraint Σ_i for $i = \{1, 2\}$. The impact time τ is implicitly defined by the contact condition $H_i(x(\tau), y_i(\tau)) = 0$. The relative velocity is obtained from (6.2) as $H_{i,t}(x(\tau), y_i(\tau)) < 0$.

An impact occurs when the contact condition holds. We also define $y_i^- := y_i(\tau^-) = \lim_{t \to \tau^-} y_i(t)$, from the state vector (position, velocity and parameterized time) of the moving constraint at impact. In (6.1), the impact does not affects the state of the moving constraint which implies $y_i^+ := y_i(\tau^+) = y_i(\tau^-)$, with negative relative velocity. We assume the relative velocity at impact to be strictly negative, since we are not interested in the analysis of soft (grazing) impacts.

The impact map $R_i(\cdot, \cdot) : \partial\Omega \longmapsto \partial\Omega$ describes the correction to the system state $x(t)$ at impact with Σ_i, and is given by

$$R_i(x^-, y_i^-) := x^- - W v_i(x^-, y_i^-), \tag{6.3}$$

where $W := \begin{bmatrix} 0 & (1+r) & \cdots & 0 \end{bmatrix}^T$, is defined such that the impact mapping affects only the velocity component with $0 \leq r \leq 1$, as restitution coefficient; and v_i is the relative velocity of the system referred to the moving constraint Σ_i. We can then write the impact map R_i as

$$\begin{aligned} R_i(x^-, y_i^-) &= x^- - W H_{1,t}(x^-, y_i^-), \\ &= x^- - W(H_{1,x} F(x^-) + H_{1,y} G_i(y_i^-)), \\ &= x^- - W C^T(F(x^-) - G_i(y_i^-)), \qquad (6.4) \\ &= x^- - W C^T(F(\phi(x_0, \tau_i)) - G(\gamma(y_0, \tau_i))). \qquad (6.5) \end{aligned}$$

We label $\phi(x, t)$ the system flow generated by F such that

$$\frac{d\phi(x,t)}{dt} = F(\phi(x,t)), \qquad \phi(x,0) = x. \tag{6.6}$$

Let us assume there is an impact at time $\tau \in \mathbb{R}$, belonging to a zero measure set $\mathcal{T}$ containing all the impact times of an orbit. We denote the state before impact at time τ as $x^- := x(\tau^-) = \lim_{t \to \tau^-} x(t)$, and the state after impact as $x^+ := x(\tau^+) = \lim_{t \to \tau^+} x(t)$.

We focus our analysis on the assumption that, the moving constraint changes configuration at some time instant t_c, between the smooth functions $y_1(t)$ and $y_2(t)$ *i.e.*

$$y(t) = \begin{cases} y_1(t) & \text{If } t \leq t_c, \\ y_2(t) & \text{If } t > t_c. \end{cases} \tag{6.7}$$

Moreover, without loss of generality, we suppose that $y_i(t)$ is given by the differential equation

$$\dot{y}_i(t) = G_i(y_i(t), t),$$

and we define $\gamma_i(y,t)$ as the system flow generated by G_i such that

$$\frac{d\gamma_i(y,t)}{dt} = G_i(\gamma_i(y,t)), \qquad \gamma_i(y,0) = y. \tag{6.8}$$

We also define $y_i^- := y_i(\tau^-) = \lim_{t\to\tau^-} y_i(t)$, as the state vector of the moving constraint at impact. Note that, the impact does not affect the state of the moving constraint which implies $y_i^+ := y_i(\tau^+) = y_i^-$.

We assume the impact map to be invertible such that

$$(R_i^{-1} \circ R_i)(x^-, y_i^-) = R_i^{-1}(R_i(x^-, y_i^-), y_i^-) = x^-,$$

and

$$(R_i \circ R_i^{-1})(x^+, y_i^+) = R_i(R_i^{-1}(x^+, y_i^+), y_i^+) = x^+,$$

with the inverse given by

$$R_i^{-1}(x^+, y_i^+) \quad := \quad x^+ - \frac{1}{r} W C^T (F(x^+) - G_i(y_i^+)). \tag{6.9}$$

An impacting trajectory can be described by appropriately composing the system flow with the impact rule. For example, assume that a trajectory starting from $x(0) = x_0$, impacts with Σ_i at time τ_i. Then the dynamics for $t > \tau_i$ will be given by

$$x(t) = \phi(R_i(\phi(x_0, \tau_i), y_i(\tau_i))), t - \tau_i)$$

Definition 1: $y_c \in \partial\Omega$ is a corner of degree k, if $y_c \in \Sigma_1 \cap \Sigma_2$, and $\frac{\partial^k H_1}{\partial y^k} \neq \frac{\partial^k H_2}{\partial y^k}$.

According to the definition of the admissible space given in (6.7), where we assume non-smooth dynamics of the moving constraint; we will find a corner at every point that is not continuously differentiable. At corners of degree 1, the normal and tangential directions of $\partial\Omega$ are not well-defined. Besides constraints (as for example kinetic energy loss, or post impact velocities into feasible motion domain), it is necessary to impose impact rules to render the problem solvable (i.e. find a unique set of postimpact velocities). For references on the modelling of the impact dynamics with generic corners (singularities) see [7]. In order to model the system studied in this chapter, it is enough to establish that for corners of degree 2 or higher, the normal and tangential directions of $\partial\Omega$ are well-defined everywhere, and the impact map can be solved by associating some restitution coefficients where needed.

For the stability analysis instead, using the classification strategy presented firstly by Feigin [24], we will show the analysis of discontinuity-induced bifurcations at least for corners of degree 2.

Definition 2: Given the impacting system in (6.1), we say that a trajectory $x(t)$ undergoes a corner impact bifurcation of degree k, for $\mu = \mu_c$; if $\exists\ \tau_c < +\infty$ such that $[x(\tau_c)]_1 = [y_c]_1$ and $y_c \in \partial\Omega$ is a corner of degree k.

Fig. 6.1 presents several examples of configuration spaces with a corner set. In all cases the position is plotted versus parameterized time, for the moving constraint, defined by two smooth manifolds Σ_1 and Σ_2.

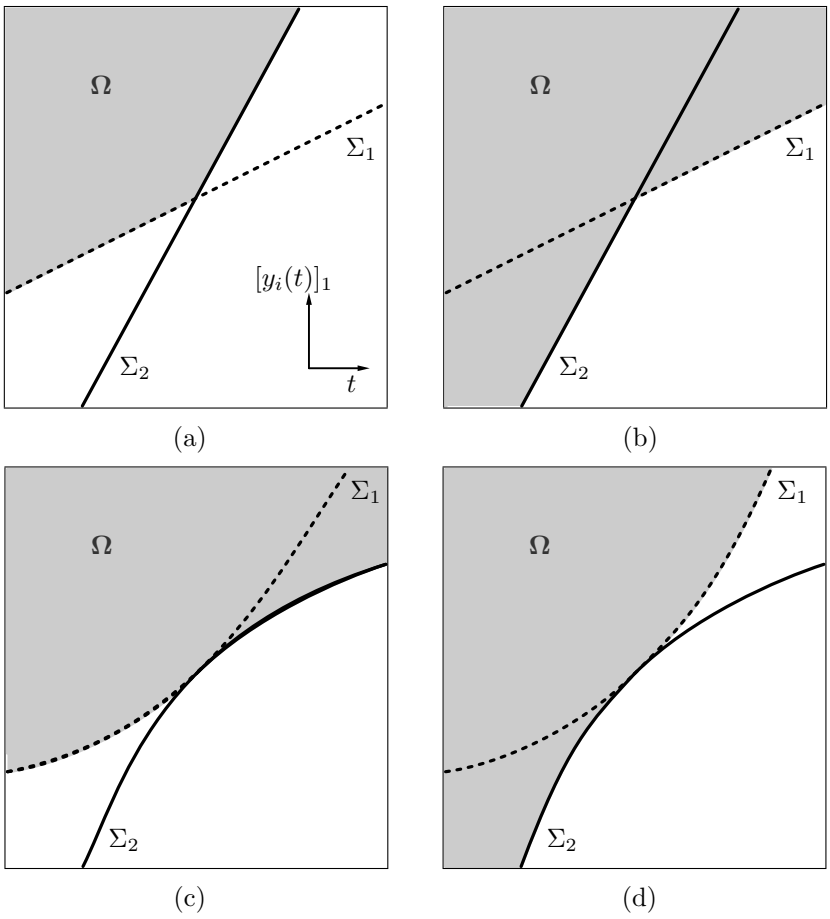

Figure 6.1: Four examples of configuration spaces. Position versus parameterized time. (a),(b) Convex and non convex configuration space with a corner of degree 1. (c),(d) Two instances of non convex configuration space with a corner of degree 2.

6.2 Analysis of a degree 2 corner impact bifurcation

Given the system in (6.1), let us assume that an impacting trajectory $x(t)$ characterized by one impact per period at some time instant $\tau \in \mathcal{I} =]-t_a, t_b[$ undergoes a corner impact bifurcation for $\mu = \mu_c$ at the point (x_c^-, τ_c). Moreover, assume that when $\mu < \mu_c$, the trajectory $x(t)$ has an impact with Σ_1 at time $t = \tau_1 < \tau_c$. We wish to investigate the effects on $x(t)$ of increasing μ past μ_c, *i.e.* the possible scenarios occurring at a corner impact bifurcation. (see Fig. 6.2(a)).

We assume $H_1(x_c^-, y_c) = H_2(x_c^-, y_c)$, $H_{1,t}(x_c^-, y_c) = H_{2,t}(x_c^-, y_c)$ and $H_{1,tt}(x_c^-, y_c) \neq H_{2,tt}(x_c^-, y_c)$ The former conditions are equivalent to say that, the point (x_c^-, y_c) is a corner of degree 2. We detail next, the construction of a Poincaré map to investigate the scenario described above.

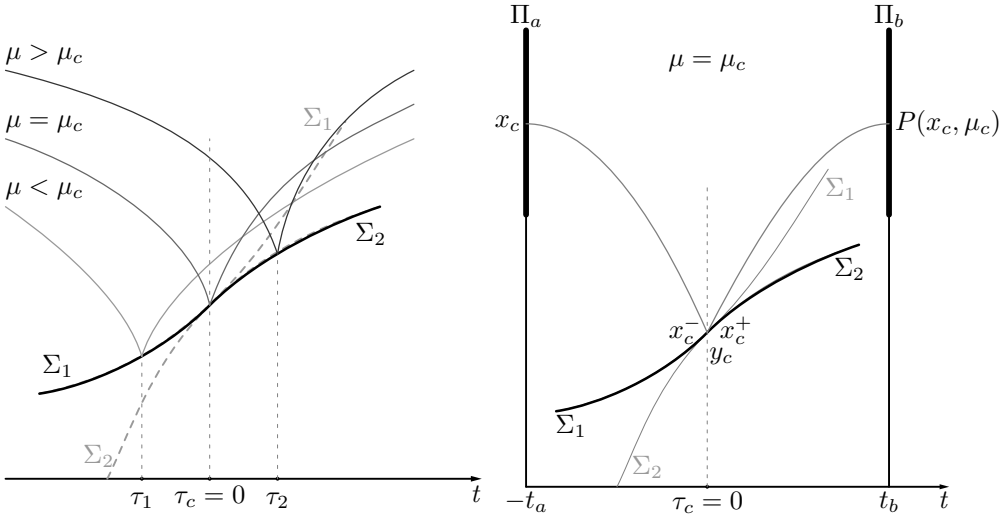

Figure 6.2: (a) Corner Impact Bifurcation. (b) Corner Impact Orbit.

6.2.1 Stroboscopic mapping

Let Π_a at $t = -t_a$ and Π_b at $t = t_b$ be two Stroboscopic Poincaré sections (see Fig. 6.2(b)). The corner impact trajectory is associated to the initial condition $x_c \in \Pi_a$, such that $x_c^- = \phi(x_c, t_a)$, $x_c^+ = R_1(x_c^-, y_c) = R_2(x_c^-, y_c)$ and $P(x_c, \mu_c) = \phi(x_c^+, t_b)$, where $\mu = \mu_c$ and (y_c, τ_c) define a corner. We wish to construct the mapping $P : \mathcal{A} \to \mathcal{B}$ from $\mathcal{A} \subset \Pi_a$ to $\mathcal{B} \subset \Pi_b$, where $\mathcal{A} \subset \Pi_a$ is a sufficiently small neighborhood of x_c, such that all trajectories rooted in $\mathcal{A}$ have one and only one impact occurring at $\tau \in \mathcal{I} =]-t_a, t_b]$ and $\mathcal{B}$ is the corresponding images on Π_b.

Now, for $\mu \leq \mu_c$ the point $x_c \in \mathcal{A}$ is mapped to the point $P(x_c, \mu) \in \mathcal{B}$ given by

$$P(x_c, \mu) = \phi(R_1(\phi(x_c, t_a + \tau_1), y_1(\tau_1)), t_b - \tau_1), \quad \text{if } \mu \leq \mu_c,$$

or equivalently, using an appropriate discontinuity mapping D, we can write:

$$P(x_c, \mu) = (\Phi_b \circ D \circ \Phi_a)(x_c, \mu), \quad \text{If } \mu \leq \mu_c, \tag{6.10}$$

where $\Phi_a : \Pi_a \to \Pi_d$ and $\Phi_b : \Pi_d \to \Pi_b$ are fixed time maps defined as

$$\Phi_a(x) = \phi(x, t_a), \qquad \Phi_b(x) = \phi(x, t_b), \tag{6.11}$$

and $D : \Pi_d \to \Pi_d$ is a *discontinuity map* acting on some section Π_d, that can be obtained from the composition of local flows and impacting dynamics near the point (x_c^-, τ_c); see Fig. 6.3.

Note that for $\mu \leq \mu_c$ the impact point lies on Σ_1. If we then vary μ past the bifurcation point the mapping changes as the impact point moves from Σ_1 to Σ_2. It has been observed in Chapter 5, that such phenomenon causes a non smooth transition, captured by introducing an extra discontinuity mapping D_c that allow us to write the global map as

$$P(x_c, \mu) = (\Phi_b \circ D_c \circ D \circ \Phi_a)(x_c, \mu), \quad \text{if } \mu > \mu_c, \tag{6.12}$$

where the map $D_c : \Pi_d \to \Pi_d$ is locally obtained from the composition of local flows and impacting dynamics near the point (x_c^+, τ_c); see Fig. 6.4. Next, we will show how to construct such maps D and D_c, and obtain the global Poincaré map using (6.12).

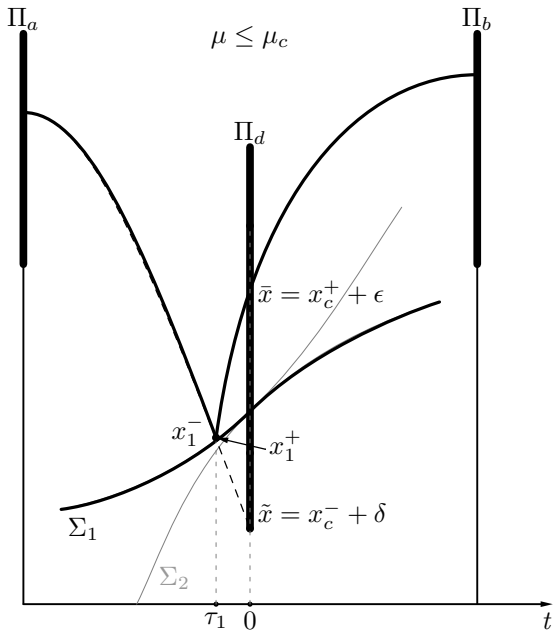

Figure 6.3: Construction of the Corner Impact Map D_c

6.3 Derivation of the map D

We first present the construction of the map D, that will model the interaction with Σ_1 as if the corner were not there; for small perturbations near the corner-impact orbit. We choose to construct the mapping on the section Π_d transversal to the flow at the corner. We consider a perturbed initial condition $\tilde{x} \in \Pi_d$, near the point x_c^- at time τ_c, defined as $\tilde{x} := x_c^- + \delta$ with small δ, (*i.e.* $\delta \approx 0$); we want to obtain in zero time, the correction ϵ to the perturbed post-impact state that we define as $\bar{x} := x_c^+ + \epsilon$, near the point (x_c^+, τ_c), such that for $\delta = 0$ we have $\epsilon = 0$, which means no perturbation implies no correction. Notice that D will then take into account perturbations of the impact dynamics. Fig. 6.3, presents the schematics for the construction of the mapping D, where we assume small perturbations on the parameter μ, nevertheless the local analysis performed in this section is generic for any perturbation on the initial condition $\tilde{x}$. This allows us the use of the discontinuity mapping D for the asymptotic and structural analysis. We can obtain D as a function of the local flows and impact dynamics by considering the following 3 steps (see Fig. 6.3):

1. Flow from $\tilde{x} \in \Pi_d$ for time $t = \tau_1$ using $\phi(\cdot, \cdot)$ generated by the vector field F in (6.1), to reach $x_1^- \in \Sigma_1$ *i.e.*
$$x_1^- := \phi(\tilde{x}, \tau_1) \tag{6.13}$$
where τ_1 is such that $H_1(\phi(\tilde{x}, \tau_1), y_1(\tau_1)) = 0$.

2. Using the pre-impact state $x_1^- \in \Sigma_1$ and the impact rule $R_1(\cdot, \cdot)$ to compute the post-impact state $x_1^+ \in \Sigma_1$ as
$$x_1^+ := R_1(x_1^-, y_1(\tau_1)) \tag{6.14}$$
where the impact rule R_1 is given by (6.5).

3. Flow backward from $x_1^+ \in \Sigma_1$ for time $t = -\tau_1$ till reach $\bar{x} \in \Pi_d$

$$\bar{x} := \phi(x_1^+, -\tau_1) \tag{6.15}$$

we can finally write D as function of $\tilde{x}$, after composing (6.13), (6.14) and (6.15) as,

$$\bar{x} = D(\tilde{x}) = \phi(R_1(\phi(\tilde{x}, \tau_1), y_1(\tau_1)), -\tau_1). \tag{6.16}$$

Note that the total time spent flowing backward and forward is zero. We present no two alternative derivations to obtain an analytical approximation of the map D: one based on asymptotics the other on implicit differentiation.

6.3.1 Local approximation of D using asymptotics

To obtain an analytical expression of $D(x)$, we can use the local Taylor expansion of $\phi(x,t)$ and $F(x)$ on perturbation of the initial conditions and time near the corner point $(x(\tau_c), \tau_c) = (x_c^-, 0)$ and $y_1(\tau_c) = y_c$. We have:

$$\begin{aligned}
x(t) = \phi(x,t)|_{\substack{x\approx x_0 \\ t\approx 0}} &= x + F(x_0)t + \mathcal{O}(2) && (6.17)\\
F(\phi(x,t))|_{\substack{x\approx x_0 \\ t\approx 0}} &= F(x_0) + F_x(x_0)(x-x_0) + F_x(x_0)F(x_0)t + \mathcal{O}(2) && (6.18)\\
y_i(t) = \gamma_i(y_c,t)|_{t\approx 0} &= y_c + G_i(y_c)t + \mathcal{O}(2) && (6.19)\\
G_i(\gamma_i(y_c,t))|_{t\approx 0} &= G_i(y_c) + G_{i,y_i}(y_c)G_i(y_c)t + \mathcal{O}(2) && (6.20)\\
\tau_1(x)|_{x\approx x_0} &= -\frac{C^T\delta}{C^T(F^0 - G_1^c)} + \mathcal{O}(2) = -\frac{1}{v_1^0}H_x \cdot x + \mathcal{O}(2) && (6.21)
\end{aligned}$$

where we use the superscript "-" or "+" to distinguish the approximation near x_c^- (*i.e.* $x_0 = x_c^-$), from the one near x_c^+. In the former case, we consider some perturbed initial condition $\tilde{x}$ near the corner impact at x_c^-, such that for $\delta \approx 0$ we have that $\tilde{x} \approx x_c^-$. We also use the superindex "c" to denote the state of the moving constraint at the corner as $G_1^c := G_1(y_c)$. The leading order approximation of $D(\tilde{x})|_{\tilde{x}\approx x_c^-}$ in (6.16) can then be obtained as follows:

1. From (6.13) and (6.17) with $\tilde{x} \approx x_c^-$ and $\tau_1^- \approx 0$, we obtain

$$\begin{aligned}
x_1^- &= \phi(\tilde{x}, \tau_1^-)\\
&= \tilde{x} + F^-\tau_1^- + \mathcal{O}(2).
\end{aligned} \tag{6.22}$$

2. From (6.5),(6.14),(6.18) with $x^- \approx x_c^-$ and $\tau_1^- \approx 0$, we have that

$$\begin{aligned}
x_1^+ &= R_1(x_1^-, y_1(\tau_1^-))\\
&= x_1^- - WC^T(F(x^-) - G_1(y_1(\tau_1^-)))\\
&= x_1^- - WC^T(F^- + F_x^-(x_1^- - x_c^-) - G_1^c - G_{1,y_1}^c G_1^c \tau_1^-) + \mathcal{O}(2)\\
&= R_1^- + R_{1,x}^-\delta + R_{1,t}^-\tau_1^-.
\end{aligned} \tag{6.23}$$

3. From (6.15) and (6.17) with $x_1^+ \approx x_c^+$ and $\tau_1^- \approx 0$, we get

$$\begin{aligned}
\bar{x} &= \phi(x_1^+, -\tau_1^-)\\
&= x_1^+ - F^+\tau_1^- + \mathcal{O}(2).
\end{aligned} \tag{6.24}$$

After composing (6.22), (6.24) and (6.24), we can write (6.16) as:

$$\begin{aligned}\bar{x} &= x_c^- + \delta + F^-\tau_1^- - WC^T(F^- + F_x^-\delta + F_x^-F^-\tau_1^- - G_1^c - G_{1,y_1}^c G_1^c\tau_1^-) \\ &\quad -F^+\tau_1^- + \mathcal{O}(2), \\ &= x_c^- - WC^T(F^- - G_1^c) + (I - WC^TF_x^-)\delta \\ &\quad +(F^- - WC^T(F_x^-F^- - G_{1,y_1}^c G_1^c) - F^+)\tau_1^- + \mathcal{O}(2) \\ &= R_1^- + R_{1,x}^-\delta + (R_{1,t}^- - F^+)\tau_1^- + \mathcal{O}(2) \end{aligned} \tag{6.25}$$

with

$$\begin{aligned} R_1^- &:= x_c^- - WC^T(F^- - G_1^c) = x_c^+, \\ R_{1,x}^- &:= I - WC^TF_x^- = \begin{bmatrix} 1 & 0 \\ 0 & -r \end{bmatrix}, \\ R_{1,y_1}^- &:= WC^TG_{1,y}^c = \begin{bmatrix} 0 & 0 \\ 0 & 1+r \end{bmatrix}, \\ R_{1,t}^- &:= R_{1,x}^-F^- + R_{1,y}^cG^c, \end{aligned}$$

where I is the identity matrix.

The approximation of τ_1^- can be obtained from (6.21) as:

$$\tau_{1,x}^- := -\frac{C^T}{C^T(F^- - G_1^c)} = -\frac{1}{v_1^-}H_x.$$

Notice that τ_1^- is function of δ, such that for $\delta = 0$ then $\tau_1^- = 0$.

We can then rewrite (6.25) as

$$\bar{x} := D(\tilde{x})|_{\tilde{x}=x_c^-+\delta} = R_1^- + (R_{1,x}^- + (R_{1,t}^- - F^+)\tau_{1,x}^-)\delta + \mathcal{O}(2). \tag{6.26}$$

For a perturbed initial condition $\tilde{x} = x_c^- + \delta$, we can compute the post-impact state $\bar{x} = x_c^+ + \epsilon$, decoupling the effect from the unperturbed orbit as

$$\epsilon := (R_{1,x}^- + (R_{1,t}^- - F^+)\tau_{1,x}^-)\delta + \mathcal{O}(2). \tag{6.27}$$

6.3.2 Local approximation of D using implicit differentiation

Alternatively, from (6.16) we can compute the jacobian $D_x(\tilde{x})|_{\tilde{x}=x_c{}^-}$ as

$$\begin{aligned} D_x(\tilde{x}) = \phi_x(x_1^+, -\tau_1)\cdot(R_{1,x}(x_1^-, y_1(\tau_1))\cdot(\phi_x(\tilde{x},\tau_1) + \phi_t(\tilde{x},\tau_1)\tau_{1,x}(\tilde{x})) \\ + R_{1,y}(x_1^-, y_1(\tau_1))\gamma_{1,t}(y_1(\tau_1),\tau_1)\tau_{1,x}(\tilde{x})) - \phi_t(x_1^+, -\tau_1)\tau_{1,x}(\tilde{x}) \end{aligned} \tag{6.28}$$

As we are interested on the analysis at $\tilde{x} = x_c^-$, we have that time $\tau_1 = 0$, and the jacobian $\phi_x(x_c^-, 0) = I$, moreover $\phi_t(x_c^-, 0) = F(x_c^-)$ and $\gamma_{1,t}(y, 0) = G_1(y)$ we can rewrite (6.28) as:

$$\begin{aligned} D_x(\tilde{x})|_{x=x_c{}^-} &= R_{1,x}(x_c{}^-) + (R_{1,x}(x_c{}^-, y_c)\cdot F(x_c{}^-) \\ &\quad +R_{1,y}(x_c{}^-, y_c)G_1(y_c) - F(x_c{}^+))\tau_{1,x}(x_c{}^-) \\ &= R_{1,x}^- + (R_{1,x}^-\cdot F^- + R_{1,y}^c\cdot G_1^c - F^+)\tau_{1,x}^- \end{aligned} \tag{6.29}$$

which lead us to the same expression as in (6.26).

6.4 Derivation of the corner map D_c

If we now vary μ past the bifurcation point the mapping changes as the impact point moves from Σ_1 to Σ_2. In particular we write the local map as

$$P(x,\mu) = (\Phi_b \circ D_c \circ D \circ \Phi_a)(x,\mu), \qquad \text{If } \mu > \mu_c. \tag{6.30}$$

where D_c represents the additional correction to the mapping due to the fact that for $\mu > \mu_c$, the impact now occurs with Σ_2 rather than Σ_1.

For the construction of the mapping D_c, we assume a perturbed initial condition $\bar{x} \in \Pi_d$ defined as $\bar{x} := x_c^+ + \epsilon$, with small ϵ (*i.e.* $\epsilon \approx 0$); after impacting Σ_1 near the point (x_c^+, τ_c). We want to obtain the zero time correction ξ to the perturbed postimpact state defined as $\hat{x} := x_c^+ + \xi$, after impacting Σ_2 near the point (x_c^+, τ_c)); such that for $\epsilon = 0$ we have $\xi = 0$.

Fig. 6.4, presents the schematics for the construction of the mapping D_c. We can then obtain D_c as function of local flows and impacting dynamics as follows:

1. Flow from $\bar{x} \in \Pi_d$ for time $t = \tau_1$ using $\phi(\cdot,\cdot)$ generated by the vector field F in (6.1), to reach $x_1^+ \in \Sigma_1$ *i.e.*
$$x_1^+ := \phi(\bar{x}, \tau_1), \tag{6.31}$$
where τ_1 is such that $H_1(\phi(\bar{x},\tau_1), y_1(\tau_1)) = 0$.

2. Given the post-impact state $x_1^+ \in \Sigma_1$, obtain the preimpact state $x_1^- \in \Sigma_1$ using the inverse function of the impact rule $R_1^{-1}(\cdot,\cdot)$ as
$$x_1^- := R_1^{-1}(x_1^+, y_1(\tau_1)), \tag{6.32}$$
where R_1^{-1} is defined by (6.9).

3. Flow from $x_1^- \in \Sigma_1$ for time $t = \tau_2 - \tau_1$ till reaching $x_2^- \in \Sigma_2$ as
$$x_2^- := \phi(x_1^-, \tau_2 - \tau_1), \tag{6.33}$$
where τ_2 is such that $H_2(\phi(x_1^-, \tau_2 - \tau_1), y_2(\tau_2)) = 0$.

4. Using the pre-impact state $x_2^- \in \Sigma_2$ and the impact rule $R(\cdot,\cdot)$ compute the post-impact state $x_2^+ \in \Sigma_2$ as
$$x_2^+ := R_2(x_2^-, y_2(\tau_2)) \tag{6.34}$$

5. Flow backward in time from $x_2^+ \in \Sigma_2$ for time $t = -\tau_2$ untill $\hat{x} \in \Pi_d$ given by
$$\hat{x} := \phi(x_2^+, -\tau_2) \tag{6.35}$$

composing (6.31), (6.32), (6.33), (6.34) and (6.35), we obtain:

$$\hat{x} = D_c(\bar{x}) \quad = \quad \phi(R_2(\phi(R_1^{-1}(\phi(\bar{x},\tau_1), y_1(\tau_1)), \tau_2 - \tau_1), y_2(\tau_2)), -\tau_2). \tag{6.36}$$

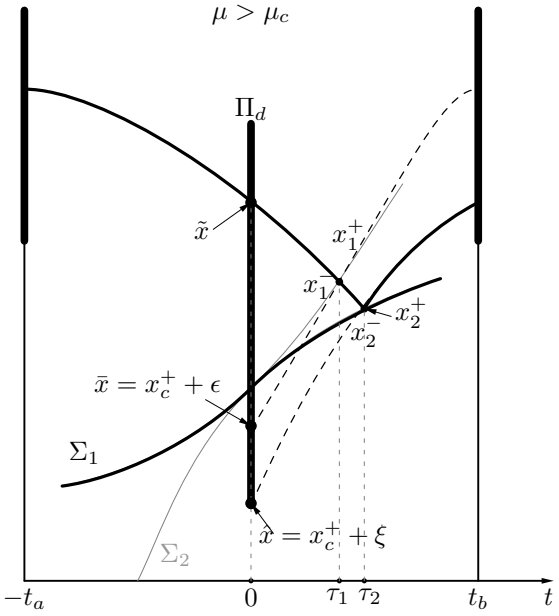

Figure 6.4: Construction of the Corner Impact Map D_c

6.4.1 Local approximation of D_c using asymptotics

Now we use (6.17), (6.18), to write a first order approximation of $D_c(\bar{x})|_{\bar{x}\approx x_c^+}$ in (6.36) as follows:

1. From (6.31) and (6.17) with $\bar{x} \approx x_c^+$ and $\tau_1^+ \approx 0$

$$\begin{aligned} x_1^+ &= \phi(\bar{x}, \tau_1^+) \\ &= \bar{x} + F^+ \tau_1^+ + \mathcal{O}(2). \end{aligned} \tag{6.37}$$

2. From (6.5),(6.32),(6.18) and (6.20) with $x_1^+ \approx x_c^+$ and $\tau_1 \approx 0$, we have that

$$\begin{aligned} x_1^- &= R_1^-(x_1^+, y_1(\tau_1^+)) \\ &= x_1^+ - \frac{1}{r} W C^T (F(x_1^+) - G_1(y_1(\tau_1^+))) \\ &= x_1^+ - \frac{1}{r} W C^T (F^+ + F_x^+ (x_1^+ - x_c^+) - G_1^c - G_{1,y_1}^c G_1^c \tau_1^+) + \mathcal{O}(2) \end{aligned} \tag{6.38}$$

3. From (6.33) and (6.17) with $x_1^- \approx x_c^-$, $\tau_1^+ \approx 0$ and $\tau_2^+ \approx 0$, we have:

$$\begin{aligned} x_2^- &= \phi(x_1^-, \tau_2^+ - \tau_1^+) \\ &= x_1^- + F^-(\tau_2^+ - \tau_1^+) + \mathcal{O}(2). \end{aligned} \tag{6.39}$$

4. From (6.5),(6.20),(6.18) and (6.34),with $x_2^- \approx x_c^-$ and $\tau_2^+ \approx 0$, we get:

$$\begin{aligned} x_2^+ &= R_2(x_2^-, y_2(\tau_2^+)) \\ &= x_2^- - W C^T (F(x_2^-) - G_1(y_2(\tau_2^+))) \\ &= x_2^- - W C^T (F^- + F_x^- (x_2^- - x_c^-) - G_2^c - G_{2,y_2}^c G_2^c \tau_2^+) + \mathcal{O}(2). \end{aligned} \tag{6.40}$$

5. (6.35) and (6.17) with $x_2^+ \approx x_c^+$ and $\tau_2 \approx 0$, yield

$$\begin{aligned} \hat{x} &= \phi(x_2^+, -\tau_2) \\ &= x_2^+ - F^+\tau_2^+ + \mathcal{O}(2) \end{aligned} \tag{6.41}$$

After composing (6.37), (6.38), (6.39), (6.40) and (6.41) we can then write

$$\hat{x} = D_c(\bar{x})|_{\bar{x}\approx x_c^+} = x_c^+ + \epsilon - (R_{1,t}^- - F^+)\tau_{1,x}^+\epsilon + (R_{2,t}^- - F^+)\tau_{2,x}^+\epsilon + \mathcal{O}(2) \tag{6.42}$$

Notice that, τ_1^+ and τ_2^+ are functions of ϵ and the approximation can be obtained from (6.21) as

$$\tau_{1,x}^+ = -\frac{C^T}{C^T(F^+ - G_1^c)} = -\frac{1}{v_1^+}H_x, \qquad \text{and} \qquad \tau_{2,x}^+ = -\frac{C^T}{C^T(F^+ - G_2^0)} = -\frac{1}{v_2^+}H_x.$$

From (6.42), we can decouple the effect of the perturbation ϵ as

$$\xi = (I - (R_{1,t}^- - F^+)\tau_{1,x}^+ + (R_{2,t}^- - F^+)\tau_{2,x}^+)\epsilon + \mathcal{O}(2). \tag{6.43}$$

6.4.2 Local approximation of D_c using implicit differentiation

From (6.36) we can compute the jacobian $D_{c,x}(\bar{x})|_{\bar{x}=x_c^+}$ as

$$\begin{aligned} D_{c,x}(\bar{x}) &= \phi_x(x_2^+, -\tau_2)\cdot(R_{2,x}(x_2^-, y_2(\tau_2))\cdot(\phi_x(x_1^-, \tau_2 - \tau_1) \\ &\quad \cdot(R_{1,x}^{-1}(x_1^+, y_1(\tau_1))\cdot(\phi_x(x_2^+, -\tau_1) + \phi_t(x_1^+, \tau_1)\tau_{1,x}(\bar{x})) \\ &\quad + R_{1,y}^{-1}(x_1^+, y_1(\tau_1))\gamma_{1,t}(y_1(\tau_1), \tau_1)\tau_{1,x}(\bar{x})) + \phi_t(x_1^-, \tau_1)(\tau_{2,x}(\bar{x}) - \tau_{1,x}(\bar{x})) \\ &\quad + R_{2,y}(x_2^-, y_2(\tau_2))\gamma_{2,t}(y_2(\tau_2), \tau_2)\tau_{2,x}(\bar{x})) - \phi_t(x_2^+, \tau_2)\tau_{2,x}(\bar{x})) \end{aligned} \tag{6.44}$$

because at $\bar{x} = x_c^-$, we have that time $\tau_1 = 0$, $\tau_2 = 0$ and the jacobian $\phi_x(x, 0) = I$, as well as $\phi_t(x, 0) = F(x)$ and $\gamma_{i,t}(y, 0) = G_i(y)$. Now, from (6.45) we have

$$D_{c,x}(\bar{x})|_{\bar{x}=x_c^+} = I - (R_{1,t}^- - F^+)\tau_{1,x}^+\epsilon + (R_{2,t}^- - F^+)\tau_{2,x}^+ \tag{6.45}$$

which lead us to the compact form in (6.43).

6.4.3 Sensitivity of D and D_c under parameter variation

We consider now the effects of variation of the parameter μ, on the maps D and D_c defined in Sec. 6.3 and 6.4. Namely, we note that any small variation on the parameters of the system, say $\mu = \mu_c + \Delta\mu$, with $\Delta\mu \ll 1$; may produce a deviation from the post-impact state associated to the corner impacting orbit Now, if we define ϵ_μ as the correction to the post-impact state caused by variation of the parameter vector μ, we can repeat the local analysis. In particular, we obtain $\epsilon_\mu = D_\mu\Delta\mu$, for impacts occurring before the corner point at $\tau \leq \tau_c$, where

$$D_\mu(\mu) = R_{1,\mu} + (R_{1,t}^- - F^+)\tau_{1,\mu}^-, \tag{6.46}$$

and for the case of impacts occurring at $\tau > \tau_c$, we will need to consider the additional correction $D_{c,\mu}$ given by

$$D_{c,\mu}(\mu) = I - (R_{1,t}^- - F^+)\tau_{1,\mu}^+ + (R_{2,t}^- - F^+)\tau_{2,\mu}^+. \tag{6.47}$$

In section **??**, we include examples of analysis for a representative cam-follower system.

6.5 Derivation of the global Poincaré map

We can now use the analytical approximation of D and D_c to obtain the global Poincaré map defined in (6.10) and (6.12). Say $\mathcal{A}_\mu \subset [\Pi_a \times R^1]$ a sufficiently small neighborhood of the point(x_c, μ_c), such that all trajectories rooted in $\mathcal{A}_\mu$ have one and only one impact occurring at $\tau \in \mathcal{I} =]-t_a, t_b]$. Now, for $\tau(x,\mu) \leq \tau_c$ the point $x \in \mathcal{A}_\mu$ is mapped to the point $P(x,\mu) \in \mathcal{B} \subset \Pi_b$ given by

$$P(x,\mu) = \begin{cases} (\Phi_b \circ D \circ \Phi_a)(x,\mu), & \text{If } \tau(x,\mu) \leq \tau_c \\ (\Phi_b \circ D_c \circ D \circ \Phi_a)(x,\mu), & \text{If } \tau(x,\mu) > \tau_c \end{cases} \tag{6.48}$$

where $\Phi_a(x)$ and $\Phi_b(x)$ are given by (6.11) and $D(x)$ and $D_c(x)$ are given by (6.16) and (6.36).

As mentioned before, the corner impact trajectory is associated to an initial condition $x_c \in \Pi_a$ with $\mu = \mu_c$, such that $x_c^- = \phi(x_c, t_a)$ when $\mu = \mu_c$. (see Fig. 6.2(b)).

Let Δx and $\Delta\mu$ be sufficiently small variation of the state and parameter near x_c and μ_c, such that the point $(x_c + \Delta x, \mu_c + \Delta\mu) \subset \mathcal{A}_\mu$. Then, we can write a linear approximation of (6.48) near a corner of degree 2 as

$$\Delta P(x,\mu)|_{\substack{x \approx x_c \\ \mu \approx \mu_c}} = P_x(x_c,\mu_c)\Delta x + P_\mu(x_c,\mu_c)\Delta\mu + \mathcal{O}(||\Delta x||^2, ||\Delta\mu||^2)$$

where

$$P_x(x_c,\mu_c) := \begin{cases} \phi_x(x_c^+, t_b) \cdot D_x(x_c^-) \cdot \phi_x(x_c, t_a) & \text{If } \tau(x,\mu) \leq \tau_c \\ \phi_x(x_c^+, t_b) \cdot D_{c,x}(x_c^+) \cdot D_x(x_c^-) \cdot \phi_x(x_c, t_a) & \text{If } \tau(x,\mu) > \tau_c \end{cases} \tag{6.49}$$

and

$$P_\mu(x_c,\mu_c) := \begin{cases} \phi_\mu(x_c^+, t_b) \cdot D_\mu(x_c^-) \cdot \phi_\mu(x_c, t_a) & \text{If } \tau(x,\mu) \leq \tau_c \\ \phi_\mu(x_c^+, t_b) \cdot D_{c,\mu}(x_c^+) \cdot D_\mu(x_c^-) \cdot \phi_\mu(x_c, t_a) & \text{If } \tau(x,\mu) > \tau_c \end{cases} \tag{6.50}$$

where D_c, $D_{c,x}$, D_μ and $D_{c,\mu}$ are defined by (6.28), (6.45), (6.46) and (6.47) respectively.

6.6 Stability of periodic orbits near a corner of degree 2

Probably the most straightforward use of the methodology presented above, is the analysis of periodic orbits with impacts near to a corner. As an example, Fig. 6.5 shows position versus time, of the simplest orbit undergoing a corner impact bifurcation. It is assumed the existence of an isolated periodic (1,1) orbit (noted as $\mathcal{P}(1,1)$) impacting a corner of degree 2 of the type depicted in Fig. 6.1(c). In order to study the asymptotic and structural stability of such an orbit, we proceed with the construction of a proper Poincaré mapping. In this case it is convenient to define the stroboscopic Poincaré section Π_i every period, that allows the definition of the map $P : \Pi_i \to \Pi_{i+1}$. In this particular case we assume the map is invertible near the fixed point associated to the periodic orbit, which means that there are not grazing bifurcations or sliding solutions belonging to orbit. It is also worth mentioning that the map P will take care of the free flow evolution of the systems, as well as of the impact dynamics. Fig. 6.6 shows the same $\mathcal{P}(1,1)$ orbit in the state space (*i.e.* position, velocity and time).

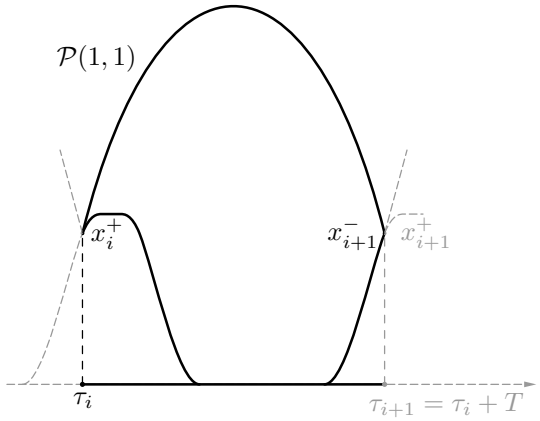

Figure 6.5: Position on time for a (1,1) impacting orbit

Using the methodology described above we can write the Poincarḿap of this orbit as:

$$P(x,\mu) = \begin{cases} (D \circ \Phi_1)(x,\mu), & \text{If } \tau(x,\mu) \leq \tau_c \\ (D_c \circ D \circ \Phi_1)(x,\mu), & \text{If } \tau(x,\mu) \leq \tau_c. \end{cases} \tag{6.51}$$

Now if, x_c is the fixed point of this mapping corresponding to the orbit of interest we can write:

$$\Delta P(x,\mu)|_{\substack{x \approx x_c \\ \mu \approx \mu_c}} = P_x(x_c,\mu_c)\Delta x + P_\mu(x_c,\mu_c)\Delta\mu + \mathcal{O}(||\Delta x||^2, ||\Delta\mu||^2)$$

and study the asymptotic stability using:

$$P_x(x_c,\mu_c) = \begin{cases} D_x(x_c^-) \cdot \phi_x(x_0,T) & \text{If } \tau(x,\mu) \leq T \\ D_{c,x}(x_c^+) \cdot D_x(x_c^-) \cdot \phi_x(x_0,T) & \text{If } \tau(x,\mu) > T \end{cases} \tag{6.52}$$

while the structural stability using:

$$P_\mu(x_c,\mu_c) = \begin{cases} D_\mu(x_c^-) \cdot \phi_\mu(x_c^+,t_a) & \text{If } \tau(x,\mu) \leq T \\ D_{c,\mu}(x_c^+) \cdot D_\mu(x_c^-) \cdot \phi_\mu(x_c^+,t_a) & \text{If } \tau(x,\mu) > T \end{cases} \tag{6.53}$$

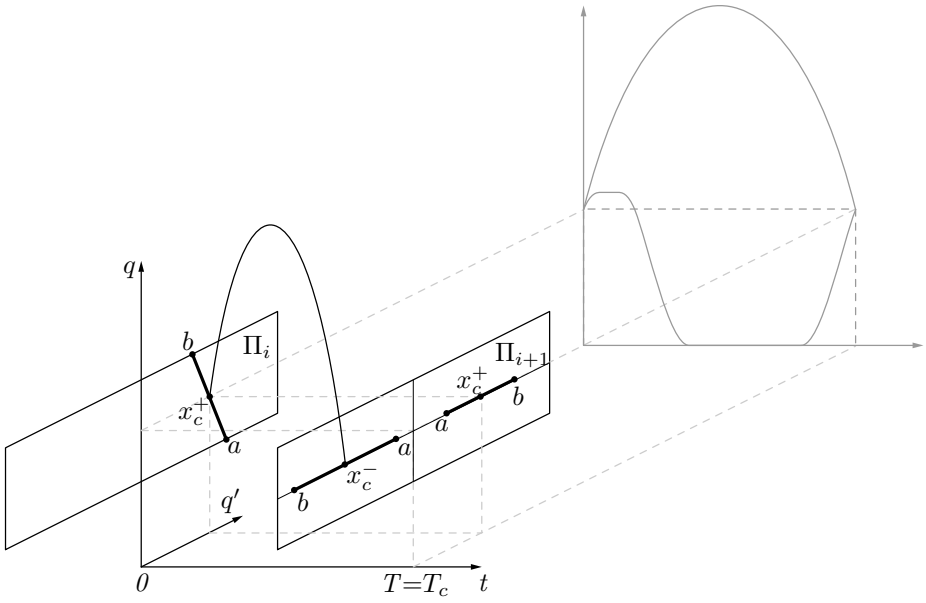

Figure 6.6: Simplest orbit undergoing a corner impact bifurcation

6.7 Corner impact bifurcation in the cam–follower system

We now illustrate the derivation of *corner impact map* D_c presented in this chapter, for the complete analysis of a corner impact bifurcation in the cam–follower system.

6.7.1 Definition of the impacting system

The dynamics of the mass-spring-damper system is described by the second order differential equation

$$mq'' + bq' + kq = -mg, \tag{6.54}$$

if we define q_0 and q_0' as the initial position and velocity of the follower. The state of the system can be defined as

$$x(t) = \begin{bmatrix} q(t), \\ \dot{q}(t) \end{bmatrix} + \frac{mg}{k} \begin{bmatrix} 1 \\ 0 \end{bmatrix}$$

the differential form

$$\begin{aligned} \dot{x} &= F(x), \\ &= Ax, \end{aligned}$$

where $F(x)$ is a linear vector field generator the flow $\phi(x_0, t)$ such that

$$\begin{aligned} x(t) &= \phi(x_0, t), \\ &= e^{-\zeta t} \left(I \cos(\omega_s t) + D \sin(\omega_s t) \right) x_0, \\ &= \Phi(t) x_0, \end{aligned}$$

where $A = \begin{bmatrix} 0 & 1 \\ -\omega_0^2 & -2\zeta \end{bmatrix}$, $D = \frac{1}{\omega_s}\begin{bmatrix} \zeta & 1 \\ -\omega_0^2 & -\zeta \end{bmatrix}$, $\zeta = \frac{b}{2m}$, $\omega_0 = \sqrt{\frac{k}{m}}$, $\omega_s = \sqrt{\omega_0^2 - \zeta^2}$

Definition of constraints Σ_1 and Σ_2. The geometrical construction of the cam allow us define the constraints Σ_1 and Σ_2 by the zero level set of smooth scalar functions H_1 and H_2 as

$$H_i(x(t), y_i(t)) = C^T(x(t) - y_i(t)) \quad \text{and} \quad \Sigma_i = \{x : H_i(x, y) = 0\},$$

for $i \in \{1, 2\}$ and $C^T = [\ 1 \quad 0\ ]$.

$$y_i(t) = \begin{bmatrix} (-1)^i \kappa_i \sin(\omega t + \theta + \theta_i) + (\rho_i^2 - \kappa_i^2 \cos(\omega t + \theta + \theta_i)^2)^{\frac{1}{2}} \\ (-1)^i \kappa_i \cos(\omega t + \theta + \theta_i) + \frac{\kappa_i^2 \sin(\omega t+\theta+\theta_i)\cos(\omega t+\theta+\theta_i)}{(\rho_i^2 - \kappa_i^2 \cos(\omega t+\theta+\theta_i)^2)^{\frac{1}{2}}} \end{bmatrix} \tag{6.55}$$

where ω, θ, κ_i, ρ_i and θ_i are constant parameters . It can be shown that $y_1(0) = y_2(0)$ as well as

$$H_1(t)|_{t=0} = H_2(t)|_{t=0}, \quad \left.\frac{\partial H_1(t)}{\partial t}\right|_{t=0} = \left.\frac{\partial H_2(t)}{\partial t}\right|_{t=0} \quad \text{and} \quad \left.\frac{\partial^2 H_1(t)}{\partial t^2}\right|_{t=0} \neq \left.\frac{\partial^2 H_2(t)}{\partial t^2}\right|_{t=0}.$$

Impact dynamics. The dynamics at impact is defined as

$$\begin{aligned} x^+ = R_i(x^-, y_i(\tau_i)) &= x^- - W(x^-) v_i(x^-, y_i^-), \\ &= x^- - W(x^-) C^T \left[F(x^-) - G_i(\tau_i)\right], \end{aligned} \tag{6.56}$$

where $W(x^-) = [\ 0 \quad (1+r)\ ]^T$ and $G_i(y_i(t)) = y_{i,t}(t)$.

6.7.2 Local analysis for the cam-follower system

Using the analytical tools presented in section 6.2 we can obtained the local approximations for the map in (6.48) as

$$P_x(x_c, \mu_c) = \begin{cases} \phi_x(x_c^+, t_b) \cdot D_x(x_c^-) \cdot \phi_x(x_0, t_a), & \text{If } \mu \leq \mu_c, \\ \phi_x(x_c^+, t_b) \cdot D_{c,x}(x_c^+) \cdot D_x(x_c^-) \cdot \phi_x(x_0, t_a) & \text{If } \mu > \mu_c, \end{cases} \tag{6.57}$$

where for the cam-follower system we have:

$$\begin{aligned} \Phi_a &= \Phi(t_a) = \phi_x(x_0, t_a) = e^{-\zeta t_a}\left(I\cos(\omega_s t_a) + D\sin(\omega_s t_a)\right), \\ \Phi_b &= \Phi(t_b) = \phi_x(x_c^+, t_b) = e^{-\zeta t_b}\left(I\cos(\omega_s t_b) + D\sin(\omega_s t_b)\right), \end{aligned}$$

$$D_x(x) = R_x + \left(\ R_x(F(x_c^-) - G_1(y_c)) - (F(x_c^+) - G_1(y_c))\ \right)\tau_{1,x},$$

or

$$D_x(x) = R_x + \left(\ R_x F(x_c^-) + R_y G_1(y_c) - F(x_c^+)\ \right)\tau_{1,x},$$

with

$$\tau_{1,x} = -\frac{C^T}{C^T \cdot \left(F(x_c^-) - G_1(y_c)\right)},$$

$$R_x = I - W(x^-)C^T F_x(x^-) = I + R = \begin{bmatrix} 1 & 0 \\ 0 & -r \end{bmatrix},$$

$$R_y = W(x^-)C^T G_y(y^-) = -R = \begin{bmatrix} 0 & 0 \\ 0 & 1+r \end{bmatrix},$$

and $R = -W(x^-)C^T F_x(x^-) = \begin{bmatrix} 0 & 0 \\ 0 & -(1+r) \end{bmatrix}$.

Moreover, we obtain:

$$\begin{aligned} F(x_c^-) &= Ax_c^- = \phi'(0)x_c^-, \\ G_1(y_c) &= G_1(y_1(0)) = y_1'(0), \\ \Delta F_1^- &= F(x_c^-) - G_1(y_c) = \phi'(0)x_c^- - y_1'(0), \\ \Delta F_1^+ &= F(x_c^+) - G_1(y_c) = \phi'(0)x_c^+ - y_1'(0), \\ x_c^+ &= x_c^- - W(x^-)C^T(F(x_c^-) - G_1(y_c)), \\ &= x_c^- + R(x_c^- - y_1(0)). \end{aligned}$$

These analytical mappings can be used to study the dynamics of any cam–follower system of interest.

For the sake of brevity we omit here the analysis of the cam–follower system of interest which yields the same results presented in Chapter 5.

Chapter 7

Analysis of Limit Cycles in Hybrid Anti–lock Braking Systems

Contents

In this chapter we study an hybrid controller for an *Anti–lock Braking System* (ABS) in the context of the Qualitative theory of Piecewise Smooth Dynamical Systems. To the best of our knowledge, this type of ABS has never been fully analyzed. Our interest is to characterize the performance (stability and robustness), rather than focusing on the design of new ABS control algorithms. We believe that our approach can give useful synthesis tools as it shows how a simple hybrid controller with a low number of both discrete states and parameters can be designed to guarantee stability and robustness.

The work presented in this chapter was carried out in collaboration with Mara Tanelli and Sergio M. Savaresi from the *"Dipartmento di Electtronica e Informazione, Politecnico di Milano"*, and Alessandro Astolfi from the Department of Electrical and Electronic Engineering, Imperial College, London.

7.1 Description of the ABS hybrid controller

Electronic *Anti-lock Braking Systems* (ABS) have recently become a standard for all modern cars. In fact, ABS can greatly improve the safety of a vehicle in extreme

circumstances, as it maximizes the longitudinal tire-road friction while keeping large lateral forces which guarantee vehicle steerability. The use of automatic braking control systems has recently been extended also to Electronic Stability Control (ESC) systems [27], [39].

This advanced control techniques, although very powerful, do rely on a new generation of braking system which are not an industrial reality yet. This is mainly due to the fact that both electro-hydraulic and electro-mechanical braking systems do not yet have been proved to comply with the safety standards required for this highly safety-critical application (see *e.g.,* [68], [27]). We now present an hybrid controller for an anti–lock breaking system with a threevalued hydraulic actuator, modelled as a piecewise smooth dynamical system.

7.1.1 Braking model

For the preliminary design and testing of braking control algorithms, a simple but effective quarter-car model (see *e.g.,* [36]) is typically used. The model is given by the following set of equations (see also Figure 7.1)

$$J\dot{\omega} = rF_x - T_b, \tag{7.1a}$$
$$m\dot{v} = -F_x, \tag{7.1b}$$

where

- ω $[rad/s]$ is the angular speed of the wheel;
- v $[m/s]$ is the longitudinal speed of the vehicle body;
- T_b $[Nm]$ is the braking torque (which plays the role of control/input variable);
- F_x $[N]$ is the longitudinal tire-road contact force;
- J $[Kg\,m^2]$, m $[Kg]$ and r $[m]$ are the moment of inertia of the wheel, the quarter-car mass, and the wheel radius, respectively. In the following simulations and Figures, unless otherwise stated, the values $J = 1\,[Kg\,m^2]$, $m = 400\,[Kg]$ and $r = 0.3\,[m]$ will be used.

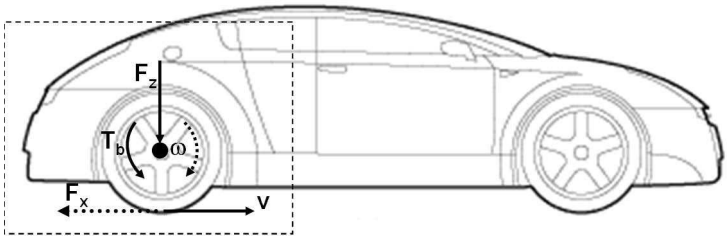

Figure 7.1: Quarter car vehicle model.

The dynamic nonlinear behavior of the system is hidden in the expression of F_x, which depends on the state variables v and ω. The most general expression of F_x is quite involved, since it depends on a large number of features of the road, tire, and suspension. However, it can be well-approximated as follows

$$F_x = F_z\mu(\lambda, \beta_t; \theta_r), \tag{7.2}$$

where

- F_z is the vertical force at the tire-road contact point;
- λ is the longitudinal slip, defined as $\lambda = \frac{v-\omega r}{\max\{\omega r, v\}}$. Notice that, by definition, $\lambda \in [-1, 1]$; during braking, though, as $\omega r \leq v$, the wheel slip is defined as

$$\lambda = \frac{v - \omega r}{v},$$

  and $\lambda \in [0, 1]$;
- β_t is the wheel side-slip angle (see *e.g.,* [39]);
- ϑ_r is a set of parameters which characterize the shape of the static function $\mu(\lambda, \beta_t; \vartheta_r)$.

For simplicity, we assume that the braking maneuver is performed along a straight line, (*i.e.* $\beta_t = 0$).This assumption is not crucial in the design, since β_t acts as a scaling factor on the friction curves $\mu(\lambda)$, which resembles the effect due to a change in the vertical load.
Accordingly, as we will discuss how changes in the vertical load can be managed in the proposed control approach, in the same way we can handle non-zero values of β_t.
Many empirical analytical expressions for $\mu(\cdot; \vartheta_r)$ have been proposed; a simple and widely-used model is (see [39], [48])

$$\mu(\lambda; \vartheta_r) = \vartheta_{r1}(1 - e^{-\lambda\vartheta_{r2}}) - \lambda\vartheta_{r3}. \tag{7.3}$$

Notice that $\vartheta_r \in \mathbb{R}^3$ is a parameter vector to model different tire-road friction conditions. In Figure 7.2 the shapes of $\mu(\lambda; \vartheta_r)$ in four different road conditions are displayed.

We will analyze the case of dry asphalt and wet asphalt, where ϑ_r are $\theta_{rDry} = [1.11\ 23.99\ 0.52]$ and $\theta_{rWet} = [0.687\ 33.822\ 0.347]$, (see [39]). After these assumptions we can model (7.2) as

$$F_x = F_z\mu(\lambda), \tag{7.4}$$

with $\lambda = \frac{v-\omega r}{v}$.

Substituting (7.4) into (7.1) we obtain a quarter–car model as

$$J\dot{\omega} = rF_z\mu(\frac{v - \omega r}{v}) - T_b, \tag{7.5a}$$

$$m\dot{v} = -F_z\mu(\frac{v - \omega r}{v}). \tag{7.5b}$$

Nonetheless, as λ, v and ω are linked by an algebraic relationship, it is possible to replace the state variable ω with the state variable λ. This can be simply obtained by substituting the following two relationships

$$\dot{\lambda} = -\frac{r}{v}\dot{\omega} + \frac{r\omega}{v^2}\dot{v}$$

and

$$\omega = \frac{v}{r}(1 - \lambda)$$

into the first Equation of (7.5), thereby obtaining

$$\dot{\lambda} = -\frac{1}{v}\left(\frac{(1-\lambda)}{m} + \frac{r^2}{J}\right)F_z\mu(\lambda) + \frac{r}{vJ}T_b, \tag{7.6a}$$

$$m\dot{v} = -F_z\mu(\lambda). \tag{7.6b}$$

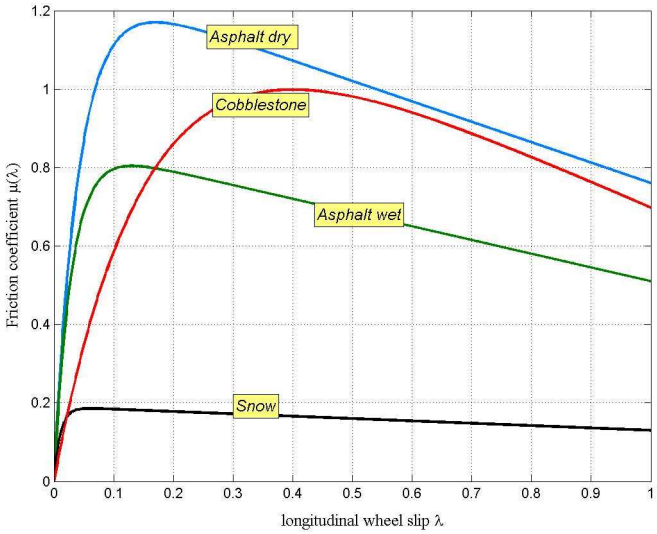

Figure 7.2: Behavior of the function $\mu(\lambda)$ in different road conditions.

Since the longitudinal dynamics of the vehicle (*i.e.* state variable v) are much slower than the rotational dynamics of the wheel (*i.e.* the state variable λ or ω) due to large differences in inertia (7.1b) is neglected, and we reduce to a first order model given by

$$\dot{\lambda} = -\frac{1-\lambda}{J\omega}\left(\Psi(\lambda) - T_b\right), \tag{7.7}$$

with $\omega \geq 0$ and

$$\Psi(\lambda) = \left(r + \frac{J}{rm}(1-\lambda)\right) F_z \mu(\lambda). \tag{7.8}$$

7.1.2 Actuator dynamics and closed loop trajectories

The considered actuator is the *Hydraulic Actuated Brake* (HAB) depicted in Fig. 7.3. For this HAB the pressure exerted by the driver on the pedal is transmitted to the hydraulic system via a Build Valve (valve 1), which communicates with the brake cylinder. Moreover, the hydraulic system has a second valve, the Dump Valve (valve 2), which can discharge the pressure and which is connected to a low pressure accumulator. A pump completes the overall system.

According to its physical characteristics, the HAB actuator is only capable of providing three different control actions, namely

- *Increase* the brake pressure. In this case the Build valve is open and the Dump one closed;
- *Hold* the brake pressure. In this case both valves are closed;
- *Decrease* the brake pressure. In this case the Build valve is closed and the Dump one open.

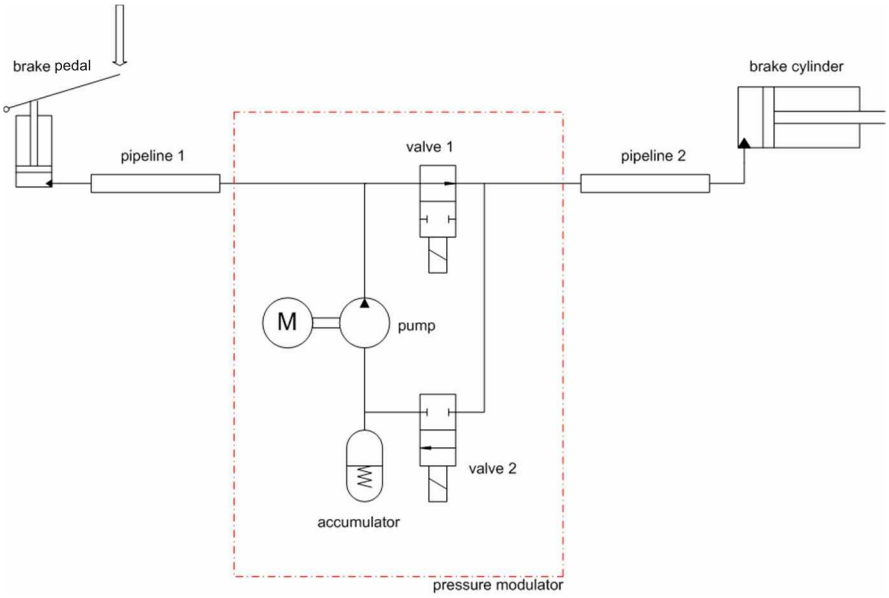

Figure 7.3: Qualitative scheme of the considered braking system.

We assume a static brake-pads friction model, *i.e.,* the braking torque T_b is computed from the measured brake pressure p_b as

$$T_b = r_d \, \nu \, A \, p_b,$$

where r_d is the brake disk radius; ν is the (constant) brake pads friction coefficient; A is the brake piston area and p_b is the measured brake pressure. This simplification does not affect the analysis; in fact, in Sec. 7.4 we will show how the controller can take care of uncertainties in the braking torque and how to tune the controller parameters according to the available actuator performance.

Note that the increase and decrease pressure actions are physically limited by the actuator rate limit, *i.e.*,

$$\frac{dT_b}{dt} = k,$$

where the rate limit $k \in \mathbb{R}^+$ is a known parameter. Its nominal value in the following simulations will be set to $10\,kN/s$.

To analyze the closed loop behavior of the hybrid system made of the connection between the wheel dynamics (7.7) and the hydraulic actuator, we will work on the second order system dynamics

$$\dot{\lambda} = -\frac{1-\lambda}{J\omega}\left(\Psi(\lambda) - T_b\right), \tag{7.9a}$$

$$\dot{T}_b = u, \tag{7.9b}$$

where we define three dynamical modes that corresponds to $u = \{-k, 0, k\}$. In Figs. 7.4(a), 7.4(b) and 7.4(c) we present the phase portrait for each dynamical mode using a vertical load $F_z = mg$, for $v = 30\,m/s$ on a dry asphalt road. The dashed line in these figures is the isocline given by (7.8).

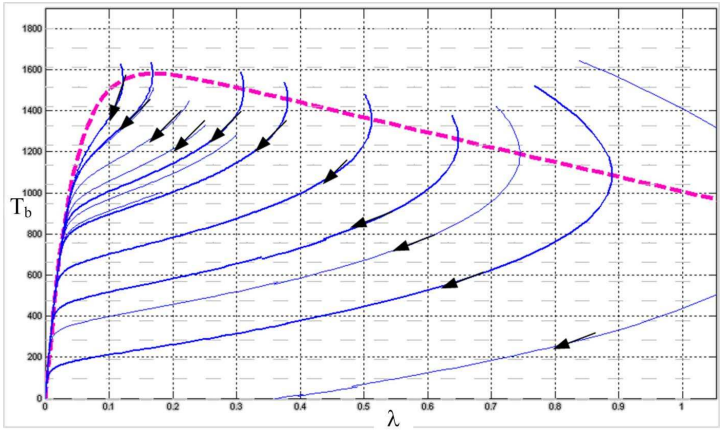

(a)

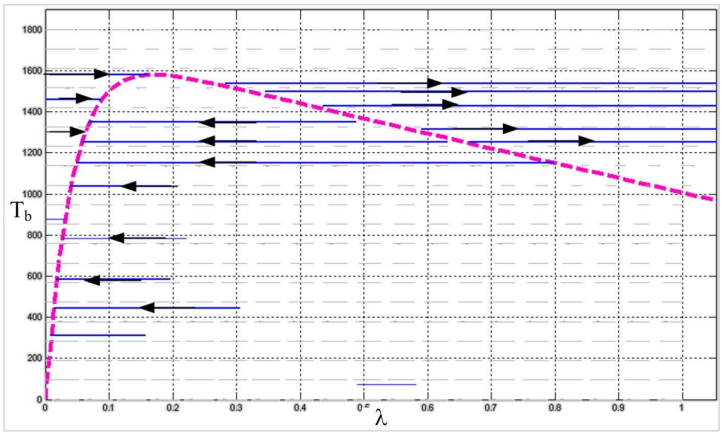

(b)

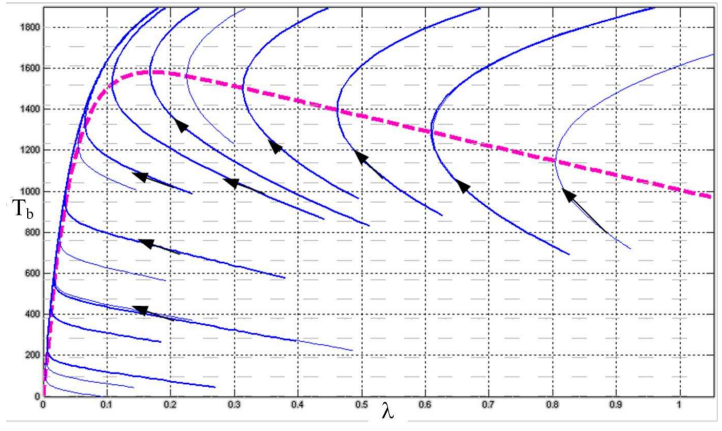

(c)

Figure 7.4: Phase portrait for the close-loop braking system with a threevalued u. (a) $u = -k$. (b) $u = 0$. (c) $u = k$.

Notice that for $u = 0$ depending on the value of T_b we can have different scenarios (invariant sets) in the phase portrait. In Fig. 7.5 we present a manifold Σ_{ss} obtained from (7.9a) with $T_b = 1300\ Nm$. In this case the phase portrait presents two stable equilibria, namely wheel locking equilibrium at $\lambda_1^{ss} = 1$ and the equilibria on the isocline λ_2^{ss}; and an unstable equilibrium λ_3^{is} at another intersection point with the isocline.

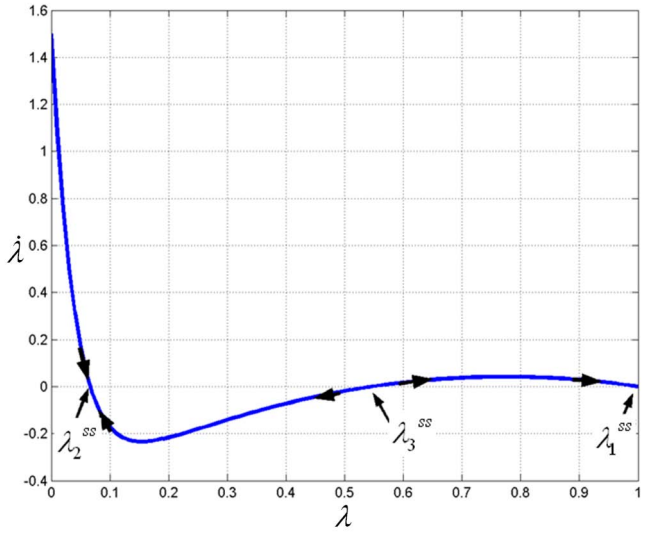

Figure 7.5: Graph of $\dot{\lambda}$ as a function of λ.

7.1.3 Hybrid controller

After analyzing the phase portrait for each of the three different dynamical modes defined by the actuator, we can devise a switching logic which induces a limit cycle on the wheel slip. We select the box depicted in Figure 7.6. The idea is to use the boundaries of the box as switching functions and to select the control actions according to the finite state machine shown in Fig. 7.7

We define the switching manifolds as follows (see also Figure 7.6)

$$\Sigma_0 = \{(\lambda, T_b) : H_0(\lambda, T_b) := T_b - T_{bMax} = 0\}, \tag{7.10}$$
$$\Sigma_1 = \{(\lambda, T_b) : H_1(\lambda, T_b) := \lambda - \lambda_{Max} = 0\}, \tag{7.11}$$
$$\Sigma_2 = \{(\lambda, T_b) : H_2(\lambda, T_b) := T_b - T_{bMin} = 0\}, \tag{7.12}$$
$$\Sigma_3 = \{(\lambda, T_b) : H_3(\lambda, T_b) := \lambda - \lambda_{Min} = 0\}, \tag{7.13}$$
$$\Sigma_{is} = \{(\lambda, T_b) : T_b = \Psi(\lambda)\}. \tag{7.14}$$

where Σ_{is} defines the isocline.

From the application viewpoint, the controller needs a measure of the longitudinal wheel slip λ. As it is well known, to have a measure of the wheel slip, the knowledge of the vehicle speed v is necessary. As a matter of fact, the vehicle speed v can be directly measured (by means of laser beams) only for testing and for prototyping purposes. In

commercial cars it must be estimated by indirect measurements *e.g.*, by using longitudinal accelerometers or some filtering and identification tools - see *e.g.*, [40], [35], [65], [71] and the references cited therein. Hence, the measure of the wheel slip is always affected by some estimation error. This will not compromise the proposed control methodology. Even if only a very rough wheel slip estimate is available to the controller, *e.g.*, an estimate derived only from wheel speed measurements, we will show which are the maximum allowable measurements error which guarantee the limit cycle stability and how to design the controller based on the confidence on the quality of the wheel slip measure.

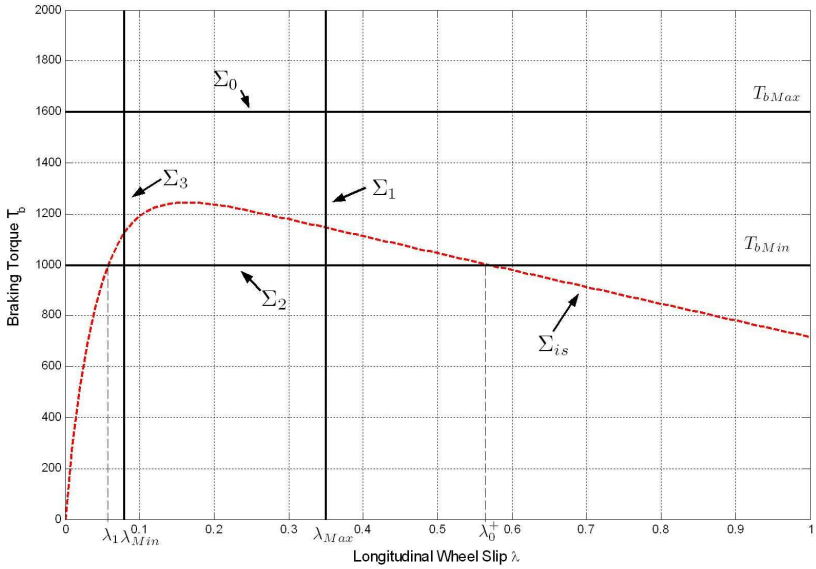

Figure 7.6: Switching Logic shown in the phase plane (λ, T_b).

By analyzing Fig. 7.7, where Finite State Machine (FMS) of the hybrid controller is depicted, one can see that we use the braking torque T_b and the wheel slip λ as switching variables and that the switching manifolds change according to the current discrete controller state $q = \{0, 1, 2, 3\}$. Moreover note that, according to the specific application, we can assume that (in normal operating conditions) the controller - upper activation - enters the state $q = 0$ associated with the Increase control action. This is due to the fact that, when the braking maneuver begins, the controller is usually activated when the wheel slip λ reaches a predefined threshold value λ_{init}, such that $\lambda_{init} < \lambda_{min}$. From now on we assume $\lambda_{init} = 0$. It is worth noticing that when the closed-loop system evolves in the discrete states $q = 1$ and $q = 3$ the control action is $u = 0$. Hence, the system dynamics given in (7.9) reduces to a first order system. Accordingly, the closed-loop trajectories in these discrete states evolve on *sliding surfaces*. This will be employed in the Poincaré map construction for the proof of the limit cycle asymptotic stability.

The main features of the limit cycle presented in Figs. 7.8 and 7.9, with threshold values $T_{bMax} = 1600\,Nm$, $T_{bMin} = 1000\,Nm$, $\lambda_{Max} = 0.35$ and $\lambda_{Min} = 0.08$. In particular, Fig. 7.8 shows the phase portrait in the three dimensional hybrid state space, where also the discrete control action is regarded as a system state variable increasing the dimension, while Fig. 7.9 shows the time evolutions of state variables λ (wheel slip)

and T_b (braking torque).

Simulation results assess that the proposed controller can indeed induce a periodic behavior in the wheel slip and in the braking torque. Nonetheless, we still have to determine conditions for the existence of the limit cycle and which are the other possible invariant sets.

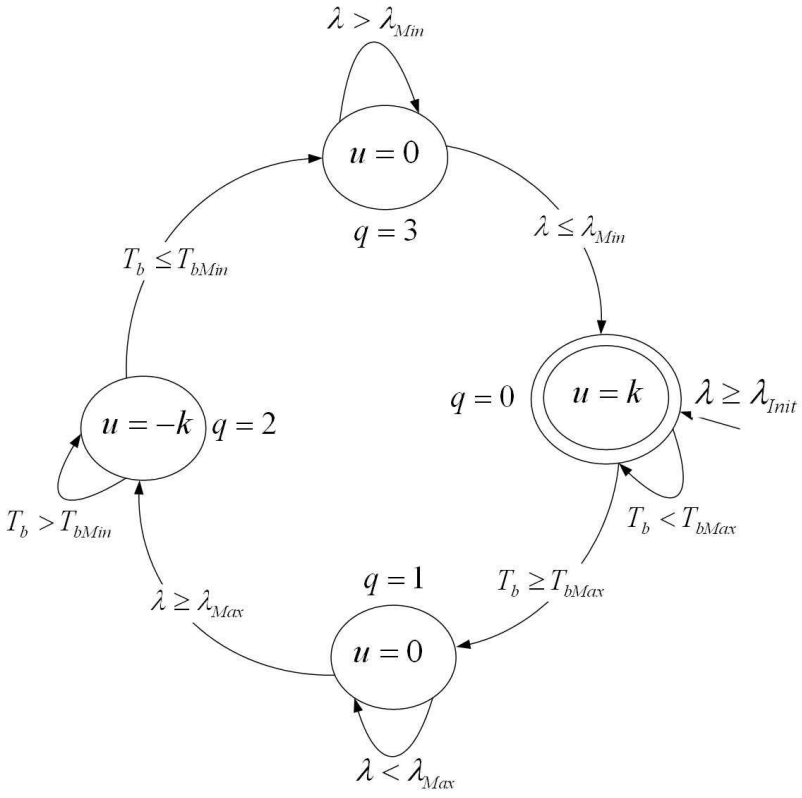

Figure 7.7: Finite State Machine of the Switching Control Logic.

7.1.4 The ABS hybrid controller as a PWSDS

Note that the ABS Hybrid Controller described in Sec. 7.1 can be recast as a Piecewise Smooth Dynamical System of the form

$$\mathcal{D}(x_0, q_0) \begin{cases} x(t) = \varphi_q(x_0, t), & \text{if } x \in \Omega_q, \quad (7.15a) \\ q \mapsto \rho(q), & \text{if } \sigma(x, q) \le 0. \quad (7.15b) \end{cases}$$

where $\rho(q)$ model the state transition in Fig. 7.7, $\sigma(x, q)$ models the condition for transition to the next state as a zero level set of a scalar function $H_q(x)$ with initial value $x(0) = x_0$ and $q(0) = q_0$

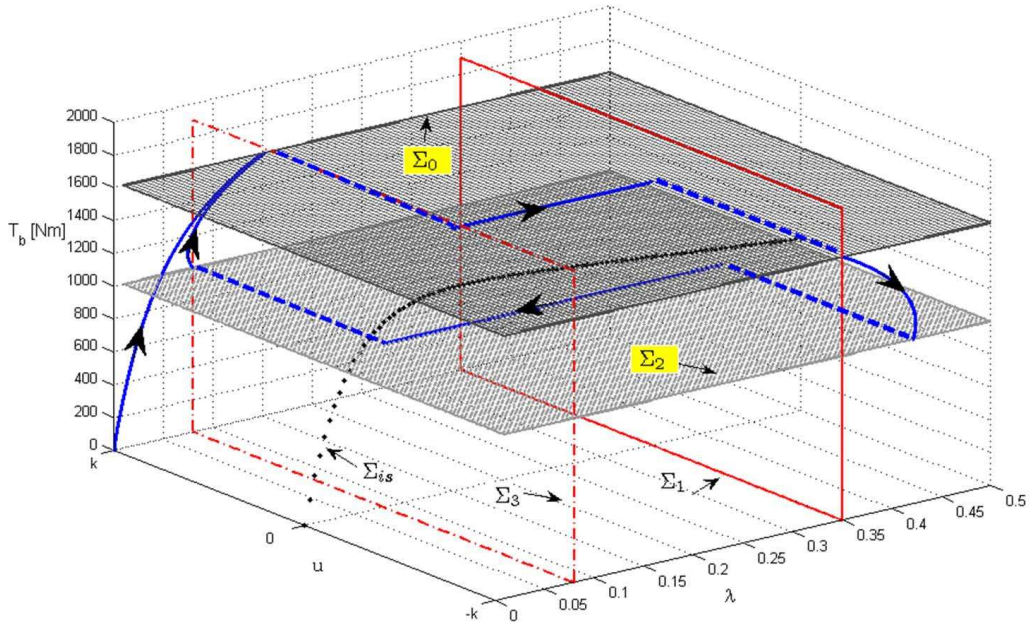

Figure 7.8: Schematic view of the switching manifolds associated to each discrete state of the hybrid controller.

7.2 Existence of limit cycles

We now investigate the existence of the limit cycle induced by the ABS hybrid controller in (7.15). Let us note $\mathcal{O}^*$ the limit cycle generated by (7.15). We can then partition the limit set $\mathcal{O}^*$ in four different segments as $part\{\mathcal{O}^*\} = \{\mathcal{O}_0, \mathcal{O}_1, \mathcal{O}_2, \mathcal{O}_3\}$, that corresponds with the long term (asymptotic) itinerary of the discrete variable q as (see Fig. 7.10):

1. When the braking maneuver begins (*i.e.* $x(0) = 0$, $u = k$), the finite state machine is in the state $q = 0$ and consequently the state of the system evolves with the dynamics given by φ_0, *i.e.* $u = k$ as:

$$x(t) = \varphi_0(0, t).$$

   The first switching will occur when the system reaches Σ_0 at the point labelled as $\bar{x}$, at time t_0 as

$$\begin{cases} \bar{x} = \varphi_0(0, t_0), \\ q^+ = \rho(0), \quad H_0(\bar{x}) = 0. \end{cases}$$

   Notice that $\bar{x}$ and t_0 are generic tags to characterize an orbit evolving on Ω_0 such that t_0 is the time required to reach $\bar{x} \in \Sigma_0$ for an arbitrary initial initial condition.

2. Analogously, at state $q = 1$ (*i.e.* $u = 0$), the state evolution is given by φ_1 with initial condition $\bar{x}$, until reaching Σ_1 at the point x_{Max} as

$$\begin{cases} x_{Max} = \varphi_1(\bar{x}, t_1), \\ q^+ = \rho(1), \quad H_1(x_{Max}) = 0. \end{cases}$$

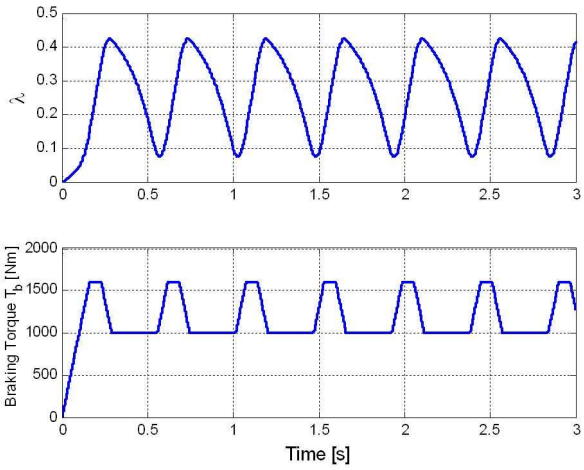

Figure 7.9: Simulated closed loop trajectory of system (7.9) with the given control logic in the hybrid state space (a) and of the wheel slip λ (top) and of the braking torque T_b (bottom) in the time domain (b).

3. Now, at state $q = 2$ (*i.e.* $u = -k$), the state evolution is given by φ_2 with initial condition x_{Max}, until reaching Σ_2 at the point $\bar{\bar{x}}$ as

$$\begin{cases} \bar{\bar{x}} = \varphi_2(x_{Max}, t_2), \\ q^+ = \rho(2), \quad H_2(\bar{\bar{x}}) = 0. \end{cases}$$

4. At state $q = 3$ (*i.e.* $u = 0$), the state evolution is given by φ_3 with initial condition $\bar{\bar{x}}$, until reaching Σ_3 at the point x_{Min} as

$$\begin{cases} x_{Min} = \varphi_3(\bar{\bar{x}}, t_3), \\ q^+ = \rho(3), \quad H_3(x_{Min}) = 0. \end{cases}$$

5. Finally, at state $q = 0$ (*i.e.* $u = k$), the state evolution is given by φ_0 with initial condition x_{Min}, until reaching Σ_3 at the point x_{Min} as

$$\begin{cases} \bar{x} = \varphi_0(x_{Min}, t_0), \\ q^+ = \rho(0), \quad H_0(\bar{x}) = 0. \end{cases}$$

Since we assume the asymptotic behavior reaches the limit set $\mathcal{O}^*$, then we can define intervals $T_i = [0, t_i]$ as the evolution time corresponding to the discrete state $q = i$, for $i = 0, \ldots, 3$.

In Fig. 7.10 we show an schematics for each of the segments $\mathcal{O}_i$ that forms the periodic orbit. We can formally define them as

$$\mathcal{O}_0 = \{x : x(t) = \varphi_0(x_{Min}, t), \ \forall\, t \in T_0\}, \tag{7.16}$$
$$\mathcal{O}_1 = \{x : x(t) = \varphi_1(\bar{x}, t), \ \forall\, t \in T_1\}, \tag{7.17}$$
$$\mathcal{O}_2 = \{x : x(t) = \varphi_2(x_{Max}, t), \ \forall\, t \in T_2\}, \tag{7.18}$$
$$\mathcal{O}_3 = \{x : x(t) = \varphi_3(\bar{\bar{x}}, t), \ \forall\, t \in T_3\}, \tag{7.19}$$

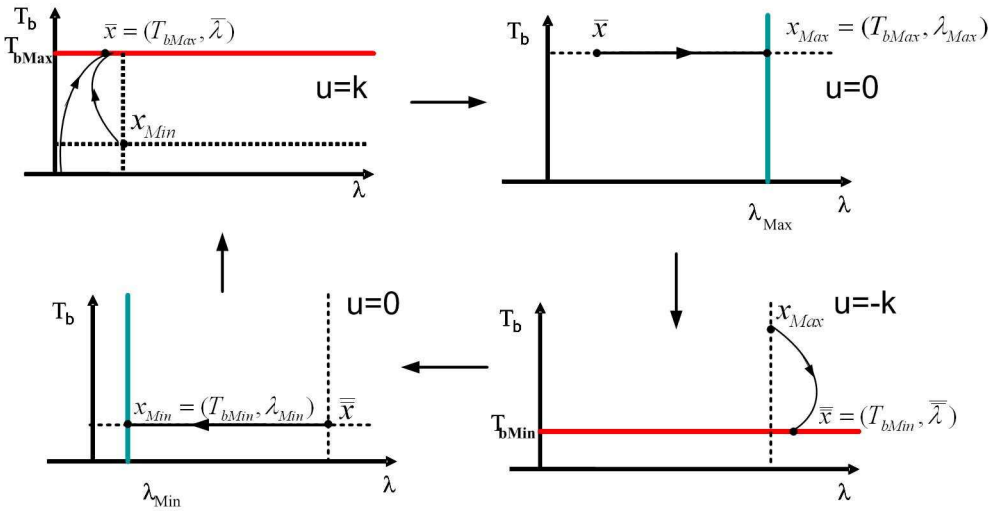

Figure 7.10: Limit cycle in terms of itinerary and initial conditions.

Note that both $\bar{x}$ and $\bar{\bar{x}}$ are functions of the system parameter k, which gives the curvature of the vector field when the system is in the states $q = 0$ and $q = 2$.

Thus, if the limit cycle $\mathcal{O}^*$ exists, the following conditions must be satisfied.

1. No intersection must exist between the switching manifold Σ_0 and the isocline manifold Σ_{is} (see Figure 7.6), i.e.,

$$\Sigma_0 \cap \Sigma_{is} = \emptyset. \tag{7.20}$$

2. The switching manifold Σ_2 must intersect the isocline manifold Σ_{is}, i.e.,

$$\Sigma_2 \cap \Sigma_{is} \neq \emptyset.$$

3. If $T_{bMin} \geq \Psi(\lambda = 1)$, i.e., two points of intersections exist between Σ_2 and Σ_{is}, that is

$$\Sigma_2 \cap \Sigma_{is} = \{(T_{bMin}, \lambda_1), (T_{bMin}, \lambda_0^+)\}$$

such that $\lambda_1 < \lambda_0^+$¡ then the intersection between the systems forward orbit $\Phi(t, [\lambda_{Max}, T_{bMax}; q = 2])$ and Σ_2 must occur at a point $(T_{bMin}, \bar{\bar{\lambda}})$ such that $\bar{\bar{\lambda}} < \lambda_0^+$, i.e.,

$$\mathcal{O}_2 \cap \Sigma_2 = (T_{bMin}, \bar{\bar{\lambda}}),$$

such that $\bar{\bar{\lambda}} < \lambda_0^+$.

Setting the threshold values $T_{bMax} = 1600Nm$, $T_{bMin} = 1000Nm$, $\lambda_{Max} = 0.35$, $\lambda_{Min} = 0.08$, and other system parameters, we can compute numerical solutions of (7.15) for the unknowns $\bar{\lambda} = 0.147$, $\bar{\bar{\lambda}} = 0.419$, $t_0 = 0.06$, $t_1 = 0.068$, $t_2 = 0.06$ and $t_3 = 0.329$, as depicted in Fig. 7.11. It is straightforward to compute the period T of $\mathcal{O}$ as

$$T = \sum_{i=0}^{3} t_i = 0.517 \ S.$$

We can also compute the amplitude referred to each of the state variables as A_{T_b} (T_b–Amplitude) and A_λ (λ–Amplitude). The T_b–Amplitude is fixed a-priori from the choice of the thresholds as

$$A_{T_b} = T_{bMax} - T_{bMin} = 600 \text{ Nm},$$

while λ–Amplitude needs to be computed numerically, using the fact that at λ_{min} as well as at λ_{max} it is hold the condition $\dot{\lambda} = 0$ occurs. In fact, the cycle λ-amplitude is

$$A_\lambda = \lambda_{max} - \lambda_{min} = 0.346.$$

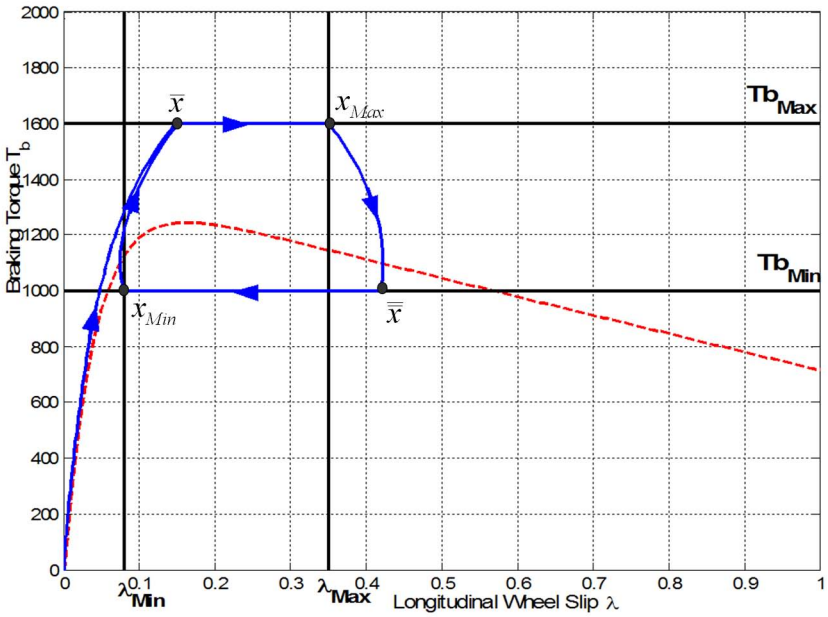

Figure 7.11: Phase portrait of the limit cycle obtained as solution of (7.15).

7.3 Asymptotic stability of limit cycles

To prove asymptotic stability of the limit cycle exhibited by system (7.15) and depicted in Fig. 7.11, we construct an appropriate *Poincaré* map. we choose the plane $\Pi := \{(\lambda, T_b) : \lambda = 0.2\}$, as a suitable *Poincaré* section transversal to the limit cycle flow (see Fig. 7.12). As the system evolves, its trajectory intersects Π transversally. Let x_n be the n-th intersection of the system flow with the section Π. Also, let $x^* = [\lambda^*, T_b^*]^{T/2} \in \Pi$ be the point at which the limit cycle crosses the *Poincaré* section. Then, it is possible to construct a local mapping $P : \Pi \to \Pi$ in a neighborhood of x^* from one intersection x_n to the next x_{n+1}. Specifically, we have

$$x_{n+1} = P(x_n), \ x_n \in \mathrm{B}_\varepsilon(x^*),$$

where $\mathrm{B}_\varepsilon(x^*)$ is a ball of center x^* and radius ε.

In Fig. 7.12, we present the composition of P for two particular values $x_0^-, x_0^+ \in \mathrm{B}(x^*)$. Trajectories starting at any of these two initial conditions evolve until reaching the switching manifold $\lambda = \lambda_{Max} \in \Sigma_1$. Then, when the second switching with manifold Σ_2 occurs, both trajectories evolve again reaching the limit cycle $\mathcal{O}$ which annihilates the initial perturbation. We can then write

$$P(x_n) = x^* \forall x_n \in \mathrm{B}(x^*).$$

we deduce that the only multiplier of P is null (*i.e.* $\mu = 0$). This guarantees that the limit cycle is not only *asymptotically stable*, but it is also characterized by *dead beat* convergence (see [76]).

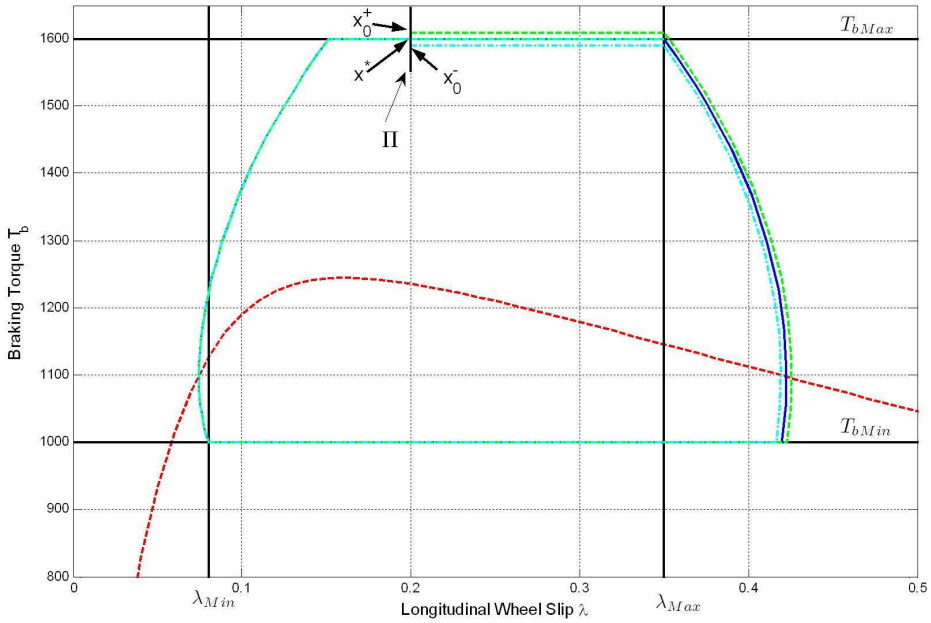

Figure 7.12: Poincaré map for the initial conditions x_0^- and x_0^+ in a neighborhood of the fixed point x^*.

7.4 Structural stability of limit cycles

To characterize the structural stability of the limit cycle, we first define the concept of basin of attraction for the hybrid controller of the form (7.15), as it provides quantitative information on the controller robustness against measurements uncertainties. Further, we focus on changes in both the road condition and in the actuator rate limit k.

7.4.1 Basins of attraction

We are interested in characterizing a limit cycle under perturbations in the initial conditions. For the case of an hybrid controller of the form (7.15), we define the set

$$\mathcal{B}_{\mathcal{O}}(q_0) = \{x_0 : x_0 \in \mathbb{R}^n, \exists t \text{ such that } x(t) = \mathcal{D}(x_0, q_0) \in \mathcal{O}\}$$

as the *basin of attraction* of *PWSC*[1] *Limit Cycle* $\mathcal{O}$ associated to the initial state $q_0 \in \mathbb{Z}$. In other words $\mathcal{B}_{\mathcal{O}}(q_0)$ is the set of all initial conditions $x_0 \in \mathbb{R}^n$ which yield trajectories converging to $\mathcal{O}$ using the hybrid dynamical system $\mathcal{D}(x_0, q_0)$ where $x(0) = x_0$ and $q(0) = q_0$.

The phase portrait of the hybrid system consist of four different solutions (or invariant sets):

- The limit cycle (see Sec. 7.2)
- Two stable equilibria, namely wheel locking equilibrium $\lambda_1^{ss} = 1$ and the equilibria on the isocline λ_2^{ss} (see Fig. 7.5).
- An unstable equilibrium λ_3^{ss} (see Fig. 7.5).

In Fig. 7.13(a) we present the set $\mathcal{B}_{\mathcal{O}}(0)$ which is the white region , the light gray region indicates the set of initial conditions which lead to wheel locking (i.e., to $\lambda_1^{ss} = 1$), while the rest of the plane is the basin of attraction $\mathcal{B}_{\mathcal{O}}(0)$. The basin of attraction $\mathcal{B}_{\mathcal{O}}(1)$ is presented in Fig. 7.13(b), where the dark gray region indicates the set of initial conditions which converge to an equilibrium on the isocline λ_2^{ss}. Finally, Figs. 7.14(a) and 7.14(b) show $\mathcal{B}_{\mathcal{O}}(2)$ and $\mathcal{B}_{\mathcal{O}}(3)$ respectively.

From the application view point, the only undesirable behavior both in terms of safety and braking performance, is wheel locking. It is worth noticing that if we consider the intersection (over the four discrete states Figs. 7.13(a), 7.13(b), 7.14(a) and 7.14(b)) of the basins of attraction, regarding as acceptable both the initial conditions converging to the limit cycle and those converging to a point on the isocline (*i.e.* white area plus dark gray area are desired), we can see that the safe region of the state space is indeed very large. This highlights the good robustness properties of the proposed control algorithm.

Robustness to measure uncertainties

Basins of attraction are extremely useful as they can also be interpreted from the synthesis point of view. Since in real applications the wheel slip λ and the braking torque T_b, cannot be directly measured; it is crucial to take into account measurements errors in the control design of active braking control systems. With our approach, the measurements of λ and T_b are needed in order to detect the switching manifolds which enable the state transitions. The analysis carried out to compute the basins of attraction does also provide quantitative information about the maximum allowable perturbation in the state measure which guarantees closed-loop stability. Consider again Fig. 7.13(a), where the dashed arrow represents the distance between the steady-state periodic orbit in the discrete state $q = 0$ and the boundary of the locking region (so forth for Figs. 7.13(b), 7.14(a) and 7.14(b)).

By computing these quantities for all discrete states, we can find the maximum allowable perturbation of the state measurements Γ, that clearly depends (for fixed vehicle and actuator parameters) on the threshold values that one has chosen for T_{bMax}, T_{bMin}, λ_{Max} and λ_{Min}. These, nonetheless, are the tuning parameters of the proposed controller and hence can be adjusted according to the known uncertainty in the state measurements. For example, if the available wheel slip measures are known to have an error $e = \pm 10\%$, then one may very easily compute Γ for different choices of the threshold values, so that the limit cycle stability can be guaranteed for measure uncertainties within the pre-defined error bounds.

[1] Piecewise Smooth Continuous.

7.4.2 Bifurcation diagram

Bifurcation analysis allow us to study the structural stability of the limit cycle as function of the threshold values. To this end, Fig. 7.15 shows a bifurcation diagram of the limit cycle as function of the threshold value T_bMax. For values of T_{bMax} which satisfy (7.20) the limit cycle exists (with different amplitude and period according to the specific numerical value of T_{bMax}). Then, when the critical value $T^{cr}_{bMax} = max_\lambda \Psi(\lambda)$ is reached, the limit cycle disappears and the equilibrium is given by the intersection between Σ_0 and Σ_{is} (*i.e.* λ_2^{ss}). This type of bifurcation is typical of nonsmooth dynamical systems, is referred as a nonsmooth semi-global Hopf bifurcation; where the term semi-global refers to the fact that the first limit cycle which appears after the critical value of the parameter is reached, has finite amplitude (see [43]).

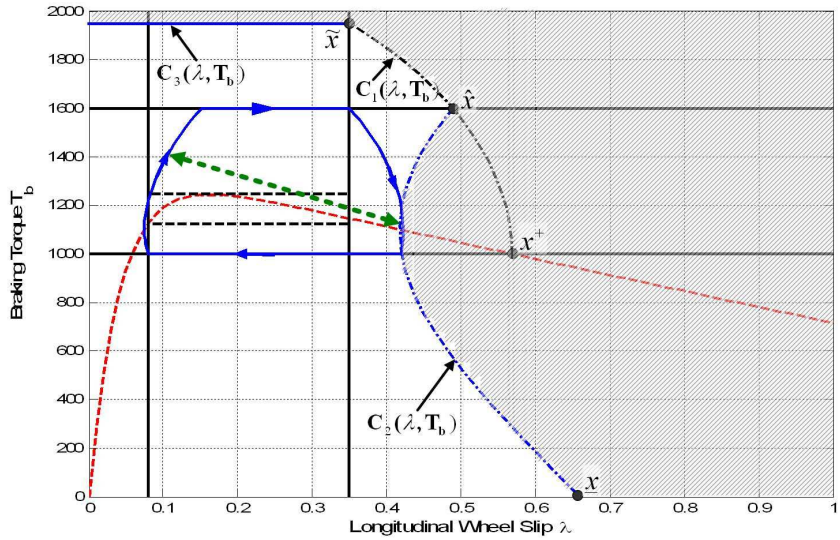

(a)

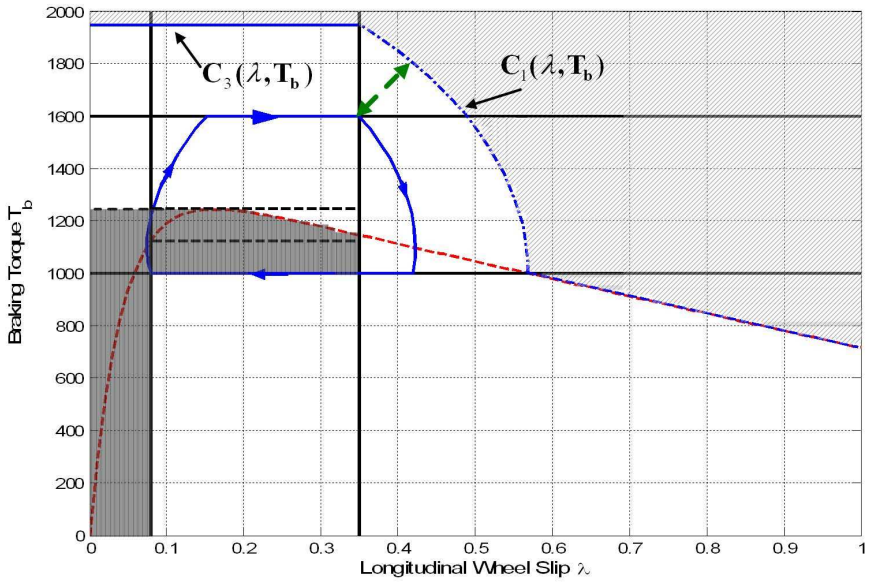

(b)

Figure 7.13: Basin of attraction of the limit cycle associated to the discrete controller state $q = 0$ (a) and $q = 1$ (b) in the phase plane (λ, T_b).

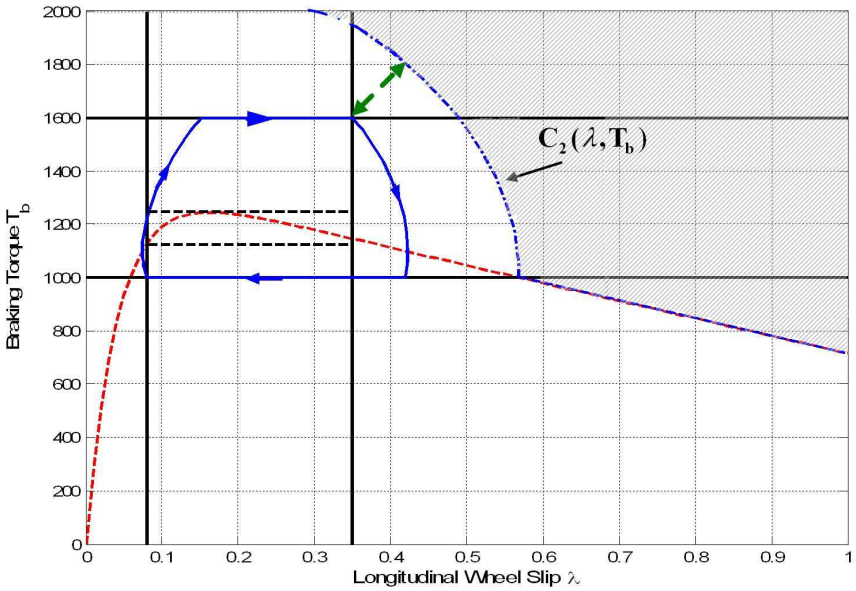

(a)

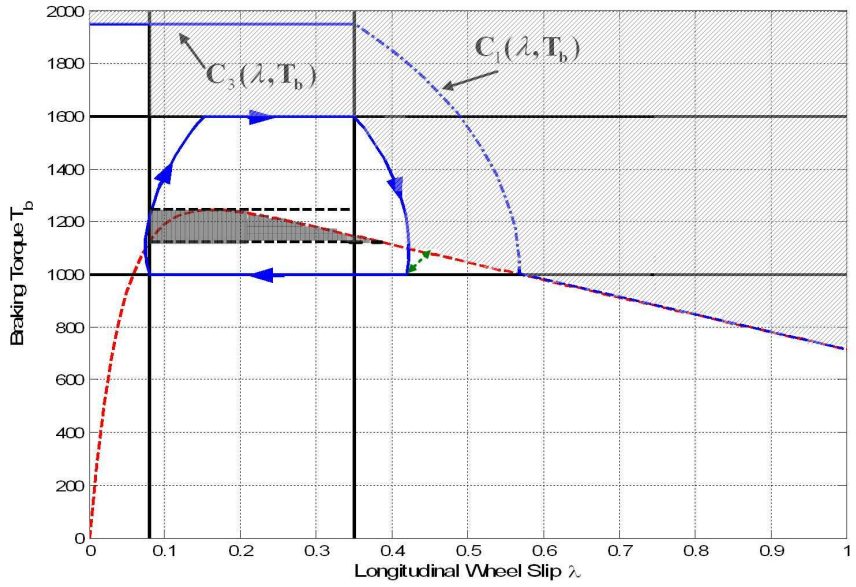

(b)

Figure 7.14: Basin of attraction of the limit cycle associated to the discrete controller state $q = 2$ (a) and $q = 3$ (b) in the phase plane (λ, T_b).

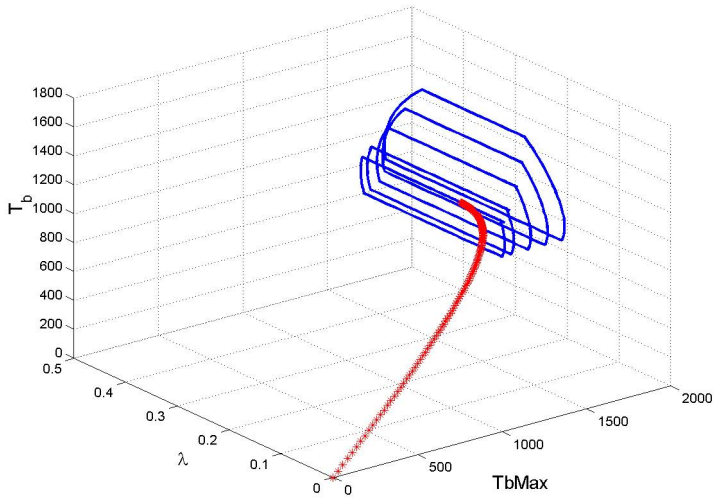

Figure 7.15: Plot of the non-smooth semi-global Hopf bifurcation in the system equilibria which is induced by the variation of the threshold value T_{bMax}.

Chapter 8

Conclusions

Contents

8.1 Main Contributions

The contributions of this thesis have been concerned with several aspects and open problems that are currently matter of research in the community studying nonsmooth dynamical systems. Namely, they have been focused on the development of numerical algorithms for the simulation of impacting systems and their unique phenomena such as sticking and chattering (i.e. Zeno behavior). A systematic study of structural stability of piecewise smooth periodic orbits has also been carried out in the context of the qualitative theory of dynamical systems. A summarizing list of the main contributions presented in this thesis is given bellow:

1. *Development of numerical routines for*:
   - Simulation - Chattering, sliding (sticking).
   - Discontinuity Induced Bifurcations detection and continuation.
   - Numerical Polynomial Approximation of Vector fields.
2. *Analytical investigation of*:
   - Dynamics of mechanical impacting systems.
   - Cam–follower devices as a subclass of Impacting Systems.
   - Bifurcation detection and continuation.
   - Corner-Impact Bifurcation in impacting systems with singularities in the boundaries.
3. Existence, Stability and Robustness Analysis of Limit Cycles in Hybrid ABS Switched Controller.

More precisely, we can say that in this thesis we have introduced a set of novel numerical and analytical tools for the study of impacting systems in the context of the qualitative theory of dynamical systems.

Specifically, in Chapters 1, 2 and 3, after presenting some background we outlined in a systematic way a new bifurcation phenomenon in impacting systems we have termed as corner-impact bifurcation. We used numerical and analytical tools already introduced in the context of qualitative analysis for smooth and nonsmooth dynamical systems.

In chapter 4, we discussed the complex dynamics exhibited by a cam-follower system under variation of the cam rotational speed. It was shown that as the bifurcation parameter is varied; the follower undergoes several bifurcations involving transitions from periodic solutions to chaos. Chattering behavior seemed to be the key to understand the phenomena reported together with the nonsmooth nature of the cam profile which forces the follower dynamics. In particular, sudden transitions were observed whenever the follower evolution hit one of the boundaries where the cam velocity signal becomes non-differentiable.

In Chapter 5, we studied a novel type of discontinuity-induced bifurcation in a class of mechanical devices widely used in applications and particularly cam-follower systems. Using a representative second order model of the follower, we showed that its dynamics can undergo several bifurcations including sudden transitions to chaos as the cam rotational speed is varied. We analyzed in detail the corner-impact bifurcation of a one-periodic solution characterized by one impact per period. In particular, we observed that the systems behavior undergoes dramatic changes when the impact occurs at a point where the cam profile is discontinuous. Using the concept of discontinuity mappings, we derived analytically the Poincaré map associated to the bifurcating orbit in the case where the cam profile has a discontinuous acceleration. Then, using the classification strategy for border-collision bifurcations, we proved that the corner-impact causes the fixed point associated to the bifurcating orbit to undergo a nonsmooth saddle node bifurcation. Namely, the fixed point ceases to exist, with the trajectories being attracted toward a chaotic invariant set. The analysis presented in Chapter 5, applies with minor changes to the case of impact oscillators forced by signals with discontinuous second derivative. This leads to maps which are locally piecewise-linear continuous close to a corner-impact bifurcation point. We conjectured that the properties of the local mapping depend on the degree of discontinuity of the forcing signal. This is the subject of ongoing work.

Discontinuity-induced bifurcations in flows are usually associated to maps which are not piecewise-linear. Grazing bifurcations of limit cycles are known to be associated to maps with square-root singularities in impacting systems and Filippov systems or maps with higher order nonlinear terms in the case of piecewise-smooth continuous (PWSC) flows. The only cases in the literature where the map was indeed found to be piecewise-linear continuous were corner-collisions in PWSC systems and grazing sliding bifurcations in Filippov systems. So far, no evidence was given of a bifurcation event in impacting systems associated to locally piecewise-linear continuous maps. The corner-impact bifurcation scenario presented in this thesis fills this gap in the literature. We showed that cam-follower systems are a particularly useful set-up to show generically the behavior of impacting systems with discontinuous forcing.

The results presented in Chapters 5 and 6 can pave the way to future work toward a better understanding of the complex dynamics of cam-follower systems. This can lead to less conservative solutions to detachment avoidance, hopefully without resorting to highly stiff closing springs, and maybe active control strategies. In Chapter 6, we proposed a new technique for the analysis of Corner-Impact Bifurcations introducing

the concept of corner-impact map.

Finally, in Chapter 7, the existence, asymptotic stability and robustness of a limit cycle induced by a hybrid controller for Anti-lock Braking Systems with on/off actuator dynamics was investigated. We gave necessary conditions for the limit cycle existence and proved it by showing that a related boundary value problem admits a solution. Further, we assessed its asymptotic stability properties via Poincaré map analysis and provided a structural stability analysis with respect to the actuator rate limit.

Bibliography

[1] V. Acary. Simulation of a bouncing ball with the moreau's time–stepping scheme. SICONOS Project Internal Report, WP2–Template, Feb. 2004.

[2] M.A. Aizerman and F.R Gantmakher. On the stability of periodic motions. *Appl. Math. Mech.*, pages 1065–1078, 1958.

[3] K. Akiba and H. Sakai. A comprehensive simulation of high speed driven valve trains. *SAE Transactions*, 1981.

[4] R. Alzate, M. di Bernardo, U. Montanaro, and S. Santini. Experimental and numerical verification of bifurcations and chaos in a cam-follower system. *Nonlinear Dynamics, Special Issue Springer Verlag*, 2007.

[5] S. Banerjee and C. Grebogi. Border collision bifurcations in two-dimensional piecewise smooth maps. *Physical Review E*, 59(4):4053–4061, April 1999.

[6] P. Barkan. Calculation of high speed valve motion with a flexible overhead linkage. *SAE Transactions*, 61:687–700, 1953.

[7] B. Brogliato. *Nonsmooth Mechanics*. Springer, 2nd edition edition, 1999.

[8] B. Brogliato. Some perspectives on the analysis and control of complementarity systems. *IEEE Transactions on Automatic Control*, 48:918–935, 2003.

[9] Ch. Budd and F. Dux. Chattering and related behavior in impact oscillators. *Phil. Trans. Royal Society London A.*, 347, 1994.

[10] Ch. Budd, F. Dux, and A. Cliffe. The effect of frequency and clearance variations on single-degree-of-freedom impact oscillators. *Journal of Sound and Vibration*, 3(184):475–502, 1996.

[11] Ch. Budd and P. Piiroinen. Corner bifurcations in non-smoothly forced impact oscillators. *Physica D: Nonlinear Phenomena*, 220(2):August, 127-145 2006.

[12] A. Cardona, E. Lens, and N. Nigro. Optimal design of cams. *Multibody System Dynamics*, 7:285–305, 2002.

[13] T. Choi, O. Eslinger, C. Kelley, J. David, and M. Etheridge. Optimization of automotive valve train components with implicit filtering. *Optimization and Engineering*, 1(1):9 – 27, 2000.

[14] H. Dankowicz and A. Nordmark. On the origin and bifurcations of stick-slip oscillations. *Physics D*, 136(3-4):280–302, 2000.

[15] M. di Bernardo. Normal forms of border collisions in high-dimensional maps. In *Proceedings IEEE ISCAS, Bangkok, Thailand.*, pages 76–79, 2003.

[16] M. di Bernardo, C. Budd, and A. Champneys. Corner collision implies border-collision bifurcation. *Physica D*, ??(154):171–194, 2001.

[17] M. di Bernardo, C. Budd, and A. Champneys. Normal form maps for grazing bifurcations in n-dimensional piecewise smooth systems. *Physica D*, 154:171–194, 2001.

[18] M. di Bernardo, C. Budd, A.R. Champneys, P. Kowalczyk, A.B. Nordmark, G. Olivar, and P.T. Piiroinen. Bifurcations in nonsmooth systems. *In submission*, 2006.

[19] M. di Bernardo, Ch. Budd, A. Champneys, and P. Kowalczyk. *Piecewise-smooth Dynamical Systems: Theory and Applications.* Springer., 2007.

[20] M. di Bernardo, C.J. Budd, and A.R. Champneys. Corner collision implies border-collision bifurcation. *Physica D*, pages 171–194, 2001, 154.

[21] M. di Bernardo, M. I. Feigin, S.J. Hogan, and M. E. Homer. Local analysis of c-bifurcaiotions in n-dimensional piecewise-smooth dynamical systems. *Chaos, Solitons & Fractals*, 10(11):1881–1908, 1999.

[22] T. L. Dresner and P. Barkan. New methods for the dynamic analysis of flexible single-input and multi-input cam-follower systems. *Journal of Mechanical Design*, 117:151, 1995.

[23] B. Fabien. The design of dwell-rise-dwell cams with reduced sensitivity to parameter variation. *Journal of The Franklin Institute*, 332:195–209, 1995.

[24] M. I. Feigin. The increasingly complex structure of the bifurcation tree of a piecewise smooth system. *J. Appl. Maths Mechs.*, 59(6):853–863, 1995.

[25] A. F. Filippov. Differential equations with discontinuous right-side. *Kluwer Academic Publishers, Dortrecht,*, pages 199–231, 1988.

[26] H. Fredriksson and A. Nordmark. Bifurcation caused by grazing incidence in many degrees of freedom impact oscillators. *Proc. R. Soc. Lond.*, 453:1261–1276, 1997.

[27] G.L. Gissinger, C. Menare, and A. Constans. A mechatronic conception of a new intelligent braking system. *Control Engineering Practice*, 11:163–170, 2003.

[28] Ch. Glocker. On frictionless impact models in rigid-body systems. *Phil. Trans. R. Soc. Lond.*, 359:2385–2404, 2001.

[29] Ch. Glocker. Impacts with global dissipation index at reentrant corners. In *Proc. 3rd Contact Mechanics International Symposium*, pages 45–52. Kluwer Academic Pulishers., Jun 2002.

[30] J. Gukenheimer and P. Holmes. *Dynamical Systems, and Bifurcations of Vector Fields*. Springer-Verlag, New York, 1983.

[31] J. Heywood. *Internal Combustion Engine Fundamentals*. McGraw-Hill, 1998.

[32] N. Hinrichs, M. Oestreich, and K. Popp. Dynamics of oscillators with impact and friction. *Chaos, Solutions & Fractals*, 8(4):535–558, 1997.

[33] J. Hogan, L. Higham, and T. C. L. Griffin. Dynamics of a piecewise linear map with a gap. *Article submitted to Phil. Trans. R. Soc. A. London.*, 463:49–65, 2006.

[34] P. Holmes. Ninety plus thirty years of nonlinear dynamics: Less is more and more is different. *International Journal of Bifurcation and Chaos*, 15(9):2703–2716, 2005.

[35] F. Jiang and Z. Gao. An adaptive nonlinear filter approach to the vehicle velocity estimation for ABS. In *Proceedings of the 2000 IEEE International Conference on Control Application, Anchorage*, September 25-27 2000.

[36] T.A. Johansen, J. Petersen, J. Kalkkuhl, and J. Ldemann. Gain-scheduled wheel slip control in automotive brake systems. *IEEE Transactions on Control Systems Technology*, 11(6):799–811, November 2003.

[37] K. Johansoon. Lecture notes on hybrid systems.

[38] K. Johansson, J. Lygeros, J. Zhang, and S. Sastry. Hybrid automata: A formal paradigm for heterogeneous modeling. In *Proc. 3rd Contact Mechanics International Symposium*, pages 123–128. Symposium on Computer-Aided Control System Design, Sept 2000.

[39] U. Kiencke and L. Nielsen. *Automotive Control Systems*. Springer-Verlag, Berlin, 2000.

[40] K. Kobayashi, K.C. Cheok, and K. Watanabe. Estimation of absolute vehicle speed using fuzzy logic rule-based Kalman filter. In *Proceedings of the 1995 American Control Conference, Seattle, USA*, June 21-23 1996.

[41] M. Koster. *Vibrations of Cam Mechanisms*. Phillips Technical Library Series, Macmillan Press Ltd.: London, 1974.

[42] M. Kushwaha and H. Rahnejat. Valve-train dynamics: a simplified tribo-elasto-multi-body analysis. *IProceedings of the Institution of Mechanical Engineers, Part K: Journal of Multi-body Dynamics*, 214:1464–4193, 2001.

[43] Y. A. Kuznetsov. *Elements of Applied Bifurcation Theory*. Springer–Verlag, New York, second edition, 1998. Applied Mathematical Sciences, Volume 112.

[44] R. Leine, B. Brogliato, and H. Nijmeijer. Periodic motion and bifurcations induced by the painlav paradox. *European Journal of Mechanics A/Solids*, 21:869–896, 2002.

[45] R. Leine and H. Nijmeijer. *Dynamics and Bifurcations in Non-Smooth Mechanical Systems*. Springer-Verlag, 2004.

[46] R. I. Leine, D. H. van Campen, and B. L. van de Vrande. Bifurcations in nonlinear discontinuous systems. *Nonlinear Dynamics*, 23(2):105–164, October 2000.

[47] D. Liberzon. *Switching in Systems and Control*. Birkhauser, 2003.

[48] Burckhardt M. *Fahrwerktechnik: Radschlupf-Regelsysteme*. Vogel Verlag, Wrzburg, 1993.

[49] R. M. May. Simple mathematical models with very complicated dynamics. *Nature*, 261(4):459–467, 6 1976.

[50] P. C. Mueller. Calculation of lyapunov exponents for dynamical systems with discontinuities. *Chaos, Solitons & Fractals*, 5:1671–1681, 1995.

[51] A. Nordmark. Non-periodic motion caused by grazing incidence in an impact oscillator. *Journal of Sound and Vibration*, 145(2):279–297, March 1991.

[52] A. Nordmark. Universal limit mapping in grazing bifurcations. *Physical Review E*, 55:266–270, 1997.

[53] A. Nordmark. Existence of periodic orbits in grazing bifurcations of impacting mechanical oscillators. *Nonlinearity*, 14:1517–1542, 2001.

[54] A. Nordmark. Bifurcations of impacting systems. PhD School on Nonsmooth Dynamical Systems, Naples, Italy., Sept 2006.

[55] A. Nordmark and P. Piiroinen. Simulation and stability analysis of impact systems with complete chattering. *In progress*, 2006.

[56] A.B. Nordmark and P.T. Piiroinen. Simulation and stability analysis of impacting systems with complete chattering. *Submitted to Nonlinear Dynamics*, 2007.

[57] R. Norton. *Cam Design and Manufacturing Handbook*. Industrial Press Inc., 1st edition edition, 2002.

[58] R. Norton, D. Eovaldi, J. R. Westbrook, and R. L. Stene. Effect of the valve-cam ramps on valve train dynamics. *SAE paper 1999-01-0801*, 1999.

[59] F. Peterka. Impact oscillator. In Bram de Kraker Marian Wiercigroch, editor, *Applied Nonlinear Dynamics and Chaos of Mechanical Systems with Discontinuities*, volume 28 of *A*, chapter 5, pages 103,126. World Scientific Publishing Co. Pte. Ltd., 2000.

[60] P. Piiroinen, L. Virgin, and A. Champneys. Chaos and period=adding; experimental and numerical verification of the grazing bifurcation. *Journal of Nonlinear Science*, 14:383–404, 2004.

[61] P.T. Piiroinen and Yu.A. Kuznetsov. An event-driven method to simulate filippov systems with accurate computing of sliding motions. *ACM Transactions on Mathematical Software*, 3(34), 2008.

[62] SICONOS platform overview. http://siconos.gforge.inria.fr/siconosprojectoverview.

[63] SICONOS project. http://siconos.inrialpes.fr/.

[64] E. Raghavacharyulu and J. Rao. Jump phenomena in cam-follower systems a continuous-mass-model approach. *American Society of Mechanical Engineers, Proceedings of the Winter Annual Meeting*, pages 1–8, 1976.

[65] L. Ray. Nonlinear state and tire force estimation for advanced vehicle control. *IEEE Transactions on Control Systems Technology*, 3(1):117–124, 1995.

[66] S. Seidlitz. Valve train dynamics - a computer study. *SAE Transactions, 890620*, 1989.

[67] S. W. Shaw and P. Holmes. Periodically forced linear oscillator with impacts: Chaos and long-period motions. *Physical Review Letters*, 51(8):623–626, August 1983.

[68] Society of Automotive Engineers, Warrendale, PA. *Antilock Brake Review*, 1992. SAE Standard: J2246.

[69] S. Strogatz. *Nonlinear Dynamics and Chaos: With Applications to Physics, Biology, Chemestry and Engineering*. Perseus Books Publishing, 1st edition edition, 2000.

[70] R. Szalai, Stépán G., and S. J. Hogan. Global dynamics of low immersion high-speed milling. *Chaos*, 14(4):1069–1077, 11 2004.

[71] M. Tanelli, S.M. Savaresi, and C. Cantoni. Longitudinal Vehicle Speed Estimation for Traction and Braking Control Systems. In *Proceedings of the 2006 Conference on Control and Applications - CCA 2006*, 2006. To Appear.

[72] M. Teodorescu, V. Votsios, H. Rahnejat, and D. Taraza. Jounce and impact in cam-tappet conjunction induced by the elastodynamics of valve train system. *Meccanica*, 41(2):157 – 171, 2006.

[73] M. Todd and L. Virgin. An experimental impact oscillator. *Chaos, Solitons and Fractals*, 8:699–714, 1997.

[74] T. Tumer and Y. Samim Unlusoy. Nondimensional analysis of jump phenomenon in force-closed cam mechanisms. *Mechanism and Machine Theory*, 6:421–432, 1991.

[75] V. I. Utkin. *Sliding Modes in Control and Optimizations*. Springer-Verlag, Berlin, 1992.

[76] S. Wiggis. *Introduction to Applied Nonlinear Dynamical Systems and Chaos.* Springer-Verlag, New York, 1990.

[77] H. S. Yan, M. Tsai, and M. H. Hsu. An experimental sudy ofthe effect of the cam speed on cam=follower systems. *Journal of Mech. Mach. Teory*, 31:397=412, 1996.

[78] J. Zhang, K. Johansson, J. Lygeros, and S. Sastry. Zeno hybrid system. *International Journal of Robust and Nonlinear Control*, 11(5):435–451, 2001.